Growth of GaN nanowire ensembles in molecular beam epitaxy: Overcoming the limitations of their spontaneous formation

D I S S E R T A T I O N

zur Erlangung des akademischen Grades

Dr. rer. nat.
im Fach Physik
Spezialisierung: Experimentalphysik

eingereicht an der
Mathematisch-Naturwissenschaftlichen Fakultät I
Humboldt-Universität zu Berlin

von
M. Sc. Johannes Kristian Zettler

Präsidentin der Humboldt-Universität zu Berlin:
Prof. Dr.-Ing. habil. Dr. Sabine Kunst

Dekan der Mathematisch-Naturwissenschaftlichen Fakultät I:
Prof. Dr. Elmar Kulke

Gutachter:
(i) Prof. Dr. Henning Riechert
(ii) Prof. Dr. W. Ted Masselink
(iii) Prof. Dr. Jean Christophe Harmand

eingereicht am:
Tag der mündlichen Prüfung: 29.03.2017

Abstract

In molecular beam epitaxy, dense arrays of GaN nanowires form spontaneously on crystalline as well as amorphous substrates. Due to the nature of spontaneous formation, the control over important parameters is limited.

This thesis addresses the major limitations of spontaneous nanowire formation, namely the nanowire diameter, number density, and coalescence degree but also the maximum achievable growth temperature, and presents approaches to overcome the same. Thereby, we have fabricated a new class of nanowires with unprecedented structural and optical properties.

We find that a two-step growth approach, where the substrate temperature is increased during the nucleation stage, is an efficient method to gain control over the area coverage, average diameter, and coalescence degree of GaN nanowire ensembles. Furthermore, we also demonstrate that the growth conditions employed during the incubation time that precedes nanowire nucleation do not influence the properties of the final nanowire ensemble.

Furthermore, we present three growth approaches to minimize the long incubation time that precedes nanowire nucleation at elevated temperatures and to thus facilitate significantly higher growth temperatures (up to 905°C). We achieve this advancement by (i) using III/V flux ratios larger than one to compensate for Ga desorption, (ii) utilizing the two-step growth procedure introduced above, and (iii) using an AlN buffer layer to favor GaN nucleation. The GaN nanowire ensembles grown at so far unexplored substrate temperatures exhibit excitonic transitions with sub-meV linewidths comparable to those of state-of-the-art free-standing GaN layers grown by hydride vapor phase epitaxy.

Finally, we fabricate nanowires with diameters well below 10 nm, the lower boundary given by the nucleation mechanism of spontaneously formed nanowires. Here, regular nanowire arrays are thinned in a post-growth decomposition step in ultra-high vacuum. In situ monitoring the progress of decomposition using quadrupole mass spectrometry enables a precise control over the diameter of the thinned nanowires. These ultrathin nanowires show dielectric confinement, which is potentially much stronger than quantum confinement. We demonstrate intense excitonic emission from bare GaN nanowires with diameters down to 6 nm. The large dielectric mismatch between the nanowires and vacuum greatly enhances the Coulomb interaction, with the thinnest nanowires showing the strongest dielectric confinement and the highest radiative efficiency at room temperature. These ultrathin nanowires may constitute the basis for the fabrication of advanced low-dimensional structures with an unprecedented degree of confinement.

Keywords: gallium nitride, GaN, nanowires, nanocolumns, nanorods, molecular beam epitaxy, spontaneous formation, two-step growth, high temperature, photoluminescence, ultrathin, dielectric confinement

Zusammenfassung

Dichte Ensembles aus GaN-Nanodrähten können in der Molekularstrahlepitaxie mithilfe eines selbstinduzierten Prozesses sowohl auf kristallinen als auch amorphen Substraten gezüchtet werden. Aufgrund der Natur selbstgesteuerter Prozesse ist dabei die Kontrolle über viele wichtige Ensembleparameter jedoch eingeschränkt.

Die Arbeit adressiert genau diese Einschränkungen bei der Kristallzucht selbstinduzierter GaN-Nanodrähte. Konkret sind das Limitierungen bezüglich der Nanodraht-Durchmesser, die Nanodraht-Anzahl-/Flächendichte, der Koaleszenzgrad sowie die maximal realisierbare Wachstumstemperatur. Für jede dieser Einschränkungen werden Lösungen präsentiert, um die jeweilige Limitierung zu umgehen oder zu verschieben. Als Resultat wurde eine neue Klasse von GaN Nanodrähten mit bisher unerreichten strukturellen und optischen Eigenschaften geschaffen.

Mithilfe eines Zwei-Schritt-Ansatzes, bei dem die Wachstumstemperatur während der Nukleationsphase erhöht wurde, konnte eine verbesserte Kontrolle über die Flächendichte, den Durchmesser und den Koaleszenzgrad der GaN-Nanodraht-Ensembles erreicht werden. Desweiteren konnten wir zeigen, dass die Wachstumsbedingungen während der Inkubationsphase keinen Einfluss auf die Eigenschaften des finalen Nanodraht-Ensembles haben.

Darüber hinaus werden drei Ansätze präsentiert, um die außerordentlich lange Inkubationszeit, welche bei hohen Wachstumstemperaturen vor der Nanodraht-Nukleation auftritt, zu minimieren und damit wesentlich höhere Wachstumstemperaturen zu ermöglichen (bis zu 905 °C). Die Verbesserungen wurden erreicht durch (i) die Verwendung eines III/V Flussverhältnisses größer eins zur Kompensation von Ga-Desorption, (ii) die Verwendung des oben beschriebenen Zwei-Schritt-Ansatzes sowie (iii) durch die Einführung einer AlN-Pufferschicht, welche die GaN-Nukleationsbarriere senkt. Die GaN-Nanodraht-Ensembles, welche bei bisher unerreichten Wachstumstemperaturen gezüchtet wurden, weisen schmale exzitonische Übergänge mit sub-meV Linienbreiten auf, vergleichbar zu denen freistehender GaN-Schichten, welche nach dem aktuellen Stand der Technik der Hydridgasphasenepitaxie fabriziert wurden.

Abschließend wurden Nanodrähte mit Durchmessern deutlich unterhalb von 10 nm, dem unteren Limit herkömmlicher selbstinduzierter GaN-Nanodrähte, fabriziert. Mithilfe eines Zersetzungsschrittes im Ultrahochvakuum direkt im Anschluss an die Wachstumsphase wurden reguläre Nanodraht-Ensembles verdünnt. In-situ Prozesskontrolle durch Quadrupolmassenspektroskopie ermöglichte hierbei die genaue Steuerung des finalen Nanodrahtdurchmessers. Die resultierenden ultradünnen Nanodrähte weisen dielektrisches Confinement auf, welches potentiell viel stärker ist als reguläres Quantenconfinement. Wir zeigen eine ausgeprägte exzitonische Emission von puren GaN-Nanodrähten mit Durchmessern bis hinab zu 6 nm. Der große dielektrische Kontrast zwischen Nanodraht und Vakuum verstärkt die Coulomb-Wechselwirkung, wodurch die dünnsten Nanodrähte das stärkste Confinement und die höchste Strahlungseffizienz bei Raumtemperatur aufweisen. Diese ultradünnen Nanodrähte könnten einen Ausgangspunkt für die Fabrikation hochentwickelter niederdimensionaler Strukturen mit einem bisher unerreichten Confinement darstellen.

Stichwörter: Gallium Nitrid, GaN, Nanodrähte, Nanosäulen, Molekularstrahlepitaxie, Selbstinduktion, Zwei-Schritt-Wachstum, Hochtemperatur, Photolumineszenz, Ultradünn, dielektrisches Confinement

Abbreviations

CCD	charge-coupled device
CVD	chemical vapor deposition
cw(-PL)	continuous-wave (photoluminescence)
FS-GaN	free standing Gallium Nitride
FFT	fast Fourier transform
FX	free exciton
FWHM	full width at half maximum
HVPE	hydride vapor phase epitaxy
LD	laser diode
LED	light-emitting diode
MBE	molecular beam epitaxy
MOCVD	metalorganic chemical vapor deposition
μ-PL	micro-photoluminescence
NBE	near-band edge (luminescence)
NW	nanowire
PA-MBE	plasma-assisted molecular beam epitaxy
PL	photoluminescence
QMS	quadrupole mass spectrometry
RHEED	reflection high-energy electron diffraction
SAG	selective area growth
SEM	scanning electron microscopy
TRPL	time-resolved photoluminescence
UHV	ultra-high vacuum
VLS	vapor-liquid-solid
VSS	vapor-solid-solid
XRD	X-ray diffraction

Contents

1. Introduction

The technological revolution in the last century has strongly influenced modern life. Electronic and optoelectronic devices have played a major role in these developments. Electronic switches, amplifiers, memory, and sensors have enabled the development of integrated circuits, computers, smartphones, roboters and many more. Light-emitting diodes have led to the realization of bright and efficient indicators, signals, displays and lamps. Photodiodes have enabled digital cameras and are used in many other applications.

The foundation of the success of these devices is the ability to produce semiconducting material with high structural perfection in large volumes. The synthesis of pure, single crystalline semiconducting materials usually is a fundamental prerequisite for electronic devices to function efficiently.

For the material systems of Si, Ge, SiC, III-Vs, this prerequisite has been fulfilled for decades and therefore many different applications based on these materials have hit the market. In that case, continuous enhancements and further developments are mostly achieved by optimizing fabrication, design and principle of the respective devices.

For GaN and the group-III nitrides (III-N) in general, the case is different. First commercial LEDs based on GaN were announced only in 1993. The structural quality of GaN layers in current LEDs is still far from comparable to Si technology. Despite these shortcomings, GaN has enabled solid-state lighting which is currently underway to revolutionize how man enlightens his environment and may thereby severely reduce our global power consumption. Thus, GaN has become one of the most important semiconductors after Si in only 20 years. However, there are a lot of open questions remaining to be answered. The fabrication of inexpensive bulk GaN substrates with a high structural quality is maybe the most important one. For GaN LEDs, mastering the decrease in efficiency for higher currents is a similarly important task. In addition, the III-Ns are highly interesting for other applications such as UV-LEDs and high power electronics or also for photodetectors and in solar water splitting.

The fabrication of GaN in the form of NWs has the potential to yield improved and novel devices while at the same time making possible a direct integration with Si technology. Usually being free of dislocations, their excellent crystal quality distinguishes GaN NWs from planar epitaxial layers. In NW LEDs, vertically oriented active regions fabricated in shells around the NW core may lead to an improved integration density compared to planar epitaxy. Moreover, NWs have the potential to realize novel device concepts where the third dimension is actively used in device design, e.g. for confining zero- or one-dimensional excitons.

GaN NWs, spontaneously formed in molecular beam epitaxy, have received considerable attention in the last decade. At the moment, spontaneously formed GaN NW ensembles outcompete selective-area-grown NW arrays in terms of structural and optical quality, in terms of process cost, as well as achievable minimum NW diameter. While SAG NW arrays are industrially more relevant because of their more uniform and ordered morphology, spontaneously formed NWs are of importance both for fundamental studies on the GaN NW system and as a reference system for what may be one day achieved with improved SAG NW arrays.

However, also the spontaneous formation of GaN NWs is far from being completely understood and optimized. Several fundamental limitations concerning the control of NW morphology and the usable growth conditions have been agreed upon in literature. Specifically, the used growth conditions simultaneously affect the average NW diameter as well as the NW nucleation rate. The minimal achievable average NW diameter is limited by the shape transition occurring during NW nucleation. Although being lower than for SAG NWs, is still significantly higher than what would be required to achieve lateral quantum confinement due to a small Bohr radius in GaN of 3 nm. Analogously, the achievable growth temperature is limited by the severely decelerated nucleation of NWs at high temperatures. A higher growth temperature is expected to lead to an improved structural quality of the GaN crystal. The third parameter that cannot be controlled in spontaneous NW formation as desired is the NW number density. Typically, high number densities are obtained that result in a high area fraction of the substrate covered by NWs. This high area coverage leads to a high degree of NW coalescence which in turn introduces structural defects. Simultaneously, it prevents core-shell growth concepts due to the shadowing of the impinging fluxes by adjacent NWs.

The present thesis is devoted to the optimization of spontaneously formed GaN NWs ensembles in molecular beam epitaxy. By employing unconventional growth schemes, experiments are performed that aim to overcome the fundamental limitations introduced above. Thereby, not only GaN NWs ensembles of unprecedented properties are obtained, but also the understanding of the process of spontaneous GaN NW formation is broadened.

Following this introduction, a general overview to the GaN material system is given in Chapter 2 starting out with an outline of the technological relevance of GaN. Then, the basic properties of GaN that are of relevance in this work are summarized. After discussing the remaining challenges to GaN-based devices, nanowires will be presented as an alternative to conventional planar epitaxy including a discussion of their differences and advantages.

In Chapter 3, the methodological and contentual background of this work is explained. Along with a brief introduction to molecular beam epitaxy, the specific experimental conditions used for the preparation of the samples described in this thesis are given. Subsequently, the analytical techniques utilized to characterize our NW ensembles are described. While reflection high-energy electron diffraction and line-of-sight quadrupole mass spectrometry enable an in-situ monitoring of NW growth, the statistical shape analysis of scanning electron micrographs, x-ray diffraction and photoluminescence spectroscopy facilitate the comprehensive determination of their morphology, their optical and structural properties.

As a starting point with regards to GaN NW growth itself, a concise review of the most important studies will be given attempting to draw a well-comprehensible picture of their spontaneous formation. Then, recent reports on the impact of the growth conditions on NW formation and growth are recapitulated. As a result, the fundamental limitations of the spontaneous formation of GaN NWs as already briefly mentioned above will be discussed. The remainder of this work will then focus on overcoming these limitations.

In Chapter 4, a two-step growth approach is presented. This approach introduces different growth conditions for the nucleation and elongation of the NWs. Thereby, we attempted to gain improved control over the morphology of the NW ensemble, namely coalescence degree, number density, and area coverage. While some degree of control over the area coverage and coalescence degree is obtained, the number density of long

homogeneous NW ensembles remains high. A reduction in number density is only observed for growth conditions where the growth is stopped before NW nucleation has finished and comes at the price of NWs very inhomogeneous in height. As a result of these experiments, it is deduced that the high number density of spontaneously formed GaN NWs is the consequence of an ensemble phenomenon where NW nucleation can only decelerated but not stopped before the self-induced saturation. In another implementation of the two-step growth approach, we show that we can significantly reduce the growth time of GaN NW ensembles without affecting their structural or optical properties by eliminating the incubation time that usually preceeds NW growth.

Chapter 5 deals with the spontaneous formation of GaN NWs at so far unprecedented growth temperatures. Using three unconventional growth approaches, we enable GaN NW growth at up to 900°C. These growth approaches include the use of nominally Ga-rich growth conditions, the two-step growth approach discussed above, and on the introduction of buffer layers to lower nucleation barrier. Along with the higher growth temperature, we observe the onset of Si melt-back etching and thermal decomposition occurring during NW growth. The optical and structural properties of these high-temperature NWs, however, outscore all previous reports on spontaneously formed GaN NWs. The linewidth of the excitonic transitions of our high-temperature NWs prove that their structural quality is comparable to that of state-of-the-art free-standing GaN layers. In addition, we also report for the first time on the spontaneous formation of GaN NWs on 6H-SiC(000$\bar{1}$) both at conventional and high growth temperatures.

In Chapter 6, we overcome the last and most important limitation of spontaneously formed GaN NWs, namely, the impossibility to grow GaN NWs with diameters below 15 nm. As the diameter cannot be reduced by means of tailored growth conditions, we employ a post-growth decomposition step, where the NWs are partially reevaporated in the MBE chamber. Thereby, they reduce in length and diameter transforming to ultrathin NWs with a tapered morphology exhibiting tip diameters down to 5 nm. While their dimensions are still too large to allow quantum confinement, we show that dielectric confinement plays an important role and induces zero- and one-dimensional excitons in these ultrathin NWs. These findings will make possible the development of new classes of devices based on GaN NWs such as single-photon emitters and lead to a renewed interest of the scientific community in GaN NWs. If the post-growth decomposition step is conducted long enough, eventually also the number density of the remaining ultrathin GaN NWs is reduced. Thus, core-shell growth on spontaneously formed GaN NWs in MBE may be finally realized.

Finally, Chapter 7 provides general conclusions drawn from the results presented in this thesis as well as an outlook for further improvements in controlling and tailoring the properties of GaN NW ensembles prepared in MBE.

2. The GaN material system

In this chapter, a brief introduction to the GaN material system will be given to classify this work into broader context for the thematically less specialized reader. Despite GaN having already developed into one of the most important semiconductor materials for device applications after silicon in the last 25 years, this thesis is rather a fundamental study on the growth of GaN in the form of nanowires. These NWs, in turn, may lead to many improved or new devices and applications. For a more detailed treatise on GaN, the reader is directed to the handbook by Morkoç.[1] For information on the physics of semiconductor devices, the book by Sze and Ng is advised.[2]

In Section 2.1, the historic path leading to the development of the blue LED is traced. Due to this invention, GaN has evolved to one the most important material systems in modern technology. In Section 2.2, the most important properties of GaN that are of relevance in this work are summarized. Afterward, recent progress made on GaN devices is outlined in Section 2.3. Finally, in Section 2.4, nanowires will be introduced and compared to conventional epitaxial films.

2.1. The development of the blue light-emitting diode

In the last century, the development of semiconductor diodes and transistors based mostly on Si and Ge have enabled the triumph of electronics governing almost every aspect of today's life. In the field of optoelectronics, the role of Si and Ge is mostly limited to the detection side, i.e., in photodiodes and solar cells, due to their indirect bandgap.[4] For light emission, conventional III-V semiconductors such as GaAs, InAs, InSb, GaSb, and InP and their alloys have lead to the development of efficient red and infrared LEDs due to their direct bandgaps.[5] At higher energies, however, for green, blue and ultraviolet light, suitable materials systems were rare. AlAs, AlP, and GaP all have their bandgap in the green but exhibit indirect bandgaps in their typical zinc blende crystal structure.[6]

A suitable material system for optoelectronic applications, in terms of bandgap, are the group-III nitrides. Their bandgaps span the wide window from 0.7 eV for InN up to 6.2 eV for AlN. Their direct bandgaps facilitate efficient electron-hole recombination and make them a potential candidate for light emitting diodes in the infrared, visible, and ultraviolet spectral range. Their realization, however, was much more technologically demanding compared to that of Si electronics and conventional III-V semiconductors. First of all, the lack of a suitable well lattice-matched substrates prevented the early fabrication of high-quality GaN films. In addition, efficient p-type doping was difficult to achieve. Only in the late 1980s and early 1990s, reports on the fabrication of high-quality GaN films[7,8] as well as successful p-doping of GaN films[9,10] allowed to overcome the main technological obstacles. Soon after, the first blue LED was developed by Nakamura et al. in 1994.[11] These important results, paving the way toward today's triumph of white LEDs (compare Fig. 2.1) replacing incandescent light bulbs, were honored with awarding the Nobel prize of physics in 2014 to Isamu Akasaki, Hiroshi Amano, and Shuji Nakamura.[3]

GaN-based LEDs and lasers have encountered the center of society from many different

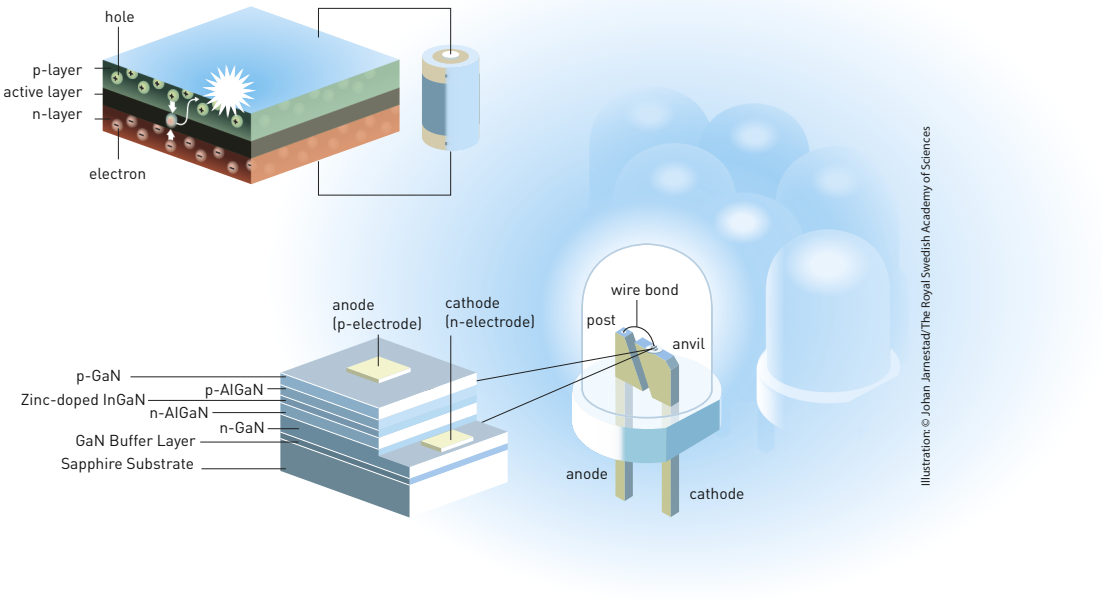

Figure 2.1: The functional principle of the blue LED as described by the Royal Swedish Academy of Sciences when awarding the Nobel Prize in Physics for 2014 to Isamu Akasaki, Hiroshi Amano, and Shuji Nakamura. Figure taken from the press release of the Royal Swedish Academy of Sciences.[3]

angles. They are, for example, used in lighting, data storage, automotive, or medical appliances.

2.2. Fundamental properties of GaN

GaN is a binary semiconductor composed to equal parts of the group III element gallium and the group V element nitrogen. Under ambient conditions, the thermodynamically stable crystal structure of GaN is wurzite.[1] The wurzite crystal structure has a hexagonal unit system described by two lattice constants, a and c. Per unit cell, there are six atoms of each type. The wurzite crystal structure consists of two interpenetrating hexagonal close-packed sublattices of Ga and N atoms, respectively.[1] The bonds between the Ga and N atoms are partially covalent.[1]

Figure 2.2(a) depicts the unit cell of wurzite GaN and the positions of the Ga and N atoms therein. As the wurzite crystal structure lacks an inversion plane perpendicular to the c-axis, GaN surfaces along c-direction have either a N or Ga layer as their utmost atomic plane as is illustrated in the figure. Due to the polar nature of wurzite GaN, it exhibits a spontaneous polarization in c-direction which is the common orientation for GaN epitaxy. When growing heterostructures, an additional piezoelectric polarization comes into play due to lattice mismatch. The interplay of both polarizations significantly influences the overlap of electrons and holes in quantum wells and thereby the performance of GaN-based optoelectronic devices. When examining III-N heterostructures, this interplay needs to be considered. In addition, Figure 2.2(b) depicts the non-polar A-plane ($\{11\bar{2}0\}$) and M-plane ($\{1\bar{1}00\}$) as well as the semi-polar R-plane ($\{1\bar{1}02\}$). These planes have only in

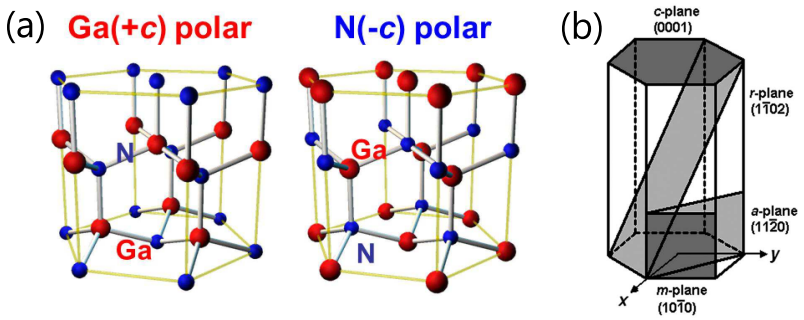

Figure 2.2: (a) Crystal structure of wurzite GaN oriented along +c and -c directions, known as Ga- and N-polar orientations. (b) Highlight of the polar C-plane, the non-polar A- and M-planes and the semi-polar R-plane. (a) Figure taken from Ref. [12]. (b) Figure taken from Ref. [13].

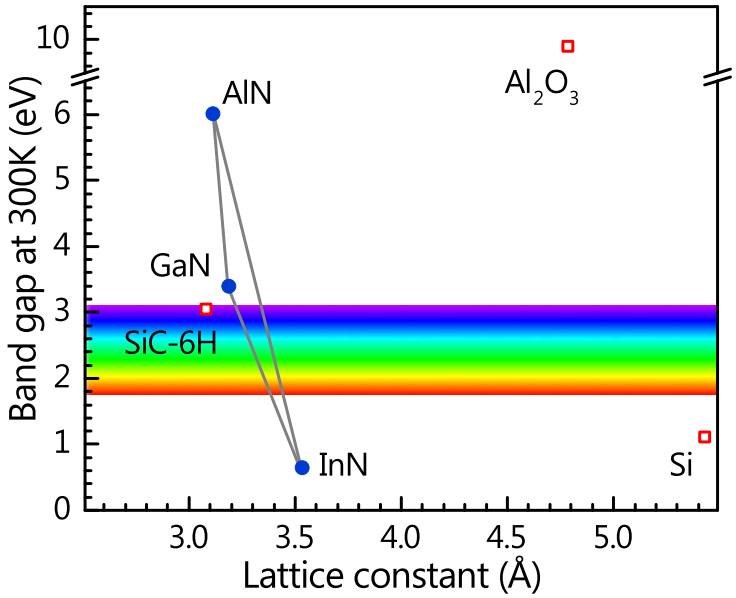

Figure 2.3: Energy band gaps of wurzite group-III nitrides (blue) and their commonly used substrates (red) versus the corresponding lattice constants.[1,15]

the last 15 years attracted significant scientific attention because the reduced or missing polarization along these orientations leads to an enhanced overlap of the electron-hole wavefunctions and thus an increase in recombination efficiency.[14]

The lattice constants *a* and *c* of wurzite GaN have been reported to be 3.189 Å and 5.1864 Å.[16] The Ga-Ga separation in bulk GaN, and therefore the monolayer thickness, is equal to 2.59 Å. Wurzite GaN has a direct band gap of 3.42 eV at ambient temperature. Together with AlN and InN it constitutes an alloy system that spans from the near infrared (0.65 eV for InN) to the ultraviolet (6.2 eV for AlN). Figure 2.3 depicts the band gaps of the wurzite III-nitrides versus their lattice constants. Also given are the corresponding (coincidence) lattice constants of the commonly used constant substrates for epitaxial growth of GaN: Si, Al_2O_3, and SiC. The graph directly points out the major drawback for III-N epitaxy – the lack of suitable, lattice-matched substrates. The lattice mismatch between GaN and Al_2O_3 is around 14%, the one between GaN and Si(111) around 17%. Only the expensive SiC exhibits a comparably lower lattice mismatch of 4%. GaN can be

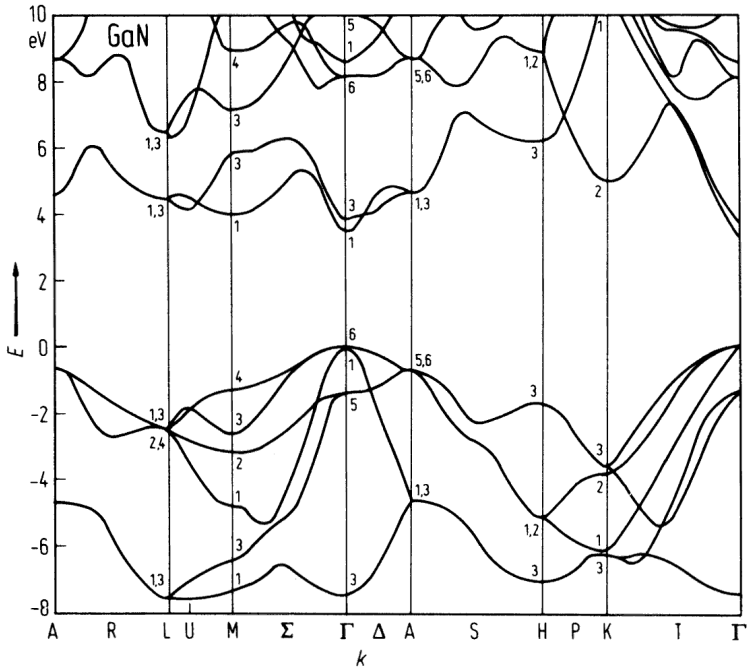

Figure 2.4: The band structure of wurzite GaN as calculated with an empirical pseudopotential method. Figure taken from Ref. [17].

doped to allow high carrier densities both n-type by using Si or Ge as dopants and p-type using Mg.

For the sake of completeness, Figure 2.4 gives the calculated band-structure of wurzite GaN. The band gap of GaN at 1.6 K is around 3.505 eV.[1] Dangling bonds at the surface result in surface states pinning the Fermi level at about 0.6–0.7 eV below the conduction band minimum for both M- and C-plane GaN.[18] The dielectric constant of GaN is about 8.9 at 300 K.[19]

For more detailed insights on the properties of GaN, the reader is advised to the book "Handbook of Nitride Semiconductors and Devices, Materials Properties, Physics and Growth" by Morkoç.[1] Complementary properties of GaN will be introduced along this work where necessary.

2.3. Recent progress and remaining challenges for GaN-based devices

In the last years, new methods have been developed for preparing high-quality free-standing layers and bulk GaN substrates by HVPE,[20] and high-pressure[21] as well as ammonothermal growth.[22] These layers exhibit dislocations densities down to 10^4 cm^{-2} and have facilitated further improvement of GaN-based LEDs.[23] In contrast, GaN layers that are prepared on Al_2O_3 or Si substrates usually exhibit threading dislocation densities of 10^8 cm^{-2} and above. In addition, free-standing GaN layers and bulk GaN substrates have enabled many advanced studies of the GaN material system itself. In terms of price, these substrates are, however, still very expensive and far from being suitable for large-scale industrial mass-production. Only for specialized applications such as high-power LEDs, commercial devices are realized on bulk GaN.[23]

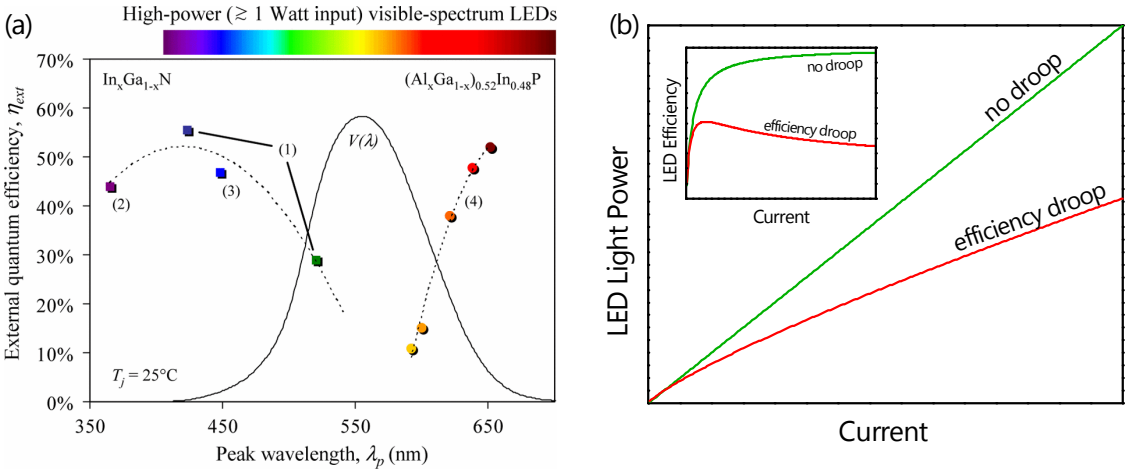

Figure 2.5: The main remaining challenges for GaN-based LEDs: (a) Filling the green gap, where human vision has its highest sensitivity, and (b) overcoming the efficiency droop at higher currents. The images were taken from Refs. [24](© 2007 IEEE) and [25], respectively.

However, there also remain challenges that have not yet been overcome. Although the (In,Ga)N alloy theoretically spans across the entire visible range, (In,Ga)N based LEDs have only been shown to efficiently function in the blue and violet, i.e., for low In contents. At longer wavelengths, the device efficiency rapidly decreases. This situation is known as the green gap because in the red efficient LEDs can be again manufactured on the basis of other, conventional III-Vs, namely AlInGaP.[24,26] The origin in the decrease of efficiency with increasing In content lies in the different properties of GaN and InN leading to phase separation and instabilitites and defects caused by the lattice mismatch between InN and GaN as well as again the lack of lattice-matched substrates.

Moreover, also blue and violet (In,Ga)N/GaN LEDs suffer from a characteristic decrease in efficiency for higher currents. This so-called "droop" is controversially discussed in literature to be either caused be electron leakage current[27,28] or auger recombination.[29–31]

In the case of deep UV-LEDs and laser diodes (LDs), the lack of suitable substrates and difficulties in p-type doping prevent the fabrication of efficient devices.[32]

In addition to optoelectronic applications, GaN-based devices also excel in purely electronic applications such as high-electron-mobility transistors (HEMTs), due to the high electron mobility in GaN and InN. Furthermore, III-Nitrides are used in Schottky diodes, HFETs, light harvesting technology, and intersubband transmitters.[1]

2.4. Nanowires, their differences and potential advantages over epitaxial films

Conventional epitaxy is the deposition of a crystalline layer where the atoms are in registry with the substrate. In order to build functional devices, fundamental epitaxial constraints have to be complied with. These constraints regard (i) the need for a low lattice mismatch between the layer and the substrate (or a suitable coincidence lattice) and (ii) the use of materials with comparable thermal expansion coefficients. Strain induced by the lattice mismatch may result in defect formation and thereby demolish the device performance. In extreme cases, it may prevent crystal growth in form of layers. When cooling down

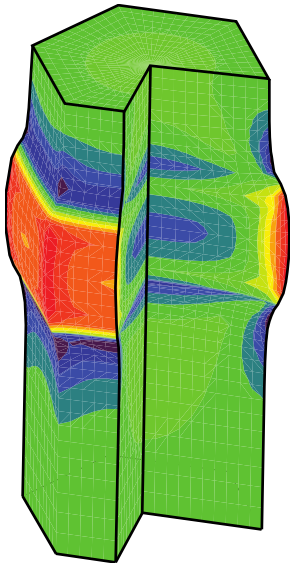

Figure 2.6: Finite element simulation of the strain relaxation in an axial quantum well embedded in a nanowire where the lattice constant of the quantum well is larger than that of the nanowire. Calculation by M. Hanke (PDI).

to room temperature after the epitaxy, the difference in thermal expansion of substrate and layers may lead to wafer bowing and eventually cracking. These epitaxial constraints limit the possible material combinations and realizable device concepts. With modern technology demanding for increased complexity to achieve advanced functionality, the concept of planar epitaxy with subsequent wafer dicing and device shaping in the backend process is not always feasible.

Nanowires may be one solution to overcome these fundamental constraints and pave the way to new and advanced devices. Note, that while some NWs can also be fabricated as whiskers along a given substrate, in this work we treat NWs that grow epitaxially perpendicular to the substrate, just as planar layers do. The main difference of NWs to layers is their lateral extent. Laterally individual NWs typically exhibit cross-section diameters of tens to low hundreds of nms. Depending on the fabrication process and their material system, their density may vary over several orders of magnitude. As a result of their limited lateral size, strain originating from either the lattice mismatch or thermal expansion may be relaxed elastically. Threading dislocations potentially forming at the interface remain there[33] or quickly bend toward the free sidewall surface.[34] Therefore, GaN NWs, for example, can be prepared on a wide variety of substrates independent of the lattice mismatch.[35–41] Analogously, axial heterostructures of larger lattice mismatch, e.g., (In,Ga)N insertions with higher In content, may be integrated without defect formation, because the strain can be elastically relaxed by deforming the NW sidewalls. Core-shell heterostructures, on the other hand, could increase the active area per chip and thus theoretically outscore planar layers. In addition, NWs are also interesting from a more fundamental point of view because they may allow the fabrication of defect-free GaN-based nanostructures such as (crystal phase) quantum dots.[42]

Nanowires can be prepared using different methods. The common mechanism is that the NW geometry is driven by a reduction in surface energy. For material systems like GaAs, InP, Si and others, NW growth usually proceeds in the vapor-liquid-solid mode that is enabled by a metallic particle that is used as a seed to induce local supersaturation and therefore uniaxial growth. GaN NWs may be synthesized using the VLS method as well but also form spontaneously, suitable growth conditions provided, without the need of a foreign catalyst. With their diameters on the order of tens of nms, GaN NWs

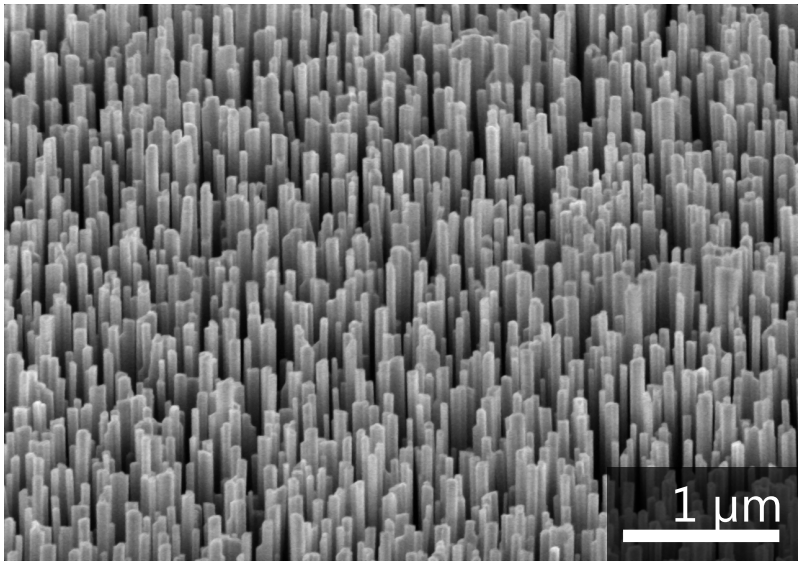

Figure 2.7: Exemplary scanning electron micrograph in tilted-view of GaN NWs prepared by molecular beam epitaxy.

are big enough to conduct electrons and holes comparably to bulk. Also the excitonic behavior remains bulk-like, as the diameters are significantly larger than the Bohr radius of the exciton in bulk GaN ($a_B = 3$ nm). However, the NW morphology also induces additional complexity, because the proximity to the NW sidewall surface effects the binding energy of donors[43,44] as well as the localization of electrons and holes in axial quantum wells.[45] If the NWs diameter could be further reduced, strong one- and zero dimensional confinement can be achieved which are of interest e.g., for single-photon emitters.

Summarizing, nanowires allow to overcome the fundamental constraints of planar epitaxy and may pave the way toward new devices as well as to explore physical phenomena in GaN. Especially, the group-III nitrides are highly interesting in this context as their alloy system spans a wide and interesting spectral range covering all three transmission windows of the existing telecommunication infrastructure (0.81, 1.31, and 1.55 µm), the entire visible range, as well as up to UV-C which is currently highly demanded for environmental sensing application and water disinfection as well as in curing, 3D-printing and fire detection.[32]

3. Growth and analysis of GaN nanowire ensembles prepared by plasma-assisted molecular beam epitaxy

Catalyst-free GaN NWs have been synthesized using different techniques such as metalorganic chemical vapor deposition,[46,47] hydride vapor phase epitaxy,[48] and molecular beam epitaxy.[35,49] In research, the most common growth technique for fundamental studies on GaN NWs is molecular beam epitaxy. The ultra-high vacuum conditions of MBE permit the monitoring of NW growth using several in situ techniques. For the still quite young field of GaN NW growth, these techniques are essential tools for fundamental studies on the growth and properties of these NWs.

In this chapter, we will introduce the essential tools and background knowledge required for GaN NW growth in MBE and for following the experiments made in this thesis.

In Section 3.1, we will provide a basic introduction to molecular beam epitaxy. Furthermore, we will clarify the usual preparation and calibration steps conducted for fabricating the samples presented in this thesis.

In Section 3.2, we will introduce and explain the functional principles of the in situ monitoring methods used: reflection high-energy electron diffraction and line-of-sight quadrupole mass spectrometry followed by the ex situ analyses that were performed to characterize the properties of our samples in detail after removing them from the MBE chamber: the statistical analysis of scanning electron micrographs, strain analysis based on x-ray diffraction as well as photoluminescence spectroscopy.

In Section 3.3, we will focus on the growth of GaN NWs itself. First, the most important studies reported on GaN NW growth by MBE will be reviewed in Section 3.3.1, attempting to draw a well-comprehensible picture of the current understanding of GaN NWs. This picture was recently extended by Fernández-Garrido et al. based on research ongoing at the Paul-Drude-Institut at the time this thesis was started. As summarized in Section 3.3.2, by systematically monitoring GaN NW growth in situ using QMS, the nucleation and growth in spontaneous NW formation could be modeled. These and other recent findings lead to a better understanding of the mechanisms controlling spontaneous GaN NW formation. Thereby, also the origins of the limitations of the spontaneous formation of GaN NWs as presented in Section 3.3.3 were identified. The limitations concerning number density, coalescence, diameter and growth temperature reduce the prospects of spontaneously formed GaN NWs. Overcoming them and thereby achieving better control over the morphology, obtaining better and novel variations of GaN NWs will be the essential goal of this thesis and pursued throughout the following chapters.

3.1. Plasma-assisted molecular beam epitaxy (PA-MBE)

GaN crystals can be synthesized using many different growth techniques. Crystal growth from solution and HVPE are primarily used for the production of thick GaN layers:

the former for bulk crystals, the ladder for free-standing GaN layers and thick GaN epitaxial layers. Bulk GaN exhibits the highest structural perfection demonstrated for GaN crystal layers and thus has led to a deeper investigation and a better understanding of the inherent properties of GaN. However, owing its high production cost, it is still far from being suitable for wide-spread industry scale device production. For the fabrication and investigation of GaN based optoelectronic devices, mostly MOCVD and MBE are used as they enable the formation of sharp heterostructure interfaces as well as high-purity and well-controlled n- and p-type doping. Often, for the fabrication of high-quality devices, HVPE buffer layers are overgrown by MBE and MOCVD. MOCVD is preferred in device production industry as it provides a better material quality due to a higher growth temperature, enables higher growth rates and requires substantially shorter maintenance periods. MBE enables the fabrication of superior interfaces and offers more in situ monitoring options not available in MOCVD. It is primarily used for academic research, but for specialized applications also in industry.

In MBE, crystal films are formed from molecular beams impinging on a heated substrate in base pressure ultra-high vacuum (UHV). The operating pressure can be as high as 10^{-4} Torr in UHV. These low pressure conditions are required to enable a mean free path of the molecular beams long enough to directly reach the substrate. Most source materials can be thermally evaporated using conventional effusion cells. In MBE conditions, ground-state molecular nitrogen by itself does not provide enough energy to form GaN.[51] As the dissociation of a nitrogen molecule into two reactive atoms however cannot be thermally achieved in MBE, primarily plasma sources are used to generate excited N_2 molecules and N atoms. As a consequence, the remaining molecular nitrogen leads to a high background pressure on the order of 10^{-5} mbar during III-N growth in MBE. The switching of the impinging molecular beams is controlled by shutters.

On the substrate surface, crystal growth is governed by the interplay and competition of adsorption and desorption processes, surface diffusion, nucleation and decomposition. Most of these processes are thermally activated and can thus be controlled via the substrate temperature. In addition, the absolute and relative rates of the impinging fluxes strongly influence crystal growth.

The GaN NW ensembles presented in this thesis were synthesized in a custom-built MBE chamber fabricated by CreaTec Fischer & Co. GmbH. The vacuum conditions in the growth chamber are maintained by two turbomolecular pumps as well as an ion getter pump. In addition, a cryo shroud inside the growth chamber which is filled with liquid nitrogen is used to condense residual vapors. During growth experiments, the valve connecting the ion gatter pump and the growth chamber was closed to protect the pump from the high background pressure caused by the molecular nitrogen. Attached to the growth chamber is a preparation chamber, which in turn connects to a load lock as well as a sputtering chamber. The load lock is used for the loading and unloading of samples. In the sputtering chamber, titanium can be sputtered onto the backside of transparent substrates in order to improve their heat absorption.

The majority of the samples presented in this thesis were grown on 2″ Si(111) substrates. Prior to loading, the as-received Si substrates were etched using diluted (5%) HF. After loading, the substrates were heated to 200°C in the load lock to evaporate residual water.

Ga was thermally evaporated from a Knudsen effusion cell heated to temperatures between 800°C and 930°C. The impinging Ga flux was measured regularly using an ion gauge whose filament was moved to the position where the substrate is located during growth. The fluxes were calibrated in GaN-equivalent growth rate units of nm/min,

as described in Ref. [52]. Here, a growth rate of 1 nm/min is equivalent to 7.3×10^{13} atoms/cm^{2}s. Prior to growth, the substrates were outgassed at 885°C for 30 min to remove any residual Si_xO_y from the surface. The substrate temperature was controlled using a thermocouple. In addition, it was measured with an optical pyrometer calibrated to the 1×1 to 7×7 surface reconstruction transition temperature of Si(111) (approx. 860°C).[53] Afterward, the substrates were exposed to an active nitrogen flux at the growth temperature for 10 min. The growth was then initiated by opening the Ga shutter. The active nitrogen flux used was $\Phi_N = 11.0 \pm 0.5$ nm/min for the samples presented in Chapters 4 and 5.1. For the samples presented in Chapters 5.2 and 6, a different nitrogen plasma source was used that supplied only $\Phi_N = 7.8 \pm 0.5$ nm/min.

The samples presented in Chapter 5.2 were grown on 10×10 mm SiC-6H(000$\bar{1}$) substrates. Before loading, those substrates were chemically cleaned in ultrasonic baths of n-Butyl acetate, acetone and ethanol and subsequently rinsed in deionized water. Prior to growth, the one-side polished SiC substrates were additionally backside sputtered with Ti. The thickness of the Ti layer was about 1 µm. Also, the substrate preparation in the growth chamber of the SiC substrates was different than for Si. As, in contrast to Si, a reaction of Ga with the substrate is not expected, the SiC substrates were cleaned using "Ga-polishing", using the gettering qualities of Ga. Here, 40 MLs of Ga were deposited at 550°C and flashed-off at a temperature of 900°C for 60 s to remove any residual SiO_2 from the surface. This procedure was repeated again before the growth was initiated. Since, in contrast to Si, there is no nitridation of the SiC when it is exposed to an active N flux, the N and Ga shutters were opened simultaneously to initiate growth.

For the intentional Si doping of NWs, a Knudsen cell filled with Si rods was used. The targeted doping concentration as a function of the cell temperature was obtained from SIMS measurements on planar calibration layers. For the NW ensembles, the doping concentration was corrected for the actual NW volume.

3.2. In situ and ex situ analysis of GaN NWs

The analysis of the prepared samples can be performed both in situ, meaning on site during the actual epitaxy process, and ex situ on the completed sample.

Owing to the UHV conditions, various techniques can be used to in situ monitor the growth. For the samples presented in this work, RHEED and line-of-sight QMS were employed. Using RHEED, the samples surface structure can be analyzed. Using line-of-sight QMS, the desorption of Ga during growth can be studied quantitatively. The in situ measurement tools were used to directly observe whether the new growth approaches and preparation methods of GaN NWs attempted in this thesis were fruitful. Furthermore, the detailed analysis of RHEED and QMS measurements facilitated a more comprehensive understanding of the underlying nucleation and growth mechanisms.

In order to further correlate the properties of the obtained NW ensembles to their growth conditions, several ex-situ analysis methods were employed. All of these methods were ensemble measurements averaging over hundreds to millions of as-grown nanowires, depending on the experiment. The statistical analysis of the NW cross-sectional shape obtained from scanning electron micrographs was used to objectively obtain the coalescence degree, the average diameter, as well as the number density of the prepared NW ensembles. X-ray diffraction experiments were performed to obtain knowledge about the epitaxial alignment of the NWs and to quantify the inhomogeneous strain existing in the samples. Continuous wave and time resolved photoluminescence experiments were

conducted to investigate the recombination dynamics present in the prepared samples and to correlate them to the growth conditions and the structural properties of the ensembles.

In the following, the basic principles of these in situ analytic methods will be introduced in Section 3.2.1, followed by an equivalent description of the main ex-situ analytic methods used in this thesis in Section 3.2.2.

At the end of each segment, the reader will be referred to suitable literature for more detailed information on the respective experimental method. For illustration, exemplary raw data of each method will be presented from a reference sample. This sample was prepared under growth conditions that are typical for the spontaneous formation of GaN NWs on Si(111), namely using a substrate temperature of 815°C and a III/V ratio of 0.5. In a total growth time of about 4 h, GaN NWs with a length of about 2.2 µm were formed.

3.2.1. In situ analytical methods

Reflection high-energy electron diffraction

RHEED is the diffraction of high-energy electrons during their reflection on the sample surface. It requires an electron gun to generate an electron beam which is aimed at the sample using a deflection unit. The kinetic energy of the produced electrons may very between 5 and 50 keV. In our case, their energy was about 20 keV. The electron beam is directed at grazing incidence onto the substrate resulting in a small penetration depth and thus enabling a sensitivity dominated by the atomic planes closest to the surface. The interaction area of the beam and sample governing the measurements is usually about 1 mm wide and between 1 and 2 cm long. The width is determined by the width and divergence of the electron beam, while the length is a result of the gracing incidence of the same. The reflected and diffracted electrons hit a fluorescent screen where their interference pattern can be monitored and recorded using a CCD camera. RHEED is widely used in MBE to investigate surface morphology, growth rates, crystal structure, surface reconstructions and epitaxial relations in heterostructures.

The diffraction patterns observed in RHEED correspond to the coincidence of the Ewald sphere with the reciprocal lattice of the sample. The Ewald sphere represents the allowed diffraction conditions of elastically scattered electrons conserving their energy and momentum. It is centered at the sample surface and its radius $k_i = 2\pi/\lambda$ is given by reciprocal wavelength of the incident electrons. Since solely the outmost atomic layers contribute to diffraction, only the two-dimensional surface structure of the crystal determines the coincidence conditions, while in the direction perpendicular to the sample surface the reciprocal lattice is constituted of infinite rods.

Thus for an ideal, single crystal, the diffraction pattern is given by spots. In reality the surface crystal imperfections, atomic steps and instrumental broadening lead to the observation of a streaky diffraction pattern for smooth surfaces. The distance between the streaks is given by the inverse of the lattice constant perpendicular to the plane of incidence. For high-quality crystal surfaces, surface reconstructions may appear, where energy minimization causes a single adatom layer to form with a periodicity different to that of the bulk crystal. A prominent example is the 7×7 surface reconstruction of Si(111), where an adatom is positioned on every 7^{th} crystal site both along the $[11\bar{2}]$ and the $[10\bar{1}]$ direction. In the case of rough surfaces, the electrons are additionally transmitting through the asperities which results in a spotty RHEED pattern.

For the growth of GaN NWs pursued in this work, RHEED was primarily used to identify the onset of NW nucleation. Figure 3.1 shows the typical diffraction patterns

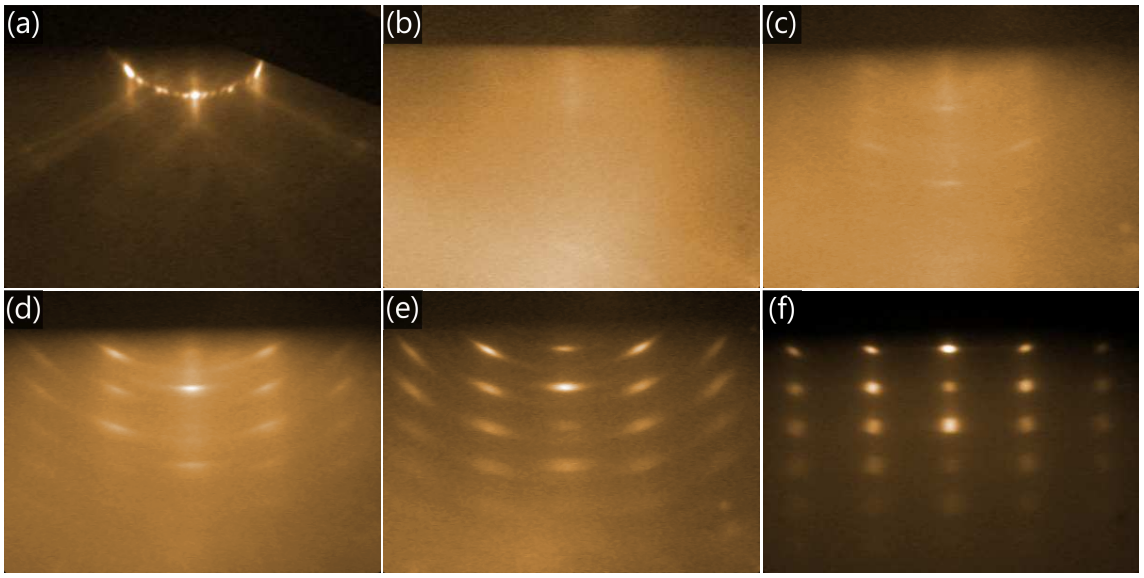

Figure 3.1: Typical evolution of RHEED pattern along [11$\bar{2}$0] azimuth during GaN NW growth: (a) 7 × 7 surface reconstruction of Si(111), (b) after nitridation of the substrate, (c) observation of the first GaN spots, (d) 10 min after the onset of nucleation, (e) 40 min after the onset of nucleation, and (f) after several hours of growth.

occurring in GaN NW growth on Si(111) along the [10$\bar{1}$] and [1$\bar{1}$00] azimuth of Si and GaN, respectively. As the substrate is usually rotated during growth, these images were not all taken during the same growth run, but rather gathered from multiple experiments using comparable growth conditions. Nevertheless, they serve the intention to illustrate the typical evolution of the RHEED pattern during the preparation of GaN NWs in MBE.

Figure 3.1(a) shows the 7 × 7 surface reconstruction of Si(111) prior to growth illustrating that a clean and sufficiently smooth Si surface was present. As mentioned earlier, the temperature-dependence of the 7 × 7 reconstruction, transitioning to a 1 × 1 structure at about 860°C,[53] furthermore enabled the calibration of the temperature measurements obtained from the thermocouple and the optical pyrometer. Figure 3.1(b) displays the RHEED image obtained after the nitridation of the substrate and during the incubation stage of NW growth. As the few nm thick Si_xN_y layer forming during nitridation is amorphous, only a diffuse halo is obtained, often super positioned with a weak streaky signal from the underlying silicon.

Once the first crystalline GaN NW nuclei form, their spotty pattern appears in RHEED in the form of ring segments.[50,54,55] The width of the segments is determined by the NW tilt. Figure 3.1 (c) gives the diffraction pattern immediately after the first GaN spots are observed. As NWs continuously nucleate, the overall intensity of the GaN-related spots increases until eventually saturating[54,55] [compare Figures 3.1(d) and (e), acquired 10 and 40 minutes after the onset of nucleation, respectively].

As will be discussed in detail in Section 3.2.2, a significant percentage of the NWs coalesces during growth owing to their high number density, their mutual misorientation, as well as radial growth.[56,57] This coalescence in turn leads to a reduction of the average tilt and twist of the NW ensembles, eventually resulting in a completely spot-like RHEED pattern. Figure 3.1(f) presents the RHEED pattern after several hours of growth during which a strongly coalesced ensemble of NWs has formed that have grown to a few µm length.

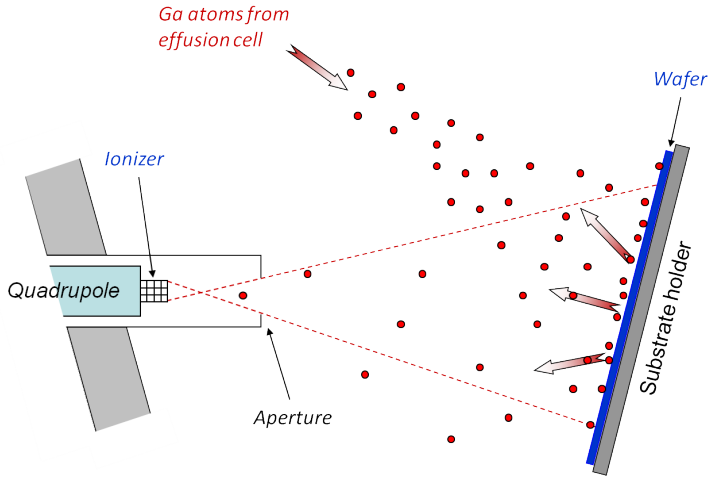

Figure 3.2: Sketch of the measurement configuration of line-of-sight quadrupole mass spectrometry in MBE.

In order to quantitatively describe NW growth using RHEED measurements, i.e., from the development of the GaN-related RHEED intensity, NW growth experiments would have had to be conducted without substrate rotation. As substrate rotation is crucial for the homogeneity and reproducibility of the NW samples, RHEED was primarily used (i) for substrate preparation, (ii) to identify the onset of GaN NW nucleation, and (iii) to estimate the progress of NW coalescence. For the quantitative description of GaN NW growth, in situ line-of-sight quadrupole mass spectrometry measurements were used. Following the recently developed model by Fernández-Garrido et al.[50], discussed in detail in Section 3.3.2, a superior description of the entire nucleation and growth processes was possible. For the quantitative analysis of tilt, twist, and strain occurring in our NW ensembles, ex-situ x-ray diffraction experiments were performed.

More details on the mechanisms of RHEED and its use in epitaxial growth can be found in Refs. [58, 59]. Further information on the RHEED patterns of GaN NW ensembles is given in Refs. [60–62].

Line-of-sight quadrupole mass spectrometry

Line-of-sight quadrupole mass spectrometry can be a powerful in situ tool for the monitoring of growth processes. The quadrupole mass spectrometer is usually positioned in a regular MBE cell port and focused on the substrate using a suitable aperture. Thus, it can be configured to measure atoms desorbing from the substrate during growth profiting from the long mean free paths in an MBE environment. This measurement setup is sketched in Figure 3.2. The area of the substrate not shielded by the aperture and thus contributing to the measurement signal is about 1.5″ in diameter. An area this large is required in order to achieve a good signal to noise ratio. Thus, for GaN growth in MBE, where Ga is partially desorbing during growth, the desorbing Ga flux Φ_{des} can be monitored in situ during the experiments. However, for growth experiments on smaller substrates, the measured Ga flux is desorbing from both the sample and the sample holder. Therefore, for the samples grown on SiC presented in Chapter 5.2, a reliable measurement of the desorbing Ga flux by QMS was not possible.

The QMS response was calibrated in equivalent growth rate units using a heated

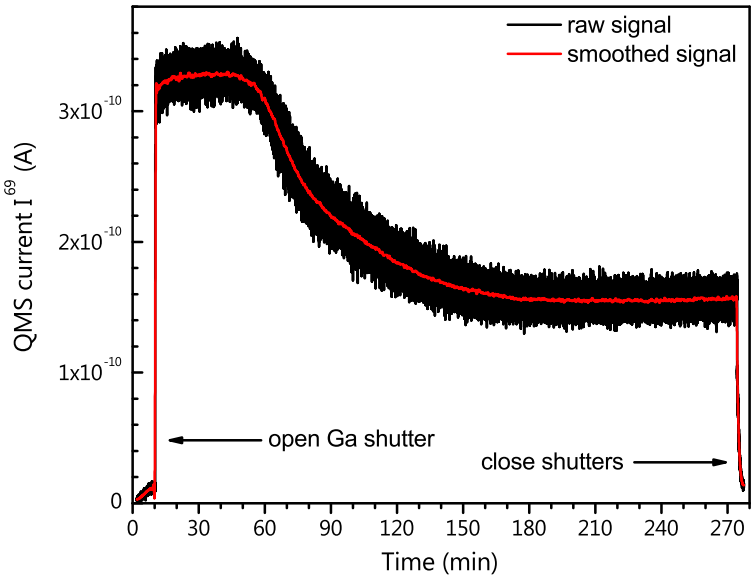

Figure 3.3: Temporal evolution of the desorbing Ga flux as measured during the growth of the NW reference sample.

sapphire substrate, where all impinging Ga is known to desorb at sufficiently high temperatures.[63,64] Thereby, the measured QMS signal can be correlated to the impinging flux as measured using an ion gauge. The correlation of the measurement flux to equivalent growth rate units is determined from a separate calibration sample. Since during GaN NW growth there is no Ga accumulation on the substrate,[65–67] the Ga incorporation rate per unit area Φ_{inc} was determined through $\Phi_{\text{Ga}} - \Phi_{\text{des}}$.

Figure 3.3 displays the raw data obtained from QMS during the fabrication of the reference sample. In the first 10 minutes of the experiment, the substrate is nitridated. As the Ga shutter is kept closed during nitridation, the signal measured at that time corresponds to the background signal. Once the Ga shutter is opened, the desorbing Ga flux is measured by the QMS. The temporal evolution of the desorbing Ga flux itself is discussed at a later stage (Section 3.3.2). At the end of the growth run, when the Ga shutter is closed again and the substrate temperature is decreased to room temperature, the signal quickly returns to the background level. Owing to the substrate rotation during growth and the inherent noise of the measurement, the raw measurement signal is usually very noisy. Thus, in a first processing step, a FFT filter was applied to remove the noise. The cut-off frequency was set equal to the one of the substrate rotation. The result is shown in Figure 3.3 as a red line. Later on the signal was converted to equivalent growth rate units[63,64] and the actual Ga incorporation Φ_{inc} was derived, as it was described above.

In this work, QMS was used to quantitatively monitor and analyze the nucleation, growth, and decomposition processes of GaN NWs. It enabled an in situ observation of the nucleation as well as the quantification of the average nucleation time and rate, crucial for further analysis of the prepared samples. The typical temporal evolution of the Ga incorporation during GaN NW growth in MBE will be discussed in Section 3.3.2. Then, also the numerical model using a double logistic function and its interpretations and consequences will be introduced.

Further information on the functionality of QMS and its use as an in situ tool for GaN NW growth in MBE can be found elsewhere.[50,61,63,64,68]

3.2.2. Ex situ analysis of GaN nanowire ensembles

Coalescence degree

Ensembles of spontaneously formed NWs usually exhibit a broad distribution in the properties of the single NWs (length, diameter). In addition, the very high density of the NWs inevitably leads to coalescence of adjacent NWs. As single NWs may be tilted and twisted with respect to each other, their coalescence potentially results in the formation of extended defects and inhomogeneous strain, significantly affecting optical and electric properties of the NW ensembles.[49,57,69–71] In order to objectively quantify the coalescence occurring in NW ensembles, the morphology of the obtained samples was analyzed using several plan-view scanning electron micrographs containing hundreds of NWs, as it was proposed by Brandt et al.[56] Using the open-source software ImageJ.[72], we determined the shape descriptors area A, perimeter P, and circularity C of all detected NW top facets, where C is defined as

$$C = 4\pi A / P^2. \tag{3.1}$$

Circles have a circularity of $C = 1$, for regular hexagons C equals 0.907. NW coalescence usually leads to shapes exhibiting lower values of C. As proposed in Ref. [56], we use a threshold value of $C < \zeta_A = 0.762$ to identify coalesced NW clusters. This value is obtained from the most symmetric conceivable shape of two regular hexagons coalescing, having their coalescence boundary parallel to the A-plane $(11\bar{2}0)$. Figure 3.4 depicts the circularities of selected typical NW shapes. Figure 3.4(d) represents the threshold condition described above.

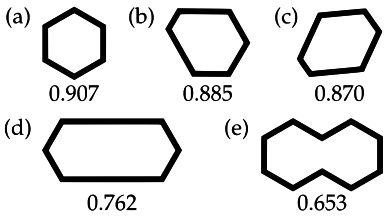

Figure 3.4: Selected cross-sectional geometrical shapes formed by M-plane facets and their circularity. Shapes originating from single nanowires are shown in (a)–(c). The shapes depicted in (d) and (e) are produced by the coalescence of two regular hexagons. For the former, the coalescence boundary is parallel to the A-plane, while it is parallel to the M-plane for the latter.

For very highly coalesced NW ensembles, the coalescence of multiple NWs may nonetheless lead to circularity values $C > \zeta_A$. This case may arise when multiple NWs cluster not in a line but rather bundle, thus composing again a roundish shape. Also, radial growth upon coalesence may result in higher values of C. In view of the fact that single NWs typically exhibit equivalent-disk diameters $d = 2(A/\pi)^{1/2}$ well below 100 nm,[73,74] unless otherwise indicated, we only consider as uncoalesced NWs those with $C > \zeta_A$ and $d < 100$ nm. The coalescence degree itself is calculated as the area fraction covered by coalesced NW aggregates A_C divided by the total area covered by NWs A_T, thus corresponding to the volume fraction that is "in contact" with coalescence boundaries.

$$\sigma_C = \frac{A_C}{A_T}, \tag{3.2}$$

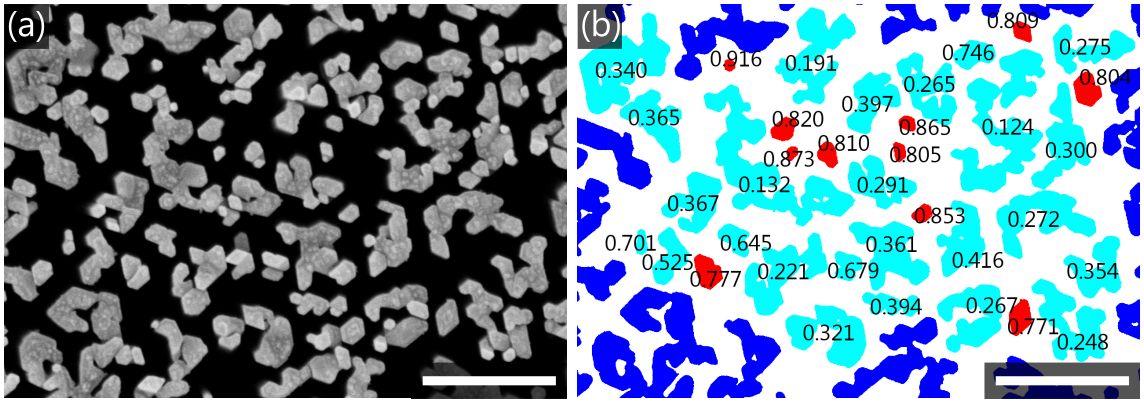

Figure 3.5: (a) Scanning electron micrograph of the reference sample in plan view. (b) NW aggregates identified by the analysis software. Blue: touching the edge of the image, unusable for shape analysis. Light blue: coalesced NW aggregates. Red: NWs with circularity values above the threshold value. For the objects not touching the edge, their circularity values are given. The scale bar corresponds to 1 µm. SEM measurements carried out by Anne-Kathrin Blum.

Figure 3.5(a) depicts a raw scanning electron micrograph of the reference sample in plan view. Prior to further analysis, the images were usually despeckled and their contrast was enhanced. The same is true for scanning electron micrographs later presented in this work. In addition, most of the scanning electron micrographs presented later in this thesis are colorized to enhance their contrast. For the shape analysis, the software then identifies all individual objects and determines their area, perimeter, and circularity. In Figure 3.5(b) three kinds of objects are color coded. Objects that touch the edge of the micrograph are marked in dark blue. These objects cannot be included in the analysis of the coalescence degree as neither their true area nor their true perimeter are known. For the determination of the area coverage and the total number density, however, also these objects have to be taken into account. Objects that do not touch the edge of the micrographs and exhibit circularities $C \leq \zeta_A$ are colored in light blue. These objects correspond to coalesced NW aggregates. Their circularity values are given in the figure. Objects exhibiting circularities $C \geq \zeta_A$ are marked in red. These objects are regarded as uncoalesced NWs given that their equivalent disk diameter is smaller than 100 nm. Also for these objects, the circularity values are given. For some of these objects in Figure 3.5, it is even by eye very difficult to discriminate whether these are single NWs or coalesced objects. For others like the ones with circularites of 0.777 and 0.804, however, it is obvious that these objects are the result of NW coalescence. The size limit introduced for uncoalesced NWs minimized the incorrect identification of these objects as their equivalent disk diameters are 114 nm and 113 nm, respectively. The same is true for the object with a circularity of 0.771 and a diameter of 106 nm.

Furthermore, we attempted to reliably determine the total number density of NWs ρ_{NW} independently of their coalescence degree. In order to automatically determine the number of single NWs any coalesced NW cluster consists of, we first determined the average area $\bar{A}$ of all identified uncoalesced NWs. Then, we divided the area of the cluster by $\bar{A}$ to estimate the integer number of NWs constituting each coalesced aggregate. In practice, the same result is obtained when dividing the total area covered by NWs A_{total} by the average uncoalesced NW area: $\rho_{NW} = A_{\text{total}}/\bar{A}$. However, due to poor statistics, for coalescence degrees approaching 100%, the inaccuracy in the determination of the

average area $\bar{A}$ of uncoalesced NWs inevitably leads to a lower accuracy of the obtained NW number density.

Further information on the shape analysis of NW ensembles can be found in Ref. [56].

In-plane and out-of-plane orientational distribution

The spontaneous formation of GaN NWs usually takes place on foreign substrates. Even though the lattice mismatch between NW and substrate may be substantial, GaN NWs generally show a well-defined epitaxial alignment to the substrate. However, the average NW tilt and twist of a given sample may strongly differ depending on the type of substrate used. Samples grown on Si(111) usually exhibit a significant distortion of the epitaxial alignment to the Si substrate. Why the epitaxial alignment to the Si is preserved at all, despite the amorphous interlayer, is not yet fully understood. Recent experiments suggest that GaN NWs initially nucleate at holes or grooves in between Si_xN_y patches. While small degrees of misalignment in coalesced NW aggregates may be accommodated elastically, larger tilt and twist will result in the formation of dislocated tilt/twist boundaries.[57,75] Coalescence is thus likely to induce inhomogeneous strain as well as nonradiative recombination.[49,57,69–71]

High resolution x-ray diffraction measurements were performed at room temperature using a Panalytical X-Pert Pro MRD^{TM} system using Cu Kα_1 radiation (wavelength $\lambda = 1.54056$ Å) and a Ge(220) monochromator. The x-ray beam profile is a few mm wide and about 2 cm long, probing a large area of the substrate containing several million NWs. XRD is based on the angle dependent measurement of the constructive interference of x-rays scattered by the electrons surrounding the atoms in the crystal lattice. Constructive interference occurs when Bragg's law is satisfied

$$n\lambda = 2d \sin\theta. \tag{3.3}$$

Here, d is the spacing between crystal planes and θ the angle of the incident monochromatic beam with respect to the normal to the crystal plane. Experimentally, the diffracted beam is measured at an angle of 2θ.

GaN NWs exhibit C-plane top-facets and usually M-plane sidewalls, thus the $[0001]$ axis is parallel to the growth direction. Therefore, ω-scans near the GaN 0002 reflection, using an open detector and a 1 mm slit, are used to determine the out-of-plane orientation distribution of the NWs. Here, the FWHM of the ω-scan directly gives the average tilt of the NWs. The in-plane orientation distribution on the other hand is determined from the FWHM of azimuthal ϕ-scans measured in skew geometry using the open detector and no slit. As a direct measurement with a sample tilted by 90° is impracticable for geometric reasons, the ϕ-scan was measured along the $10\bar{1}5$ reflection tilted by $\chi = 20.58°$ with respect to the sample surface. The average NW twist, assessed as the FWHM $\Delta\phi_{90°}$, that would be obtained at 90°, was then extrapolated according to

$$\Delta\phi_{90°} = \frac{\Delta\phi_{10\bar{1}5} \cdot \sin\chi}{1 - \Delta\phi_{10\bar{1}5}/360°}, \tag{3.4}$$

where $\Delta\phi_{10\bar{1}5}$ is the FWHM measured in the $10\bar{1}5$ reflection.[69]

The strain state of the samples was determined from $\theta/2\theta$ scans around the 0002, 0004, and 0006 reflections using the analyzer. While the positions of the respective reflections indicate that the NW ensembles are free of homogeneous strain (i.e., $< \varepsilon_{zz} >= 0$, where

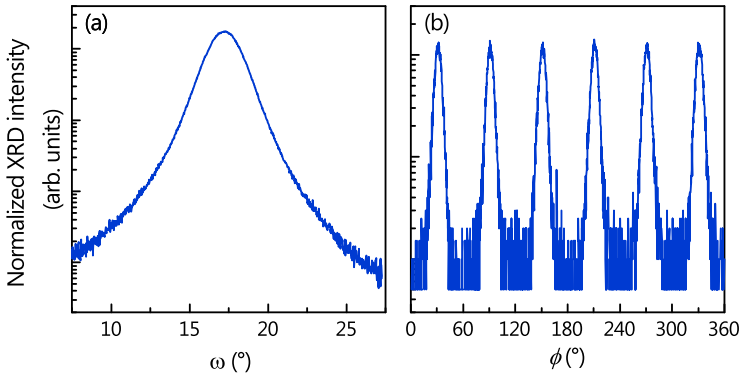

Figure 3.6: (a) X-ray diffraction scan of the reference sample across the 0002 reflection measured along ω to determine the average NW tilt from the FWHM. (b) Azimuthal ϕ scan across the $10\bar{1}5$ reflection in skew geometry from which the average NW twist can be obtained.

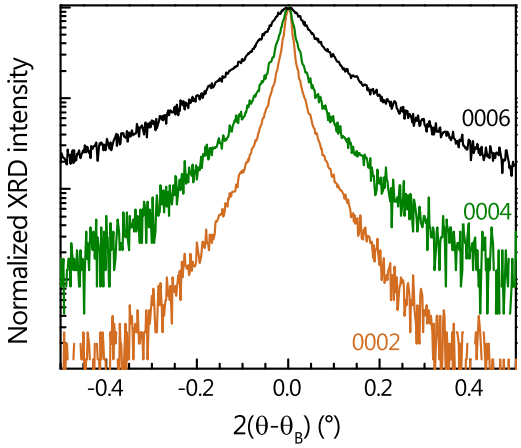

Figure 3.7: X-ray diffraction scans of the reference sample in the $\theta/2\theta$ configuration measured for the 0002, 0004, and 0006 reflections. From the increase on the broadening of these peaks the inhomogeneous strain can be derived.

$< \varepsilon_{zz} >$ is the zz-component of the strain tensor), their linewidth usually increases with the reflection order. This broadening is an indication of inhomogeneous strain also known as micro-strain $\mathcal{E} =< \varepsilon_{zz}^2 >^{1/2}$. The magnitude of $\mathcal{E}$ is obtained from Williamson-Hall Plots $\beta_f^* = f(d^*)$ in the reciprocal representation. Here, β_f^* is given by $\beta_f^* = \beta_f' \cos\theta/\lambda$, where β_f' is the integral breadth of the reflection corrected for the breath of the resolution function. The integral breadth is defined as the ratio of the area and the height of a peak. As the strain is related to the increase in the broadening, it is obtained from the slope of a linear fit to $\beta_f^* = \beta_s^* + 2\mathcal{E}d^*$, where β_s^* gives the contribution to the broadening due to size effects.[69]

Figure 3.6 shows the raw ω and ϕ scans of the reference NW sample used to obtain the tilt and twist distribution, respectively. Figure 3.7 depicts the normalized x-ray diffraction scans of the reference NW sample in the $\theta/2\theta$ configuration measured for the 0002, 0004, and 0006 reflections. Taking into account the apparatus resolution function, the inhomogeneous strain can be derived from the increase on the broadening of these peaks

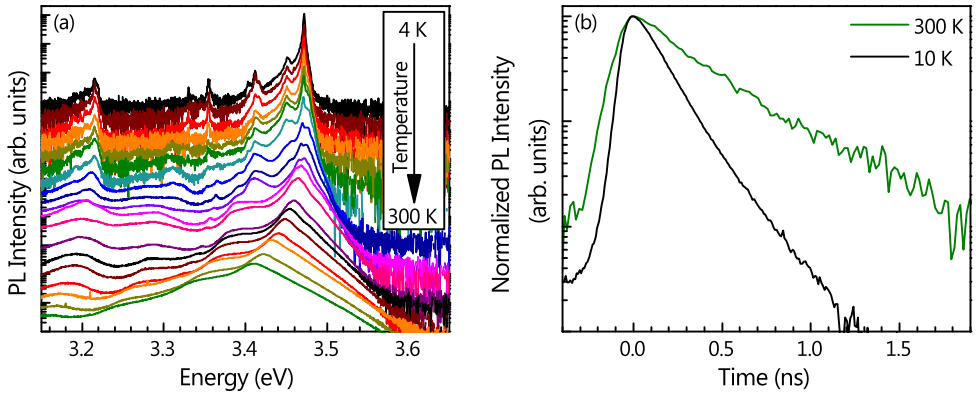

Figure 3.8: Raw spectra obtained from µ-photoluminescence measurements of the reference sample. (a) cw PL measurement at temperatures varying between 4 K and 300 K. (b) TRPL transients at 10 K and 300 K. PL measurements carried out by Pierre Corfdir and Christian Hauswald.

as described above. More detailed information on the x-ray diffraction on GaN NWs can be found in Refs. [69, 70, 76].

Luminescence

The continuous-wave (cw) and time-resolved (TR) micro-photoluminescence (µ-PL) experiments presented in this work were carried out by Pierre Corfdir and Christian Hauswald. The cw-PL measurements were carried out using a He-Cd laser ($\lambda = 325$ nm) with an excitation density below 150 nW/µm^2. The luminescence was dispersed by an Horiba Jobin Yvon monochromator (80 cm focal length, 2400 lines/mm) and detected by a charge-coupled device detector. For the TR-PL measurements, the second harmonic ($\lambda = 325$ nm) of fs pulses obtained from an optical parametric oscillator pumped by a Ti:sapphire laser was used to excite the NW ensembles. The energy fluence per pulse was kept at around 1 µJ cm^{-2}. The luminescence was dispersed using a monochromator (22 cm focal length, 1800 lines/mm) and directed onto a streak camera with a temporal resolution of 50 ps, operated either in synchroscan or in single sweep mode. For both cw- and TR-PL measurements, the samples were mounted in a cold finger cryostat whose temperature was varied between 10K and 300K. For all µ-PL measurements, the excited area of the as-grown samples covered more than 100 NWs.

Figure 3.8 shows the corresponding spectra of the reference sample. In Figure 3.8(a) the cw PL spectra at temperatures varying from 4 K to 300 K are shown. The dominating exciton and defect-related peaks can be resolved and their shift with temperature toward lower energies becomes apparent. The low-temperature spectrum is dominated by the recombination of A excitons bound to neutral donors [(D^0, X_A)] at 3.47 eV. The shoulder on the high-energy side of the (D^0, X_A) peak is due to emission from B excitons bound to neutral donors [(D^0, X_B)] at 3.474 eV and from free A excitons (X_A) at 3.478 eV. Towards lower energies, we observe so-called so-called UX band[43,77–80] [(U, X_1), (U, X_2)] at 3.45 eV, emission from excitons bound to I_1 basal plane stacking faults at 3.41 eV [(I_1, X)][44,81], and the Y_7 band at 3.21 eV.[82,83] In between, weak lines that correspond to the first LO-phonon replica of the (I_1, X) transition can be found. Figure 3.8(b) depicts the TRPL transients of the reference sample measured at 10 K and 300 K. In general, from

these measurements many conclusions can be drawn, e.g., concerning the incorporation of donors and defects, the presence of strain, or the dominating exciton recombination processes.

As this work is focused on the growth of the NW structures, the experiments on the optical properties of the obtained NW structures will not be treated in full detail. For more extensive examinations of the optical properties of the same or similar samples, the reader is advised to Refs. [42, 78, 84–87]

3.3. Growth of GaN nanowires in PA-MBE

The next section will deal with the fabrication of GaN NWs in MBE. First, a brief historical review on the important findings in GaN NW growth will be given. Then, based on the recent progress in monitoring the formation of NWs by QMS,[50] an albeit subjective attempt will be made to summarize the current understanding of the mechanisms governing the spontaneous formation of GaN NWs in MBE. Finally, the limitations in ensemble morphology and substrate temperature inherent to this spontaneous formation will be pointed out. In the following chapters, methods will be developed to overcome these limitations and fabricate GaN NWs with unprecedented properties.

3.3.1. Previous work (Review)

In crystal growth, the concentration of point defects depends strongly on temperature. Their concentration is high at low temperature due to limited kinetics, as well as at high temperature where entropy governs the defect equilibrium concentration. A minimum concentration of point defects is obtained at intermediate temperature. For covalently bonded semiconductors, this optimal growth temperature has been theoretically predicted to be close to half of their melting point.[88,89] For GaN, the melting point temperature has been established at 2540 K.[90] Accordingly, the optimal temperatures used in vapor based epitaxial growth techniques such as MOCVD or HVPE are around 1300 K.[91–93] In MBE, however, the maximum achievable temperature for the growth of GaN films is limited by thermal decomposition because GaN is thermodynamically unstable at pressures typical in the molecular beam regime ($< 10^{-4}$ Torr).[51,94,95] Furthermore, in PA-MBE, to promote step-flow growth and obtain smooth GaN films, maintaining a surfactant Ga-adlayer on the surface is required.[52,96–98] Due to the exponential increase of Ga desorption with substrate temperature,[52] this requirement implies an additional temperature limitation. For these reasons, the typical substrate temperatures reported for the growth of GaN films by PA-MBE are around 1000 K.[52,98] This value is well below the previously stated optimum.

When GaN films are prepared without the surfactant Ga-adlayer, i.e., when decreasing the III/V flux ratio and eventually using N-rich growth conditions, the growth mode first changes to layer-by-layer and later to three-dimensional growth due to insufficient surface diffusion, resulting in the formation of a rough surface.[98,99] For growth temperatures above 750°C, thermal decomposition of GaN comes into play. Thus for the growth of GaN films, the rate of GaN formation needs to exceed the rate of decomposition.[98]

The formation of self-organized GaN NWs was first reported on by Yoshizawa et al. in 1997 and Sánchez-García et al. in 1998.[35,49] Both groups investigated the formation of GaN layers in MBE on dissimilar substrates, Al_2O_3(0001) and Si(111), respectively, at comparatively high growth temperatures. They detailed that the resulting layers exhibit

a columnar structure when prepared in significant N excess. However, almost 10 years passed before this pioneering work inspired several other scientific groups to work in the field of GaN NW growth by MBE.

An important distinction to note at this point is that the formation of GaN NWs significantly differs to the fabrication of NWs in other material systems. Commonly, the synthesis of NWs is either based on catalyst seeds or on templates or prepatterned masks. The spontaneous formation of GaN NWs requires neither foreign seed materials nor prepatterning. In principle, also GaN NWs can be prepared using metallic seeds. Ni islands acting as collectors on bare sapphire substrates lead to the formation of GaN NWs in the VSS mechanism.[100,101] However, the use of a metallic particle as collector resulted in a high concentration of stacking faults in the obtained NWs.[38] Furthermore, some Ni might be actually incorporated into the GaN NWs.[38] These drawbacks caused catalyst-induced GaN NWs to be less interesting from a technological point of view and thus this growth approach has received much less attention than the spontaneous formation of GaN NWs.

Alternatively, GaN NWs can be formed on prepatterned masks, where the difference in nucleation behavior on the mask and in the holes is exploited to enforce the formation of NWs. Different groups have successfully implemented selective-area growth of GaN by MBE. Both Ti masks on GaN films as well as SiO_x masks on AlN buffer layers have enabled the fabrication of selective-area-grown well ordered GaN NW arrays.[34,102–106] Unquestioned, ordered SAG NWs are favorable for industrial applications. However, compared to some mask types, spontaneously formed GaN NWs still possess a higher structural quality, because SAG NWs often constitute coalesced aggregates within one hole. Owing the mask preparation process, accompanied by the often observed lateral overgrowth of the SAG NWs onto the mask, the minimum achievable diameter for SAG NWs is larger than for spontaneously formed NWs. In addition, the growth of spontaneously formed NWs allows the choice of a wide variety of substrates. Last but not least, mask fabrication process is also very cost- and time-intensive. Simultaneously, also the spontaneous formation of GaN NWs is yet far from being fully understood and optimized. Any improvement in the fabrication and analysis of spontaneously formed NWs will be also beneficial for SAG. Therefore, in this thesis, we will concentrate solely on the spontaneous formation of GaN NWs.

In order to summarize the reports on spontaneously formed GaN NWs, different aspects have to be addressed. These include the formation mechanisms leading to NW growth, the structural properties of single NWs, as well as their optical properties. Aiming to provide a comprehensive review, context will be favored to historical order. The majority of the results presented here were obtained on Si(111) which is the most common substrate. However, to high extent, they can be extrapolated to other substrates.

Nanowire nucleation and growth

Two main aspects are important for the spontaneous NW formation: (i) the nucleation mechanisms and (ii) the preferred uniaxial elongation. The ladder can be easily explained by diffusion induced growth, where a lower chemical potential at the top-facet leads to adatom diffusion along the NW sidewalls.[107] For rotating substrates, Ga and N usually impinge on the NW sidewalls with a relative time delay, while on the NW top facet they arrive simultaneously.[108] Theoretical calculations yielded that N, in contrast to Ga, does not diffuse along the M-plane NW sidewalls but rather forms molecular nitrogen and desorbs.[109]

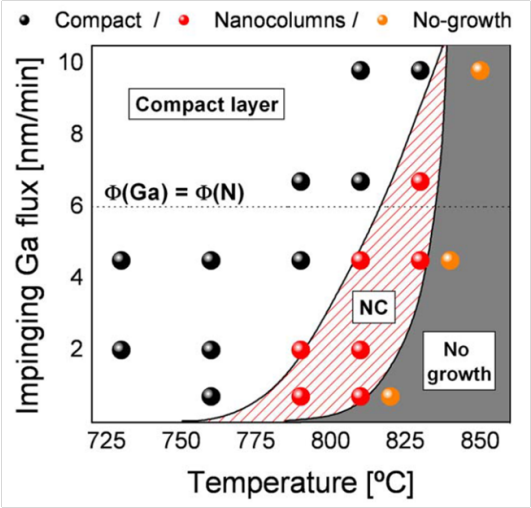

Figure 3.9: Experimental growth diagram for the spontaneous formation of NWs (here labeled nanocolumns) in MBE from Fernández-Garrido et al.[74]. Note that this diagram is only valid for the given N flux. The required substrate temperature is higher than what is used for planar layers. For too high III/V ratios, a compact layer is formed. For too high substrate temperatures, no growth is observed.

The nucleation mechanisms, on the other hand, seem to be more complex and are not yet fully understood. The nucleation of GaN NWs depends strongly on the growth parameters, i.e., the substrate temperature and the impinging fluxes. Prior to the onset of nucleation, an incubation period is observed where no NWs are formed yet. Consonni et al. reported an Arrhenius-like temperature dependence of the incubation time with a nucleation energy of (4.9 ± 0.1) eV, studying the influence of the growth parameters on the incubation time using RHEED.[55] They argued that during the incubation stage where no GaN signal is detectable in RHEED subcritical nuclei form and decompose. Once these subcritical nuclei transform to critical nuclei and eventually form NWs, they are detectable in RHEED and the growth proceeds from the incubation stage to the NW nucleation.[55]

Furthermore, Consonni et al. analyzed in detail the transition from nucleus to NW using transmission electron micrographs of NW samples where the growth was interrupted at different times during nucleation.[54] They observed the formation of spherical cap-shaped islands on a Si_xN_y amorphous interlayer. With time, the nuclei coarsen and increase in density. Above a critical diameter of 10 nm (and a height of 2 nm), they undergo a shape transition toward the NW morphology, driven by strain relief.[54] Another driving force toward the NW shape is suggested to be the anisotropy of surface energies.[110]

This formation of NWs by shape transition continues until eventually reaching very high densities, typically on the order of $10^9 - 10^{10}$ NWs/cm^2. Consonni et al. observed that the intensity of the GaN-related RHEED signal continuously increases with ongoing NW nucleation until saturating at some point.[55] The duration of the nucleation time, meaning the time difference from the shape transition of the first NW to that of the last NW, is again dependent on the growth conditions and may easily become as long as several hours.

After a spherical island experiences a shape transition, it may grow radially and axially. The final diameter of the NW was found to be determined by the ratio between the impinging Ga and N fluxes seeking a self-regulated equilibrium at the NW tip.[65] After the NW has nucleated, Ga impinging on the substrate can diffuse from the substrate

onto the NW and further to the NW tip. This surplus in available Ga may lead to Ga effectively exceeding the impinging N and resulting in radial in addition to axial growth. This radial growth simultaneously decreases the relative contribution of the Ga diffused to the top facet. Thus, a self-regulated equilibrium is obtained when the Ga, both directly impinging and diffusing to the top facet, reaches stoichiometry with the impinging N.[65] As a consequence, changing the Ga/N flux ratio during growth only allows to increase the NW diameter. When the Ga/N ratio is lowered, the axial growth rate is decreased but the diameter remains untouched.[65] The thinnest NWs observed by Consonni et al.[54] directly after shape transition already have diameters above 10 nms, the thinnest diameters reported for longer NWs were about 15 nms, while for dense ensembles, typically diameters above 30 nm are observed.[54,74,111,112]

As a consequence of this self-regulated equilibrium, the axial growth rate of the NWs is expected to be equal to the impinging N-flux, once this stoichiometry is achieved.[65] Only in the case where nucleation occurs very fast, this fast nucleation and the coalescence of adjacent NWs may lead to the fact that the NW diameter exceeds the equilibrium diameter. If the area coverage of the NW ensemble is very high, the relative fraction of Ga impinging on the NW sidewalls and diffusing to the tip is too low to reach stoichiometry. In this case, the axial growth rate remains Ga-limited.[113] Simultaneously, the self-regulated radius also explains the requirement of N-rich growth conditions. For high Ga/N ratios, a compact layer forms due to radial growth.[65]

GaN NWs spontaneously form on a variety of substrates, including Si(111), Si(100), amorphous SiO_x and Al_2O_3, AlN, Ti, Diamond, SiC, Graphene.[35–40,49,111,112] In addition to the N-rich growth conditions, two other prerequisites may be necessary to spontaneously form GaN NWs. These have not yet been fully agreed upon in literature, however.

The first requirement we want to address at this point is the polarity. GaN NWs in principle form in the wurzite crystal structure with growth proceeding along the [0001] axis.[65,114] The cross section of single NWs usually exhibit the shape of a distorted hexagon where the sidewalls are constituted by M-plane facets.[61,115–117] The distortion is believed to originate from shadowing effects due to the irregular next neighbor distance in spontaneously formed NWs.[56] There has been quite some dispute in literature, whether spontaneously formed GaN NWs on Si grow in Ga or N polarity.[60,114,118,119] Experiments by Fernández-Garrido et al., where NWs were grown on AlN buffer layer on C and Si-face SiC simultaneously addressed the influence of the substrate polarity and defect nucleation.[120] As the buffer layer is known to adopt the polarity of the SiC substrate,[121–123] the only difference between both samples was the polarity. The polarity of the NWs was assessed on a microscopic scale using convergent beam electron diffraction (CBED) and electron energy-loss spectroscopy (EELS). On N-polar AlN, a dense ensemble of N-polar NWs formed. On Al-polar AlN, the formation of a faceted layer was observed with scattered single NWs in between. These scattered NWs were found to be N-polar as well, probably located on inversion domains induced by Si segregation.[120] In addition, the N-polarity of NWs grown directly on Si(111) was also confirmed on a macroscopic scale using CBED, resonant XRD,[114] low-energy electron diffraction (LEED), x-ray photoelectron diffraction (XPD) and KOH etching.[124] While the matter is still under discussion in literature, most experimental results indicate that that spontaneously formed NWs on Si(111) grow N-polar by nature.[114,119,120,124]

The second potential requirement for the formation of NWs is the presence of strain or an amorphous layer. To our knowledge, there have been no reports on the spontaneous homoepitaxial formation of GaN NWs on GaN yet. However, the question whether strain

is an actually required condition has not yet been conclusively discussed in literature.

Furthermore, even once NW nucleation has completed, axial growth does not proceed as uniform as one would expect from planar layers. As a consequence of the different delay times for NW formation of the individual NWs, they initially exhibit a wide distribution in length. With growth time, however, the NWs have been observed to assimilate in length. This phenomenon was explained by Sabelfeld et al. with the help of collective effects.[125] When considering the Ga desorption and adsorption taking place on the NW sidewalls and the thereby invoked exchange of Ga adatoms between adjacent NWs, shorter NWs result to collect more Ga than longer ones. This effect allows the shorter NWs to catch up in height and leads to an overall height equilibration in the NW ensemble.[125] Solely NWs which do not collect any active N due to shadowing cannot compete and stop growing.

Summarizing the spontaneous formation of NWs, dense ensembles of N-polar NWs are obtained on substrates inducing N-polarity as well as on nonpolar substrates like Si(111). To induce the spontaneous formation of GaN NWs, characteristic growth conditions are required. Fig. 3.9 depicts the growth diagram for GaN NWs on Si(111) in MBE for a given N flux of $\Phi_N = 6$ nm/min. For too high effective Ga/N ratios, a compact layer forms. For too high substrate temperatures, no NW nucleation is observed within the given growth time. The basic principle of nucleation is believed to be comparable on all substrates. This principle includes the shape transformation from cap-shaped islands to NWs followed by radial and axial growth on the single NW scale and continuous nucleation until eventually reaching very high densities on the ensemble scale. Solely the nucleation barrier is expected to depend on the substrate type leading to different nucleation rates at comparable temperatures.[104,105]

Nanowire properties

Single GaN nanowires have been found to be usually free of extended defects. Dislocations are confined at the interface[33] or bend toward the free NW sidewalls.[34,126] However, as it has been addressed already, the coalescence of adjacent NWs may lead to the formation of dislocated tilt/twist boundaries.[57,75] The impact of NW coalescence hereby strongly depends on the mutual misorientation of the NWs and thus on the epitaxial alignment to the chosen substrate. Small values of tilt and twist are more likely to be accommodated elastically.[56]

Owing the high structural perfection of GaN NWs, the optical properties of GaN NWs are expected to be comparable to state-of-the-art GaN layers.[127] The peak position of the dominating (D^0, X_A) transition indicates that the NWs are generally free of homogeneous strain. As discussed above, NW coalescence may induce inhomogeneous strain which results in a broadening of the linewidth of the excitonic transitions.[57,69,76] In addition, the bound exciton transitions in NWs may also broaden due to the energy dispersion of these states resulting from their varying distances to the NW sidewall surfaces.[43,44] Furthermore, short decay times are observed experimentally for bound excitons in GaN NWs. TR-PL measurements typically yield decay times below 200 ps[44,77,87] compared to about 1 ns obtained in bulk GaN.[128,129] Recently, both the surface and coalescence boundaries have been excluded as the main origins for nonradiative recombination by Hauswald et al. (compare Chapter 5). Alternatively, they showed that bound and free excitons couple in GaN NWs. Thus, the presence of point defects is discussed as the main origin for the nonradiative recombination.[87] Owing to the exciton coupling of bound and free excitons, point defect densities as low as 10^{15} cm^{-3} may be sufficient to introduce an effective nonradiative recombination channel.[87]

Summarizing, the synthesis of GaN in the form of NWs instead of films not only enables the growth of single-crystalline GaN on dissimilar substrates[35–41] but also the use of significantly higher substrate temperatures in MBE compared to planar layers.[35,49,50,74] However, at temperatures exceeding 850°C, no spontaneous formation of NWs has been observed so far.[50,74] In addition, spontaneously formed NWs suffer from the fact that there is essentially little control over the ensemble morphology. Owing to the high number density, NWs ensembles usually exhibit significant degrees of coalescence.[56,73] Their observed optical properties do not yet match the theoretical expectations.[43,87]

3.3.2. The three stages of GaN nanowire growth – in situ control by QMS and RHEED

In the following section, the temporal evolution of the Ga incorporation during NW growth is analyzed. This section is to a large part based on a recent publication by Fernández-Garrido et al.[50] The results presented therein were obtained at the Paul-Drude-Institut in the last few years and served as a starting point for the main investigations presented in this thesis.

As discussed in Section 3.2.1, line-of-sight QMS enables the in situ monitoring of the desorbing Ga flux Φ_{des} during growth. The Ga incorporation rate is then determined through $\Phi_{\mathrm{inc}} = \Phi_{\mathrm{Ga}} - \Phi_{\mathrm{des}}$. Figure 3.10 depicts the temporal evolution of the Ga incorporation rate for the reference sample, derived from the raw data presented in Figure 3.3 as described above. In stage I, during the incubation period, no Ga is incorporated. The onset of the NW nucleation stage II was indicated by the appearance of the first GaN-related RHEED spots after 25 min. It is accompanied by a rise in the Ga incorporation rate. The change in incorporation rate is maximal after about 60 min. After around 90 min, the Ga incorporation rate continues to increase, but at a different pace. At this point, the last growth stage, stage III, starts. After 3 h of growth, the Ga incorporation eventually reaches a steady-state level of 2.6 nm/min in equivalent planar growth rate units.

In Ref. [50], we correlated the evolution of the Ga incorporation to the actual morphology of the NW ensemble by interrupting the growth at the different times. We found that the first, steep increase in the Ga incorporation rate centered around 60 min is correlated to the nucleation of NWs. At this time, the cap-shaped islands formed, undergo a shape transformation toward the final NW-like morphology and start to grow radially, until reaching their equilibrium diameter, and axially. The residual increase in Φ_{inc} observed in stage III is attributed to collective effects causing an equilibration in the height distribution.[125] Thereby, all NWs are enabled to maximize their axial growth rate which results in an increase in the Ga incorporation rate. In the early stages of nucleation, a significant amount of Ga atoms impinge on the substrate or on the NW sidewalls at distances to the NW tip greater than the diffusion length. Consequently, these Ga atoms desorb and cannot contribute to growth. As the NW density increases, desorbing Ga atoms are more likely to be readsorbed on adjacent NWs. In addition, due to shadowing, the impinging Ga is usually adsorbed closer to the NW tips and more likely to contribute to growth. Consequently, Φ_{inc} must increase until the NW ensemble becomes homogeneous in height.[125]

We found that this temporal evolution of the Ga incorporation rate can be described by the following empirically motivated equation:

$$\Phi_{\mathrm{inc}} = \frac{A_1}{1 + \exp\left(-\dfrac{t - t_1}{\tau_1}\right)} + \frac{A_2}{1 + \exp\left(-\dfrac{t - t_2}{\tau_2}\right)} \tag{3.5}$$

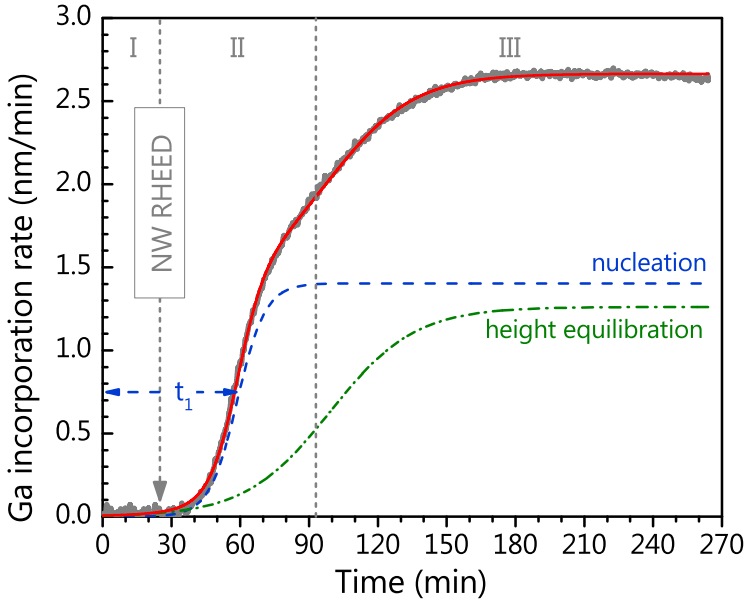

Figure 3.10: Temporal evolution of the Ga incorporation rate per unit area during the growth of the reference sample. The end of the incubation stage I is labeled by the observation of the first NW RHEED signal. The nucleation stage II is determined by the average NW formation time labeled t_1. In stage III, the NWs equalize in height and elongate.

This equation consists of the sum of two logistic functions. As can be seen in Figure 3.10, it yields an excellent fit to the experimental data. The two logistic functions allow to separate the two contributions of NW nucleation and height equilibration. Their individual temporal evolutions match the experimental observations of the area coverage and height equilibration. Therefore, t_1 represents the average delay time for NW formation, while $1/\tau_1$ is a rate constant describing the NW formation rate, and A_1 is a constant. Accordingly, t_2, $1/\tau_2$ and A_2 describe the time evolution of the height equilibration. In Figure 3.10, the contributions of nucleation and height equilibration are given by the blue dashed and the green dash-dotted lines, respectively. The average delay time for NW formation t_1 was found to be 60 min, for the NW formation rate a value of $\tau_1 = 6.1$ min was obtained.

The assessment of the average delay time for NW formation through t_1 allows us to estimate the average axial growth rate of the NWs during the elongation stage. For the reference sample, 2.2 µm long NWs we obtained in a total growth time of 264 min. Taking into account the average delay time for NW formation $t_1 = 60$ min, an axial growth rate of 10.7 ± 0.5 nm/min is measured. As the impinging N-flux was $\Phi_N = 11.0 \pm 0.5$ nm/min, we obtain that in the case of the reference sample the axial growth rate of the NWs approaches the N flux and is thus is N-limited.

Whereas previous growth models successfully characterized the specific stages of NW growth[54,65,73,108,111,113,125,130,131], equation 3.5 provides an empirical but comprehensive description of the entire NW growth process. Therefore, it enables a systemic investigation on how the spontaneous formation and growth of GaN NWs depend on the growth parameters, namely the substrate temperature, Φ_{Ga}, and Φ_N.

For a series of samples, where the substrate temperature was systematically varied between 775°C and 835°C, an Arrhenius-type temperature dependence was found for the

average delay time for NW formation t_1

$$t_1 = C_1 \exp(-E_N/k_B T), \tag{3.6}$$

where E_N represents an activation energy and C_1 is a constant. Analogously, also the NW formation rate τ_1 follows an Arrhenius-type temperature dependence. The fits of the experimental data yielded activation energies of (6.4 ± 0.1) eV for the delay time t_1 and (3.1 ± 0.1) eV for the NW formation rate τ_1. These values do not agree with those reported by Consonni et al., who determined an activation energy of (4.9 ± 0.1) eV using RHEED.[55] This is not a contradiction, however, as both, RHEED and QMS, investigate different processes. Using RHEED, the duration of the incubation time is determined, in other words the duration of stage I, the end of which is determined by the nucleation of the first NWs. In QMS, the NW formation rate τ_1 is the key parameter that effectively determines the duration of the NW nucleation stage, stage II. The average delay time for NW formation, on the other hand, describes a superposition of both processes. In fact, these two processes actually seem to be independent of each other, as will be reported in Chapter 4.2. Nevertheless, for advancements in NW growth techniques, the temperature dependence of average delay time for NW formation is the key factor, as it describes the experimentally decisive parameter: after which time period NWs essentially nucleate.

Simultaneously, the dependence of these key parameters on the Ga flux was determined using a series of samples where the substrate temperature was kept constant at 805°C and the Ga flux varied between 3 and 22 nm/min. For the average nucleation time, a dependence according to

$$t_1 = \frac{C_2}{\Phi_{Ga}^{3/2}} \tag{3.7}$$

was found, where C_2 is again a constant. This result is compares well with the dependence of duration of the incubation stage on the Ga flux, reported in Ref. [55]. The power law was explained within the framework of standard island nucleation theory and the 3/2 exponent was related to the critical size of the stable GaN nuclei.[55] For the NW formation rate τ_1 a similar dependence was found, with the difference that the exponent of the Ga flux was 1 instead of 3/2.

Determining the influence of the impinging N flux is experimentally more time-consuming. However, when deceasing the impinging flux from (10.5 ± 0.5) nm/min to (4.7 ± 0.5) nm/min, we observed a pronounced delay in NW formation. Whereas for the sample using the high N flux, a dense and homogeneous NW ensemble forms in a growth time of 3 h, in the same time only sparse and short NWs form for the low N flux, evidencing that for the latter sample the growth was interrupted at the very early stage of NW nucleation.

Combining the results obtained in equations 3.6 and 3.7, we can deduce a quantitative dependence of the average NW formation time t_1 on the growth parameters:

$$t_1 = C_N \frac{\exp(-E_N/k_B T)}{\Phi_{Ga}^{3/2}}. \tag{3.8}$$

As we were not able to quantify the influence of the N flux, its impact is given by the constant factor C_N and has to be determined experimentally for each Φ_N value.

Figure 3.11 depicts the value of t_1 obtained from equation 3.8 in a contour plot with a logarithmic color scale over a wide range of parameters. Thanks to the quantitative de-

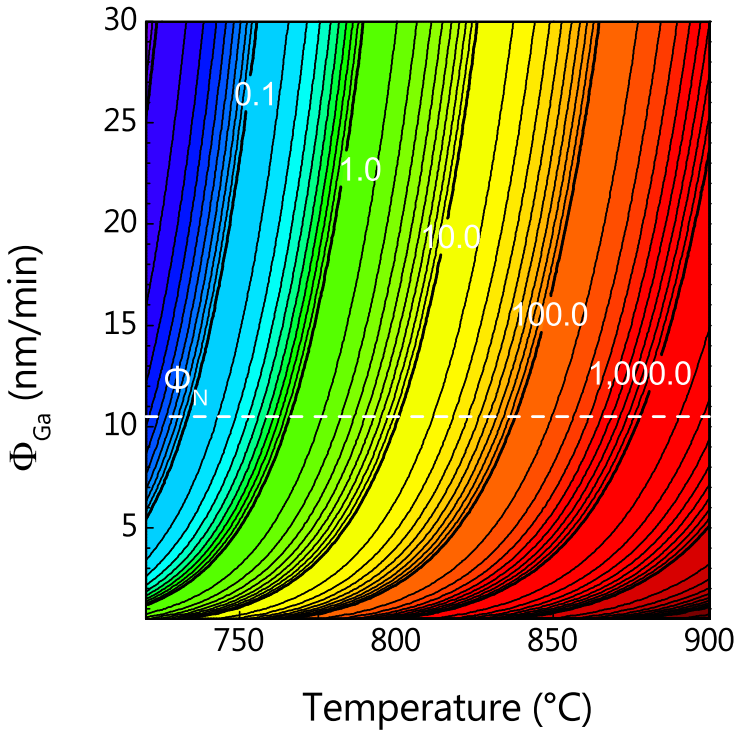

Figure 3.11: Contour plot depicting average delay time for NW formation in min as a function of the growth parameters.[50]

scription of t_1, we are able to predict the influence of substrate temperature and Ga flux on the average NW nucleation time for growth conditions that have not been experimentally explored before. In fact, Figure 3.11 can also be understood as a growth diagram, schematically comparable to the experimentally determined growth diagram given in Figure 3.9 taken from Ref. [74]. The similarity becomes more clear, when taking into account the following two considerations: (i) For very low values of t_1, nucleation takes place very fast. However, the combination of low substrate temperature and high Ga flux typically results in NWs ensembles that either exhibit high degrees of coalescence or actually form compact layers.[74] On the other hand, t_1 quickly becomes as long as several tens of hours, when using very high substrate temperatures or very low Ga fluxes. For these conditions, NW growth quickly becomes impractical, experimentally no growth is observed within reasonable growth times. We must stress that Figure 3.11 is only quantitatively valid for an impinging N flux of $\Phi_N = (10.5 \pm 0.5)$ nm/min. A higher active N flux would to reduce t_1 and shift the entire growth diagram toward lower Ga fluxes and higher substrate temperatures. For our concerns, the here derived growth diagram provides an excellent starting point to explain the new growth approaches that we envisioned and developed in this thesis.

3.3.3. The limitations of the spontaneous formation of GaN NWs in PA-MBE

On the previous pages, we have extensively described the spontaneous formation of GaN NWs and summarized the important publications contributing to the current understand-

ing of spontaneous NW formation and growth in MBE. Nevertheless, as for any other self-organized growth process, the degree of control on the properties of GaN NW ensembles is rather limited. Unless the growth is stopped before the NW nucleation stage is over, dense ensembles form. Thus for ensembles of long NWs, always a high number density on the order of 10^9 to 10^{10} NWs/cm^2 are obtained,[73,74,111] independently of the growth conditions used. Owing to this high number density, NW ensembles generally exhibit significant degrees of coalescence. As usually more than half of the total NW volume is exposed to coalescence boundaries,[56] the resulting structural and optical properties of the NW ensemble may be compromised quickly.[57,75,76]

The choice of impinging fluxes as well as substrate temperature influences both the average delay time for NW formation as described above[50] and the average diameter of NWs via the effective III/V ratio on the NW tip.[65] The average delay time for NW formation quickly imposes a temperature limit. The maximum reported growth temperatures for spontaneously formed GaN NWs are close to 840°C.[50,74] So far, no growth was observed at higher substrate temperatures. However, as it will be explained later, higher growth temperatures are highly desirable. The optimal growth temperature for GaN in MOCVD and HVPE is rather around 1000°C[91–93] and the optical properties of GaN NWs are expected to further improve when higher substrate temperatures are used.[38,83]

The average diameter of NWs is determined in a self-regulated process by the effective III/V ratio during NW growth.[65] This means that growth conditions favoring fast NW nucleation inevitably result in comparably high NW diameters. Long NW ensembles usually exhibit diameters of 40 nm and higher. But even short NWs, directly after their shape transformation from cap-shaped islands to the NW morphology exhibit diameters of not less than 10 nm.[54,74,111,112]. For some interesting applications, however, a lower dimensionality is desirable. For instance, as the Bohr radius in GaN is about 3 nm,[132] much thinner wires are required to actually obtain quantum confinement in GaN NWs.

In the following chapters, we will point-by-point address these limitations of the spontaneous formation of GaN NWs. We will attempt to find solutions for gaining more control over the morphology and properties of the resulting NW ensembles. In cases where we succeed, we will investigate how the newly developed growth approaches affect the structural and optical properties of the resulting GaN NW ensembles.

In Chapter 4, we will address the limited control on NW number density and coalescence degree. By separating the nucleation and elongation stages of NW growth using a two-step process, we will attempt to gain control over both properties. Although the achieved degree of control is limited, we gain important knowledge on the mechanisms governing NW nucleation. Furthermore, we will develop an understanding of the effects of a two-step growth process that will be beneficial for all subsequent chapters.

In Chapter 5, we will overcome the temperature limitations of the spontaneous formation of GaN NWs. Using three unconventional growth approaches, we will report on NW ensembles grown at temperatures up to 905°C. The mechanisms of these growth approaches can easily followed considering again the growth diagram presented in Figure 3.11. The first approach consists in leaving the common regime of nominally N-rich growth conditions. Instead, we use nominally Ga-rich growth conditions to compensate for the high desorption rate of Ga adatoms at elevated substrate temperatures. In the second approach, we use again a two-step growth procedure in which an initial low-temperature step favoring rapid nucleation is followed by a high-temperature elongation stage. In the third approach, we make use of an additional parameter that influences NW nucleation which we have not discussed in extent before, the choice of substrate. By introducing an

AlN buffer layer, we enable faster nucleation at higher substrate temperatures. We will investigate the phenomenon of Si melt-back etching that comes along with the growth of GaN NWs on Si at high temperatures. Furthermore, we will in detail investigate the GaN NW ensembles prepared at these high substrate temperatures.

Finally, in Chapter 6 we will devise a method to fabricate GaN NWs of unprecedented low diameters. Using post growth decomposition of GaN NWs, we will report on the controlled diameter reduction and the properties of the resulting ultrathin GaN NWs.

4. Improved growth control using a two-step method

In MBE, the diameter of spontaneously formed GaN NWs is regulated by the Ga/N ratio[37,65] while the NW number density is supposed to be determined by the diffusion length of Ga adatoms along the substrate.[67] For low enough Ga/N ratios, the diameter of single NWs can be as small as $10 - 15$ nm.[54,74,111,112] However, in most cases, the effective average diameter becomes larger due to the coalescence of adjacent NWs. This undesired phenomenon, presumably caused by NW mutual misorientation as well as NW radial growth,[56] is favored by the high nucleation density of GaN NWs (typically, in the range of $10^9 - 10^{10}$ cm^{-2}).[73,74,111] Unfortunately, NW coalescence does not only result in a poor degree of control over NW morphology but also introduces extended defects as well as inhomogeneous strain.[57,69,70,75,76] Therefore, in order to take advantage of spontaneously formed NWs for the fabrication of GaN-based devices on dissimilar substrates, it is highly desirable to develop growth approaches designed to gain control over the nucleation and growth of GaN NWs to suppress or minimize NW coalescence.

Carnevale et al. proposed a two-step growth method to separate the nucleation and growth processes.[133] They showed that, by increasing the substrate temperature during the nucleation stage, it is possible to disentangle and vary the number density, the height, and the length of spontaneously formed GaN NWs. However, even though they were able to vary the NW number density in a wide range, the resulting NW ensembles were rather short (< 400 nm) and very inhomogeneous in height.

In this chapter, we systematically investigate the impact of modifying the growth conditions at different stages during the spontaneous formation of homogeneous GaN NW ensembles on Si. In Section 4.1, we analyze the impact of increasing the substrate temperature at different times during the nucleation of GaN NWs. Although, when growing long and homogeneous NW ensembles, we were not able to reduce significantly the NW number density, we gained control over area coverage, average NW diameter and coalescence degree.

In Section 4.2, we investigate the influence of the growth conditions employed during the incubation stage[50,55,111] that precedes NW nucleation. The results demonstrate that the properties of the NW ensemble do not depend on the growth conditions used during the incubation stage. Therefore, a two-step growth approach, where more favorable growth conditions for NW nucleation are employed during the incubation stage, can be used to reduce the total growth time without affecting the properties of the final NW ensemble.

In Section 4.3, we explore the limits of a two-step growth approach. We thus gain insight into the mechanisms governing the spontaneous formation of GaN NWs and compare our observations to the results reported by Carnevale et al.[133]

Experimentally, the two-step growth approach paves the way for growing GaN NWs under more extreme growth conditions (lower Ga/N ratios and higher substrate temperatures) which typically results in smaller NW diameters, lower degrees of coalescence, and improved optical properties.[37,38,74,83,86,134] This growth procedure will turn out to be an

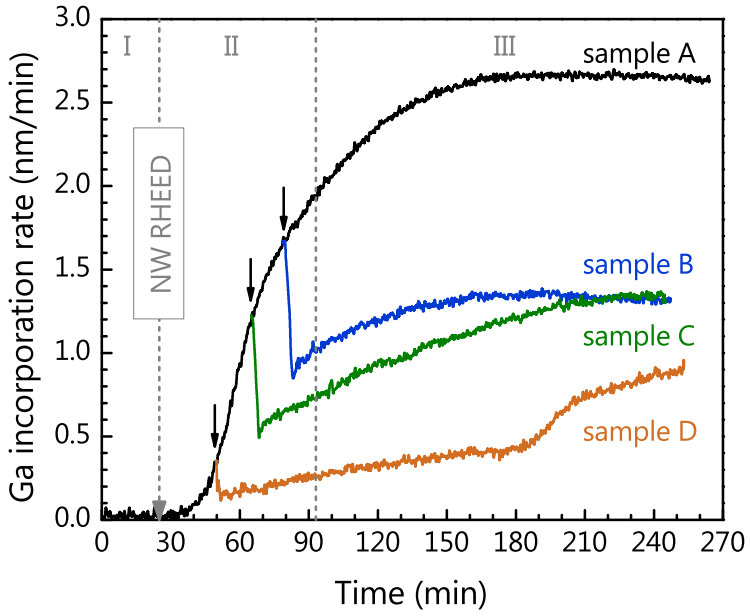

Figure 4.1: Temporal evolution of the Ga incorporation rate per unit area during the NW growth of samples A to D obtained from quadrupole mass spectrometry. The typical double-logistic behavior is observed for sample A, prepared using constant growth conditions. For samples B to D, the substrate temperature was increased by 30°C at the times by the arrows.

essential contribution to the results obtained in the subsequent chapters.

Some of the results presented in this Chapter have been published in Ref. [135].

4.1. Control of NW morphology and distribution

Here, we investigate to which extent the morphology and distribution of GaN NWs can be controlled using a two-step growth process where the growth conditions are modified during the nucleation stage.

In view of the fact that every NW experiences a different delay time before it is formed, which strongly depends on the specific growth parameters,[50,55] we expect to gain control over both NW number density and coalescence degree by modifying the substrate temperature at the nucleation stage (stage II in Fig. 3.10), as suggested by Carnevale et al. [133] Because the average delay time for NW formation increases exponentially with substrate temperature,[50,55] raising the temperature before NW nucleation is completed could even-

Table 4.1: Summary of the growth conditions used for samples A–D. The impinging fluxes were kept constant at $\Phi_{Ga} = (5.5 \pm 0.5)$ nm/min and $\Phi_N = (11.0 \pm 0.5)$ nm/min.

		sample A	sample B	sample C	sample D
step 1	substrate temperature (°C)	815	815	815	815
	growth time (min)	270	80	65	50
step 2	substrate temperature (°C)	-	845	845	845
	growth time (min)	-	190	205	220

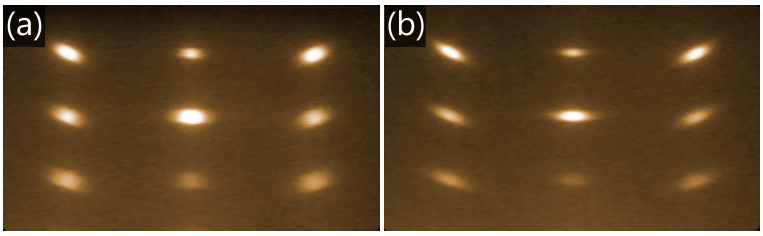

Figure 4.2: RHEED patterns along the [11$\bar{2}$0] azimuth of (a) sample B and (b) sample C at the end of the first growth step.

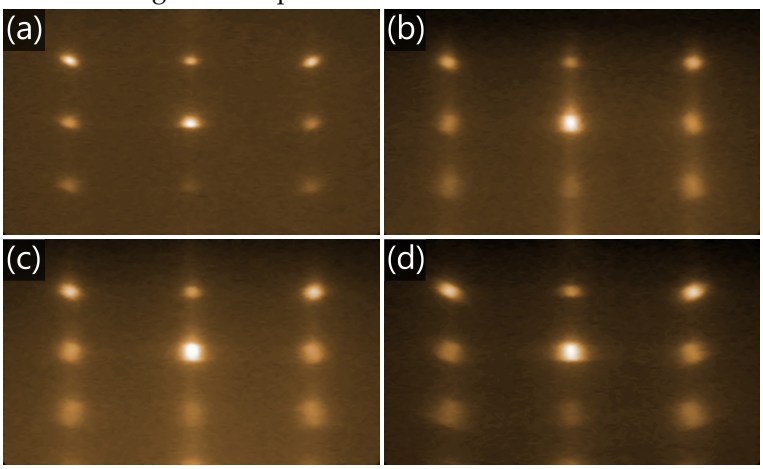

Figure 4.3: (a)–(d) RHEED patterns along the [11$\bar{2}$0] azimuth of samples A to D, respectively, at the end of the growth experiments.

tually suppress further nucleation and thus decrease the final NW number density and coalescence degree. To investigate this possibility, we prepared a series of samples where the substrate temperature was increased by 30°C at different times during the nucleation stage (samples B–D). For all samples, we used the same impinging fluxes, initial substrate temperature, and total growth time as for the reference sample which was prepared in a conventional fashion, namely, keeping constant all growth parameters throughout the entire process. The detailed analysis of the Ga incorporation rate of the reference sample, referred to as sample A in this chapter, was already performed in Section 3.3.2 (cf. Figure 3.10). Fig. 4.1 shows the temporal evolution of the Ga incorporation rate per unit area of samples A–D. For samples B–D, the substrate temperature was first kept at 815°C. After 80, 65, and 50 min, respectively, the substrate temperature was increased to 845°C at a rate of 10°C/min keeping the Ga and N shutters open during the entire process. Therefore, before increasing the temperature, for sample B the nucleation was close to the end, for sample C well advanced, and for sample D at the early times (The growth conditions of samples A–D are summarized in Table 4.1). For those samples, the increase in growth temperature apparently leads to a decreased Ga incorporation compared to sample A. Furthermore, the change in slope suggests, that the rate at which the NW nucleation and the subsequent growth stages follow is also influenced. The sudden increase in the Ga incorporation after 190 min for sample D is believed to be a measurement artifact.

Figures 4.2(a) and (b) depict the RHEED patterns along the [11$\bar{2}$0] azimuth at the end of the first growth step, for samples B and C, respectively. As both samples are still at the early stages of growth, their RHEED patterns yet exhibit fragmented ring segments originating from the tilt distribution of the NW ensemble. The RHEED pattern of sample B,

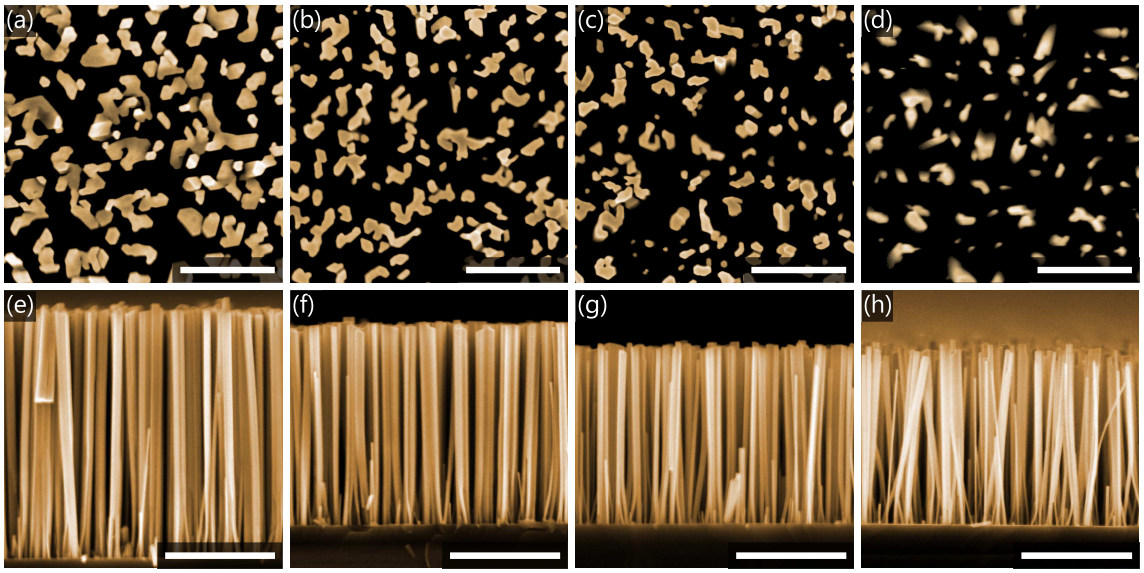

Figure 4.4: (a)–(d) Plan-view and (e)–(h) cross-section scanning electron micrographs of samples A–D, respectively. The scale bars correspond to 500 nm for plan-view and 1 µm for cross-sectional micrographs. SEM measurements carried out by Anne-Kathrin Blum.

however, is already much less ring-like than that of sample C, pointing toward a reduction in the average tilt due to the coalescence of NWs already occurring at the early stage of growth.

Figures 4.3(a) to (d) depict the RHEED patterns along the [11$\bar{2}$0] azimuth at the end of the second growth step, for samples A to D, respectively. The influence of the two-step growth approach can already be anticipated in situ from the comparison of the RHEED patterns. The earlier during the incubation stage the temperature is raised, the broader are the resulting NW spots. Thus the tilt distribution in the NW ensemble is increasing from sample A to sample D, which means that the coalescence degree is accordingly reduced. However, a more quantitative analysis of the impact of the two-step growth can be obtained from the ex-situ analysis of the NW top facets recorded by SEM.

Figures 4.4 (a)–(d) show plan-view scanning electron micrographs of samples A–D, respectively. The introduction of a two-step growth procedure leads to a clear reduction in the area fraction covered by GaN NWs. Also, the earlier during nucleation the substrate temperature is raised, the stronger is the influence on the final NW ensemble. Figures 4.4 (e)–(h) show the corresponding cross-sectional scanning electron micrographs. The NWs of sample A are about 2.2 µm long. When taking into account the average delay time for NW formation (60 min), we find that the axial growth rate is approximately 10.5 nm/min. This value is close to the impinging active N-flux ($\Phi_N = 11.0 \pm 0.5$ nm/min), in good agreement with the experiments reported in Refs. [35, 50, 65, 136–140]. In contrast, the NWs of samples B–D are not that long. Despite the identical growth times, the average NW length for samples B–D is only $1.6 - 1.7$ µm. The reduction in the axial growth rate, which becomes Ga-limited, is due to the thermal enhancement of Ga desorption during the second step of the growth.[52]

Assuming a N-limited growth rate of $r_1 = 11.0$ nm/min in the first step, we can estimate the average NW length at the end of the first growth step. Thus, we can calculate the axial growth rate r_2 for the second step, shown in Figure 4.5. For samples B, C, and D we obtain

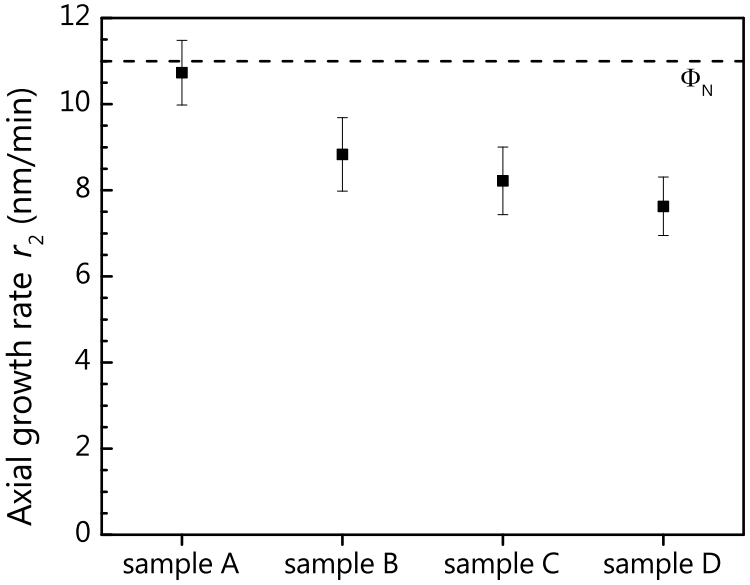

Figure 4.5: Axial growth rate during the elongation stage for samples A to D. While the growth rate of sample A is N-limited, the ones of samples B to D are Ga-limited due to the increased desorption of Ga at higher temperature. In addition, an additional decrease in growth rate from sample B to D is observed.

an axial growth rate in the second step of $r_2 = 8.8$ nm/min, 8.2 nm/min and 7.6 nm/min, respectively. This drop in axial growth rate indicates that a lower growth rate due to the higher Ga desorption may not solely be a temperature effect but might also be favored by the increase in the mean NW distance. Thus, the probability of Ga atoms desorbing from the NW sidewalls to escape increases. In contrast, their chance to being readsorbed on adjacent NWs where, again, they could contribute to growth decreases. If the average diameter after the end of the first growth step is already larger than the self-regulated equilibrium radius of the second growth step would be, the growth becomes Ga-limited and the the axial growth rate r_2 changes accordingly.

Figure 4.6 depicts the circularity histograms derived from the analysis of the cross-sectional shapes of the GaN NWs of samples A–D. The histogram of the reference sample

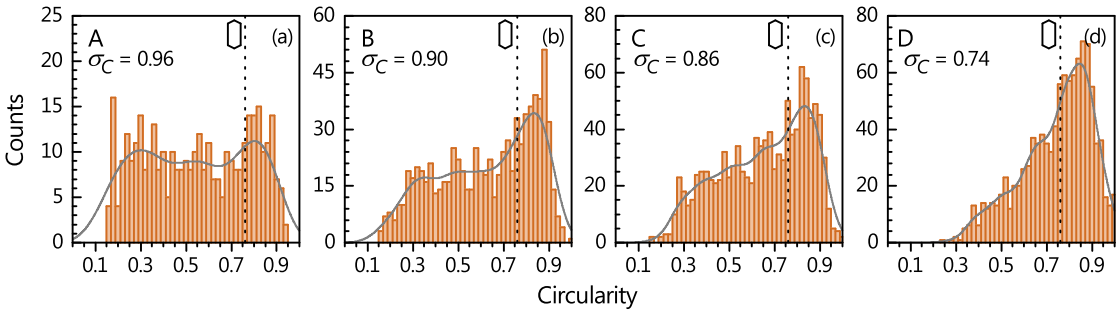

Figure 4.6: Circularity histograms of the cross-sectional shapes of NWs from samples A–D. The solid lines show the kernel density estimation of the respective histogram, the dashed lines indicate the threshold value ζ_A. The coalescence degrees σ_C are derived from eq. 3.2.

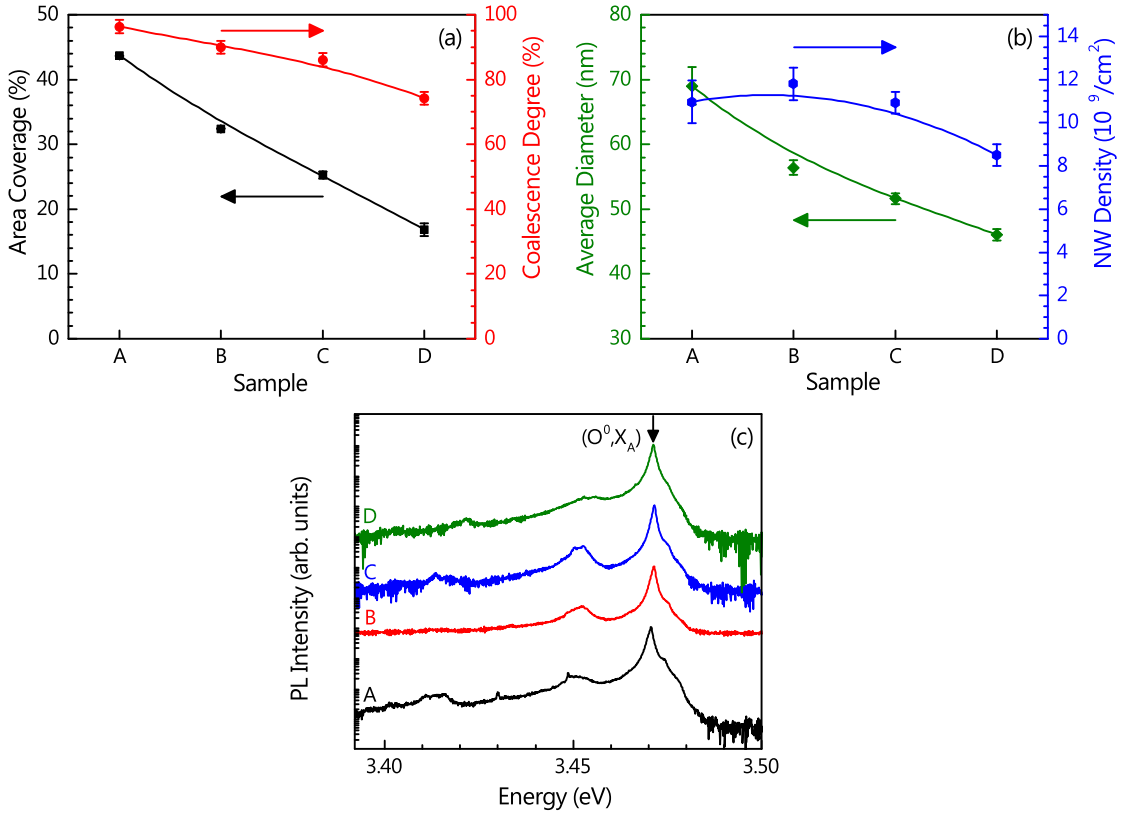

Figure 4.7: Area coverage, coalescence degree, average uncoalesced nanowire diameter, and total nanowire number density of samples A–D as determined from the statistical analysis of plan-view scanning electron micrographs. The lines are provided as a guide-to-the-eye. (c) Normalized photoluminescence spectra at 10 K for samples A—D. The spectra have been shifted vertically. PL measurements carried out by Pierre Corfdir.

[Fig. 4.6(a)] is rather broad, reflecting a wide variety of cross-sectional shapes as result of NW coalescence. Interestingly, the variation in the substrate temperature during the nucleation stage has a strong impact on the distribution of cross-sectional shapes. As shown in Figs. 4.6(b)–(d), the earlier the temperature is raised during the nucleation stage, the narrower is the circularity histogram.

Figure 4.7(a) shows for samples A–D the coalescence degrees derived from the circularity histograms as well as the area fraction covered by GaN NWs. The coalescence degree steadily decreases from 96 (reference sample) to 74% (sample D) when decreasing the time at which the substrate temperature is increased. The figure also evidences a decreases in the area fraction from 44 to 17%. In principle, the reduction of both the coalescence degree and the area fraction can be caused by the suppression of further nucleation and/or a decrease in radial growth during the second growth step.

Next, we extract the average diameter of uncoalesced NWs and the total NW number density. Figure 4.7(b) presents the values of these parameters for samples A–D. The average NW diameter steadily decreases from 70 to 45 nm from sample A to D. Regarding the total NW number density, the effect of modifying the substrate temperature during growth is not so clear. Increasing the temperature during the second half of the nucleation stage does not seem to influence the total NW number density which remains almost

constant ($\approx$ 1.1×10^{10} cm^{-2}). Only when the temperature is increased at the beginning of the nucleation stage, we observe a clear reduction in this parameter. This is the case of sample D which exhibits a total NW number density of 8.5×10^{9} cm^{-2}. Therefore, we conclude that the continuous decrease in the coalescence degree observed in Fig. 4.7(a) is mainly caused by a reduction in radial growth during the second step of the growth. This effect is the result of a decrease in the effective Ga/N ratio due to the enhancement of Ga desorption.

The high coalescence degree of sample D despite exhibiting a low total NW number density as well as a small average NW diameter is surprising. A close inspection of the scanning electron micrograph shown in Fig. 4.4(d) reveals that a significant number of NWs is bent. In addition, the distance between coalesced aggregates is much larger than the average NW diameter [see Fig. 4.4(h)]. These findings suggest that NW coalescence is not only due to NW mutual misorientation and NW radial growth but also induced by electrostatic attraction during growth.[56,141] The latter effect is most likely caused by the exposure of the NW ensemble to electrons originating from the N plasma source or the RHEED measurements. Electrostatic attraction between adjacent NWs has already been reported and systematically investigated in Si NW.[141] This phenomenon is expected to be more pronounced for thin and long NWs, as those of sample D. The intrinsic coalescence degree of sample D is therefore expected to be below the measured 74%.

Figure 4.7(c) shows normalized photoluminescence spectra at 10 K for samples A—D. The spectra (and intensities) of all samples are comparable despite the reduction in area coverage [Fig. 4.7(a)]. For all samples, the spectra are dominated by the recombination of A excitons bound to neutral oxygen [(O^0, X_A)] which shows a full width at half maximum of 1.1 ± 0.1 meV. These findings indicate that the given set of growth conditions used affect neither the inhomogeneous strain in the nanowire, nor the density of nonradiative recombination centers.

The results of these experiments demonstrate that, independent of the impinging fluxes, it is possible to obtain a certain degree of control over the morphology and distribution of GaN NWs by increasing the substrate temperature during the nucleation stage. This growth approach is found to be indeed an efficient method to decrease the average NW diameter as well as the area coverage. However, it seems that reduced NW diameters make the NWs more susceptible to electric attraction, leading to NW bending and non-intrinsic NW coalescence. Therefore, despite the reduction in NW diameter, the presented NW ensembles still suffer from a non-negligible degree of coalescence. We anticipate that additional measures aimed to prevent electrostatic attraction of NWs,[142] such as negatively biasing the substrate to deflect electrons originating from the N plasma, may enable a further reduction of the NW coalescence. The total NW number density, however, cannot be significantly decreased when growing long and homogeneous NW ensembles. This fact indicates that during the second step of the growth further nucleation is not completely suppressed. Therefore, despite the reduction in NW diameter, the NW ensembles still suffer from a non-negligible degree of coalescence. Our results are in striking contrast with those obtained by Carnevale et al., namely, a high degree of control over NW density by using a similar two-step growth approach.[133] The underlying reason for this discrepancy could be the much shorter growth times used by Carnevale et al. (< 90 min). The shorter times resulted not only in a lower density but also in much shorter and inhomogeneous NW ensembles. These apparently contradictory results can be reconciled by assuming that despite the presumable unfavorable nucleation conditions the NW number density increases slowly but steadily during the second step of the growth

until an homogeneous NW ensemble (as those shown in Fig.4.4) is formed due to the onset of collective effects.[125] A more detailed comparison of our growth experiments to those reported by Carnevale et al. will be given in Section 4.3.

4.2. Control over the incubation time

At elevated temperatures, a long incubation time hinders direct growth within reasonable growth times.[50] Here, we investigate whether the total growth time can be reduced, without modifying the morphological and optical properties of the NW ensemble, by using a two-step growth approach.

To this end, we prepared a second reference NW sample, referred to us as sample E, at a substrate temperature of 855°C. As will be discussed in detail in Chapter 5, owing to the high substrate temperature, nominally Ga-rich growth conditions [$\Phi_{Ga} = (16.5 \pm 0.5)$ nm/min] were required to compensate for the high Ga desorption rate.[50,134] The total growth time was 7 h and the delay time before detecting the formation of the first GaN NWs by RHEED (i. e., the incubation time) was as long as 90 min. We then prepared another sample using a two-step growth approach (sample F). During the first step of the growth, we used the growth conditions of sample A, namely, a Ga flux of (5.5 ± 0.5) nm/min and a substrate temperature of 815°C. After 25 min, we observed the onset of NW nucleation by RHEED. At that point, we changed to the growth conditions of sample E by first increasing the substrate temperature and subsequently the Ga flux. During all time, the N shutter was kept open. Therefore, during NW nucleation and elongation stages, the growth conditions of samples E and F were the same. The growth was finished after a total growth time of 6 h, i. e., 1 h less than for sample E. The growth conditions of both samples are summarized in Table 4.2.

Figure 4.8 shows the temporal evolution of the desorbing Ga flux during the growth of samples E and F. Unfortunately, due to some instabilities of the MBE chamber, the QMS measurements were not very stable at that time and were additionally influenced by the RHEED gun due to some cross-talk. As the obtained measurement nonetheless illustrates the basic idea, we chose to show it anyway. However, the reader is advised to keep in mind the unreliabilities of these two measurements. In Figure 4.8, the measurement for sample E is depicted in blue. As, in addition, the ion gauge that is usually used to calibrate the impinging Ga flux was inoperative, the impinging Ga flux had to be adjusted in situ using the QMS. This is the reason for the increase in the measured Φ_{des} in the beginning of samples E and F. Then, during the incubation stage, all impinging Ga desorbed. For sample E, the first GaN spots appeared in RHEED after 97 min. The end of the incubation

Table 4.2: Summary of the growth conditions used for samples E and F. The impinging N flux was kept constant at $\Phi_N = (11.0 \pm 0.5)$ nm/min.

		sample E	sample F
step 1	substrate temperature (°C)	855	815
	growth time (min)	420	25
	Ga flux Φ_{Ga} (nm/min)	16.5	5.5
step 2	substrate temperature (°C)	-	855
	growth time (min)	-	335
	Ga flux Φ_{Ga} (nm/min)	-	16.5

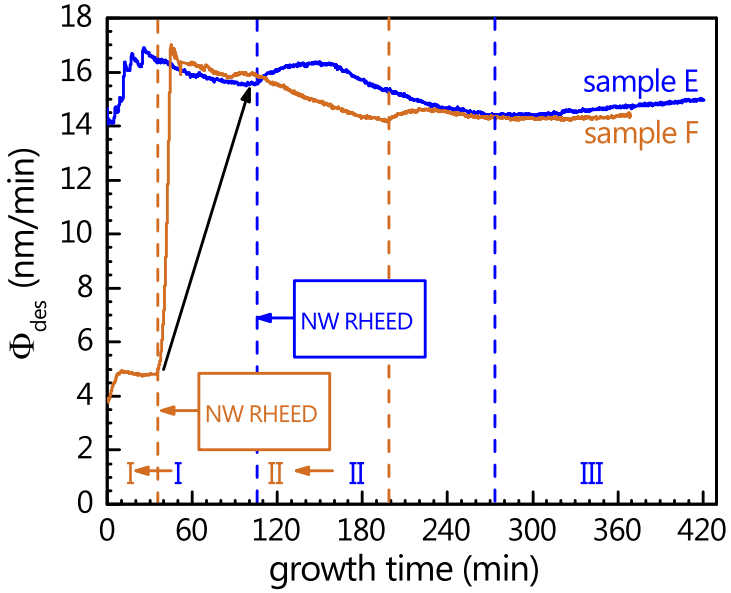

Figure 4.8: Temporal evolution of the desorbing Ga flux per unit area for samples E and F.

stage is therefore indicated by the first dashed blue line. However, due to the crosstalk mentioned above, the measured desorbing Ga flux, was not stable during this time. Only after the first GaN spots had been observed in RHEED, the RHEED gun was actually switched off. At that time, the measured desorbing Ga flux started to recover to its original level of 16.5 nm/min before eventually showing the typical double-logistic behavior. For sample F, depicted in Figure 4.8 in ocher, the crosstalk between QMS and RHEED was observed less pronounced. In the first 35 minutes, the desorbing Ga flux is low, due to the reduced impinging Ga flux of about 5.5 nm/min used in the low temperature nucleation step. After the first GaN spots were observed in RHEED for sample F, the growth conditions were switched to those of sample E. Consequently, the desorbing Ga flux then increased to 16.5 nm/min. Thereby, the duration of the incubation stage was reduced by approximately one hour. During the entire nucleation stage (stage II) as well as the elongation stage (stage III) the growth conditions of samples E and F were identical within the experimental error. The increase in the desorbing Ga flux during the elongation stage has not been observed for conventional NWs grown at lower temperatures. It will turn out that it may originate from the simultaneous decomposition of NWs during growth that becomes relevant at elevated temperatures and for long enough NWs. This matter will be discussed in detail in the next chapter.

Figures 4.9[(a),(c)] and [(b),(d)] show plan-view and cross-sectional scanning electron micrographs of samples E and F, respectively. Despite the different growth conditions used during the incubation stage and the shorter total growth time employed for growing sample E, the samples look indistinguishable. For both samples, the NWs seem to exhibit a similar density as well as comparable lengths and cross-sectional shapes. Interestingly, the cross-sectional scanning electron micrographs reveal that the diameter of these GaN NWs increases during growth. Such a temporal evolution in the NW diameter has not been observed before in NW ensembles grown a lower temperatures. This fact suggests that, due to simultaneous decomposition, the effective Ga/N ratio is not constant during growth at 855°C.[65]

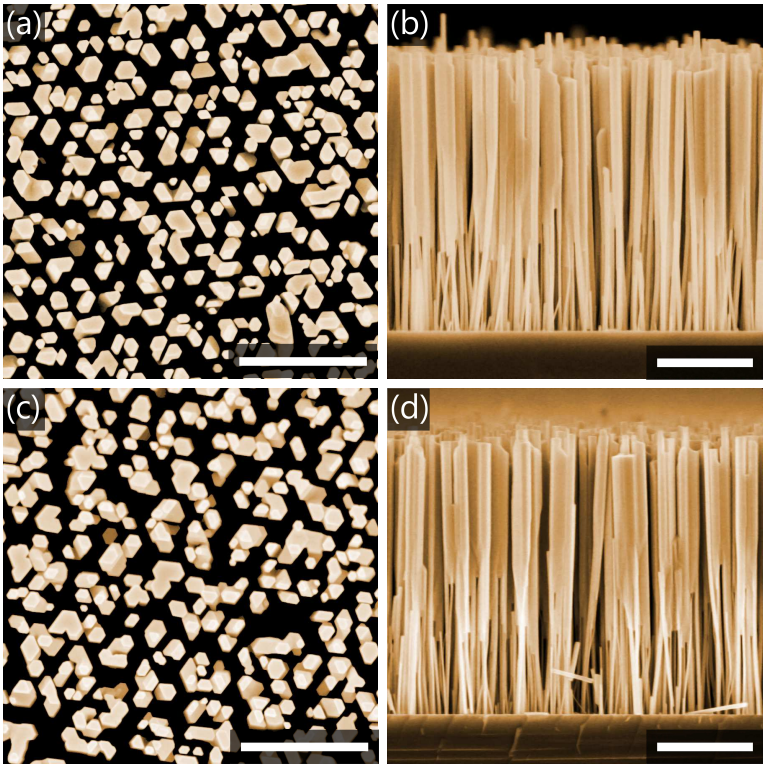

Figure 4.9: (a),(c) Plan-view and (b),(d) cross-sectional scanning electron micrographs of samples E and F, respectively. The scale bars correspond to 500 nm for plan-view and 1 µm for cross-sectional micrographs. SEM measurements carried out by Anne-Kathrin Blum.

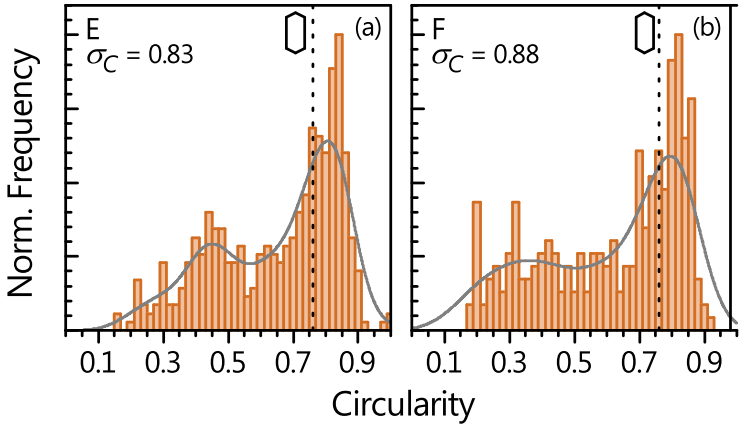

Figure 4.10: Circularity histograms of the cross-sectional shapes of the GaN NWs from (a) sample E and (b) sample F. The solid lines show the kernel density estimation of the respective histogram, the dashed lines indicate the threshold value ζ_A. The coalescence degrees σ_C are derived from eq. 3.2.

Table 4.3: NW length, area coverage, coalescence degree, diameter and NW number density of samples E and F as determined from the statistical analysis of scanning electron micrographs.

	sample E		sample F	
length (µm)	3.0	$\pm$ 0.1	3.0	$\pm$ 0.1
area coverage (%)	46	$\pm$ 1	44	$\pm$ 1
coalescence degree (%)	83	$\pm$ 2	88	$\pm$ 2
average uncoalesced diameter (nm)	111	$\pm$ 3	111	$\pm$ 4
NW number density ($10^9/\mathrm{cm}^2$)	4.2	$\pm$ 0.4	4.0	$\pm$ 0.4

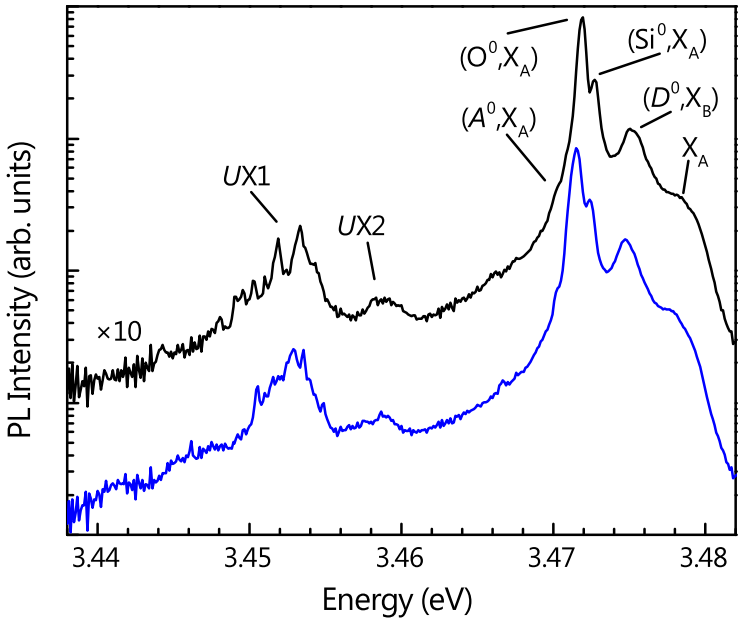

Figure 4.11: Normalized and vertically shifted low-temperature (10 K) PL spectra of samples E (black, top) and F (blue, bottom). PL measurements carried out by Pierre Corfdir.

Figure 4.10 depicts the circularity histograms of the cross-sectional shapes of NWs from samples E and F. Due to increase in NW diameter during growth, the coalescence degrees were derived from the circularity histograms without introducing a diameter limit for uncoalesced NWs. The coalescence degrees are indicated in Fig. 4.10 and listed in Table 4.3, where we also show the values of the average length, diameter, area coverage, and total number density. As expected from the visual inspection of Fig. 4.9, the quantitative analysis of the scanning electron micrographs reveals that, within the experimental error, the morphological properties of samples E and F are almost identical.

Furthermore, we also compared the low-temperature (10 K) near band-edge PL spectra of samples E and F, which are shown in Fig. 4.11. In both cases, the spectrum is dominated by the recombination of A excitons bound to neutral O [$(\mathrm{O}^0, X_\mathrm{A})$] and Si donors [$(\mathrm{Si}^0, X_\mathrm{A})$] at 3.471 and 3.472 eV, respectively. Due to the high substrate temperature,[86,134] these transitions are as narrow as 0.7 meV. Beside these lines, we also observe the recombination of B excitons bound to neutral donors [(D^0, X_B)], free A excitons [X_A], A excitons bound to neutral acceptors [(A^0, X_A)], and the so-called UX band[43,77–80] [(U, X_1), (U, X_2)], recently attributed to inversion domain boundaries.[148] For both samples, all these transitions are

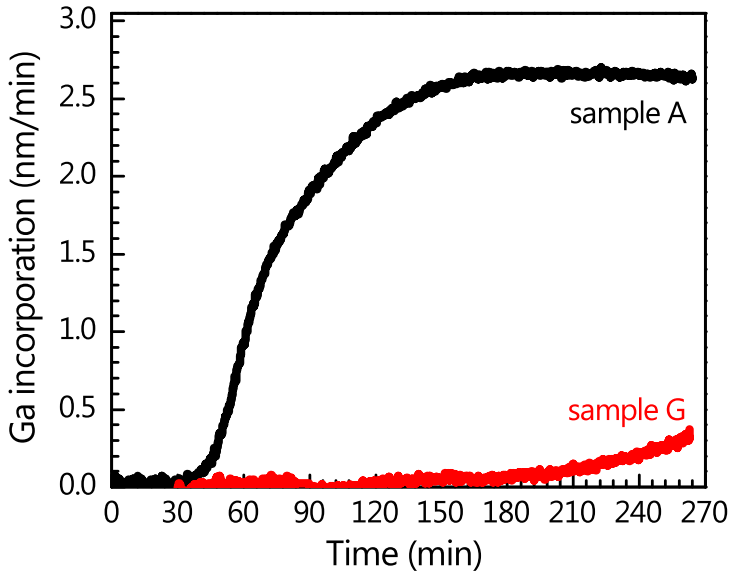

Figure 4.12: Temporal evolution of the Ga incorporation rate per unit area for samples A and G. For sample G, the substrate temperature was increased by 30°C 5 min after observing the onset of NW nucleation by RHEED.

centered at the same energy and exhibit comparable linewidths and intensities. Therefore, the PL spectra and intensities of samples E and F are quite similar.

The strong similarities between the morphological and optical properties of samples E and F reveal that the growth conditions employed during the incubation stage, i. e. prior to NW nucleation, do not influence the properties of the final NW ensemble. Thus, the present two-step growth approach enables the growth of NW ensembles in shorter times without affecting their final properties.

4.3. The limitations of the two-step growth approach

In the following, we will present attempts that were made to explore the limits of a two-step growth. We will report on samples that were prepared in a fashion comparable to those in Section 4.1 with the distinction that the temperature was raised even earlier during nucleation. These conditions resemble those used by Carnevale et al. and will allow us to better compare their experiments[133] to those obtained here. Finally, we will attempt a comprehensive interpretation of the mechanisms governing the influence of the two-step growth observed in this chapter.

Analogously to samples B to D, introduced in Section 4.1, we prepared an additional sample where the substrate temperature was raised accordingly by 30°C but already 5 minutes after the first GaN spots had been observed in RHEED (sample G). Figure 4.12 shows the temporal evolution of Φ_{inc} for sample G along with that of the reference sample, sample A, for comparison. At the time when the substrate temperature was increased, no change in Ga incorporation could be observed yet. Furthermore, no significant Ga incorporation is measured in the first 3 h of growth. Only then, an increase in Ga incorporation is observed, pointing toward a strong decrease in the NW formation rate.

Figure 4.13(a) shows the RHEED pattern along the [11$\bar{2}$0] azimuth of sample G at

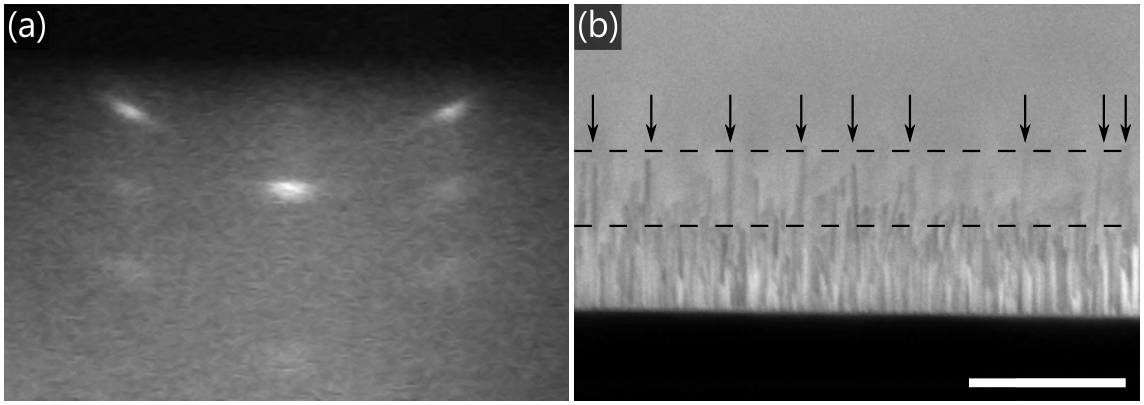

Figure 4.13: (a) RHEED pattern along the [11$\bar{2}$0] azimuth of sample G at the end of the first growth step. (b) Cross-sectional scanning electron micrograph of sample G after growth. The dashed lines illustrate the two distinct NW height groups. The arrows indicate the sparse long NWs that have nucleated in the first growth step. The scale bar corresponds to 1 µm.

the end of the first growth step. At that time enough NWs had nucleated to observe a characteristic GaN NW RHEED pattern. However, although the growth conditions in the second step were identical to those of samples B to D, it took another 2.5 h before significant NW nucleation was resolvable in QMS. Figure 4.13(b) depicts a cross-sectional scanning electron micrograph of sample G after growth. It shows that the resulting NW ensemble is constituted of two groups of NWs. Some NWs are already $\approx$ 1 µm long. The majority of the NWs, however, are shorter than 300 nm. The combined interpretation of RHEED and SEM images suggests that the long NWs are those that have formed already in the first growth step. On the other hand, the short NWs, having reached already a considerable density, seem to be originating from the increased NW nucleation observed in QMS in the last hour of growth. In comparison to samples B to D, even the longest NWs are again shorter. This means, their axial growth rate in the second growth step has further dropped, although the growth conditions of the second step were identical.

Attempting to prevent the onset of new NW nucleation as observed for sample G, we have prepared to more two-step samples, samples H and J, where we increased the substrate temperature of the second step by another 10°C, being now 855°C. Figure 4.14 shows the temporal evolution of the Ga desorption for samples H and J, along with that of reference sample A for comparison. Neither for sample H nor for sample J, a change in the desorbing Ga flux was observed within the growth times of about 5.5 h and 9 h, respectively. Therefore, a determination of the Ga incorporation rate was not reliable, and Figure 4.14 instead depicts the temporal evolution of the desorbing Ga flux Φ_{des}.

Figure 4.15 depicts plan- and tilted-view scanning electron micrographs of samples H and J. Both samples show a low-density of NWs with a broad distribution in length. In terms of general morphology, these samples resemble very much those reported by Carnevale et al.[133] We have analyzed the scanning electron micrographs and obtained average diameters, maximum NW lengths, axial growth rates, and NW number density for samples H and J. Those values are given in Table 4.4.

The longest NWs, we believe again to have nucleated already during the low-temperature step. However, as the growth temperature was raised immediately after the onset on NW nucleation (as observed by RHEED), the major part of their elongation must have taken place in the high-temperature step. When calculating the axial growth rate of the

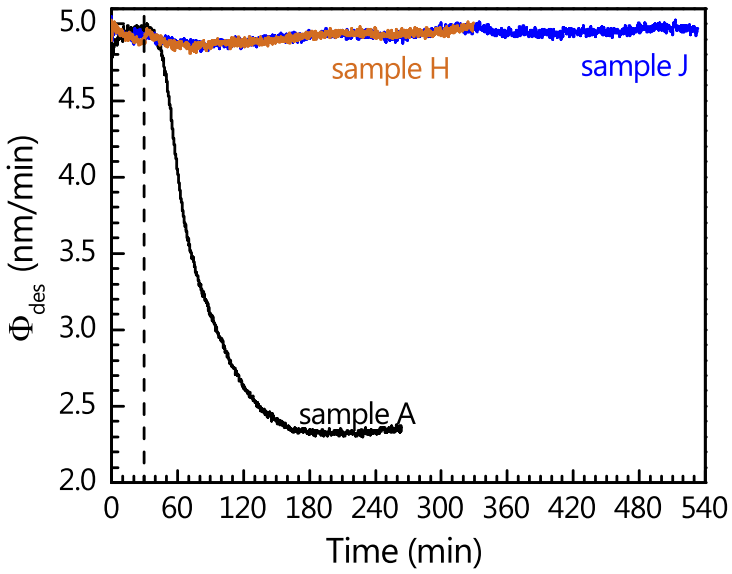

Figure 4.14: Temporal evolution of the Ga desorption per unit area of samples H and J. For both samples, the substrate temperature was increased by 40°C directly after the onset of NW nucleation was observed in RHEED.

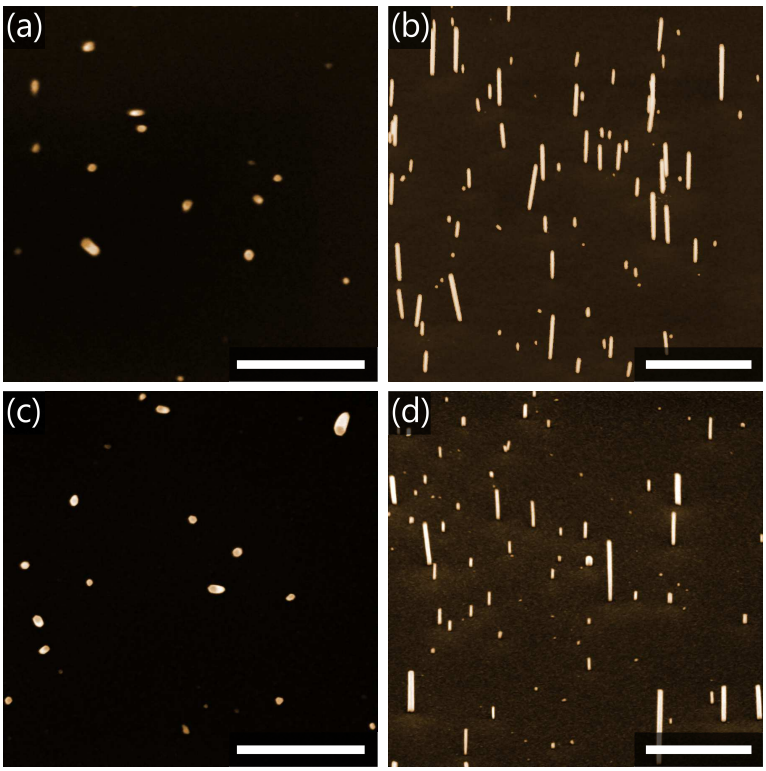

Figure 4.15: (a),(c) Plan-view and (b),(d) tilted-view scanning electron micrographs of samples H and J, respectively.

Table 4.4: Maximum NW length, average diameter, growth rate, and NW number density of samples H and J as determined from the analysis of plan-view scanning electron micrographs.

	sample H		sample J	
average diameter (nm)	42	$\pm$ 2	39	$\pm$ 2
maximum NW length (nm)	580	$\pm$ 20	970	$\pm$ 20
axial growth rate (nm/min)	1.9	$\pm$ 0.1	1.9	$\pm$ 0.1
NW number density (10^8/cm^2)	6.9	$\pm$ 0.3	9.7	$\pm$ 0.3

longest NWs, we obtain a value of 1.9 nm/min for both samples. This value is again lower than the axial growth rates of samples B, C, D, and G and significantly below the impinging N flux as well as the Ga flux. The presence of a significant number of shorter NWs of different length along with the fact that the total NW number density increased from sample H to sample J, reveal the slow but continuous nucleation of NWs during the second step. However, due to the extreme growth conditions, the NW formation rate is very low. In fact, samples H and J look well comparable to those reported by Carnevale et al. Judging from the scanning electron micrographs provided in Ref. [133], a broad distribution in length is observed. Thus, we believe that in Ref. [133] the nucleation and elongation phases were also not fully separated but rather extremely stretched.

As a result of the here presented experiments, we believe that using such a two-step growth process does not allow to significantly reduce the NW number density of long and homogeneous NW ensembles. If the growth conditions of the second step are too extreme and the temperature is raised very early during nucleation, the nucleation process can be slowed down drastically. However, also the axial NW growth rate collapses and the resulting NW ensemble will exhibit a broad distribution in length. Interestingly, also for these extreme growth conditions, the observed NWs in average exhibited diameters around 40 nm. This shows again, that a spontaneous fabrication of much thinner NWs is not achievable using conventional spontaneous GaN NW formation.

An additional attempt to prevent NW nucleation in the second growth step one might think of is to simultaneously decrease the impinging active N flux during the second step. As the existing NWs only elongate at an axial growth rate of 1.9 nm/min, the impinging N flux could be reduced by a factor of 5 without limiting the axial growth rate. In contrast, the probability of new NW formation should be drastically reduced. However, as the amount of the N excess influences the probability of Ga desorption,[95] the axial growth rate of the existing NWs might nonetheless be indirectly influenced and thereby annihilate the selective impact proposed above. Preliminary experiments on that matter were indecisive, however. At the end, this idea was not further pursued as the low growth rate in any way requires very long growth times. Thus, the entire growth experiments are rather impractical.

Finally, we need to discuss why we observe a continuous nucleation of NWs even under growth conditions where in a conventional one-step growth experiment no NW would be expected to nucleate within the given growth time.[50] In other words, why does the NW formation rate that is observed in the second growth step, seem to be influenced by the progress of NW nucleation made in the first step. We want to stress, however, that this discussion is purely hypothetical and there are far more sophisticated experiments and theoretical models required, to reliable answer those questions.

In principle, this behavior can be explained in two ways.

Hypothesis 1 relies on a continuous evolution of the cap-shaped islands that constitute the predecessors for NW formation. If these cap-shaped islands, during the first growth step, have already undergone a significant fraction of their development toward that state where they undergo a shape transition, there is less development required in the second growth step. This hypothesis would also explain the observation made in Section 4.2, that the growth conditions of the incubation stage do not influence the properties of the resulting NW ensemble.

An alternative hypothesis is that NW nucleation is actually a self-enforced process. Analogously to the considerations of the height equilibration of GaN NWs made by Sabelfeld et al.,[125] the desorption and adsorption of Ga adatoms may play a significant role in the nucleation dynamics of GaN NWs. If no NWs have nucleated yet, a Ga atom desorbing off the substrate will escape and can no longer contribute to growth or nucleation. Once the first NWs have nucleated, however, a desorbing Ga adatom has a finite probability of being readsorbed on the sidewall of an existing NWs. There, it may contribute to elongation or be redesorbed again. If the adatom desorbs again off the NW sidewall, it may, once again, impinge on the substrate and has another chance of contributing to nucleation. Thereby, as the NW density, and length, increases, the escape probability of a single Ga atom continuously decreases and the number of chances a Ga atom has to contribute to growth, or nucleation, simultaneously increases. As mentioned before, a proper investigation of this hypothesis requires more extensive simulations and correlations to experiments.

Independent of the exact mechanism, we observe that in a two-step growth process, the nucleation progress made in the first step significantly influences the development that is observed in the second step. In addition, we have demonstrated that the growth conditions used during the incubation stage before nucleation has started influence neither the morphological properties nor the low temperature PL spectra of NW ensembles. Thus, it is possible to obtain NW ensemble with similar properties but in shorter growth times by using more favorable growth conditions (lower substrate temperature and/or higher impinging fluxes)[50] during the incubation stage. In contrast, a variation in the growth parameters during the nucleation stage has a strong influence on the properties of the final NW ensemble. The impact on the final morphology depends on the time at which the growth conditions are modified during the nucleation stage. This growth approach does not allow a significant reduction in the NW number density because further nucleation is not completely suppressed after modifying the growth parameters. However, a two-step growth approach is found to be an efficient method to gain control over other important parameters such as area coverage, coalescence degree, and average NW diameter.

In other words, we can imagine the two-step growth procedure as an interpolation between the low-temperature growth conditions of the first step and the high-temperature growth conditions of the second step. If the time at which the growth conditions are changed is during or at the end of the incubation stage, the properties of the resulting NW ensemble will be identical to those of GaN NWs grown solely at the high temperature. In contrast, if the temperature is increased only after the nucleation stage is completed, i.e., in the elongation stage, the morphology is defined by the low-temperature step. In between, if the temperature is raised during the nucleation stage, one can interpolate between the morphology of both.

This "interpolation" picture concisely points out the advantages and limitations of a two-step growth procedure. The two-step growth enables the fabrication of GaN NWs which usually require growth conditions that come at the price of a long delay time for NW

nucleation in a shorter time. Thus, two-step growth will prove valuable for NW growth at higher substrate temperatures as well as for growth experiments targeting low NW diameters. For the fabrication of long, homogeneous ensembles, however, the obtainable characteristics such as NW number density, diameter, area coverage and coalescence degree are limited by the respective values of the corresponding one-step NW ensembles.

5. High-temperature growth of GaN nanowires

A major limitation of the spontaneous formation of GaN NWs in MBE, and for GaN growth in MBE in general, is the achievable growth temperature. The main handicap in the fabrication of high-quality GaN layers by MBE is the limitation in temperature. As was discussed in detail in Section 3.3.1, the achievable growth temperature in MBE is limited by thermal decomposition[51,95] and the requirement to maintain a surfactant Ga-adlayer on the surface to promote step-flow growth.[52,96–98] For these reasons, the typical substrate temperatures reported for the growth of GaN films by PA-MBE are around 1000 K.[52,98] This value is well below the theoretically predicted optimal growth temperature of covalently bonded semiconductors (approximately half of the melting point temperature, which is 2540 K for GaN[90]) and approximately 300 K lower than the optimal temperatures used in MOCVD or HVPE.[91–93]

The growth of GaN in the form of NWs facilitates the use of significantly higher substrate temperatures for GaN growth in MBE. GaN NWs does not require the presence of a Ga adlayer because they form only under N excess.[35,36,49,65,74] In addition, the N-rich environment allows a significant reduction in the effective GaN decomposition rate.[95]

As we discussed in detail in Chapter 3.3.2, the maximum achievable substrate temperature for the spontaneous formation of GaN NWs is limited by the long delay time that precedes the spontaneous formation of GaN NWs in MBE.[50] Thus, the key to achieving even higher growth temperatures consists in reducing the incubation time as much as possible. Furthermore, in the course of our prior experiments, we found GaN decomposition to be negligible during NW elongation up to at least 835°C.[50] At higher growth temperatures, however, GaN decomposition must become significant at some point.

In Section 5.1.1, we use three different growth approaches to decrease the incubation time and thereby enable the spontaneous formation of GaN NWs on Si substrates at to our knowledge so far unexplored substrate temperatures (up to 905°C). The first approach consists in leaving the common regime of nominally N-rich growth conditions, i.e., a ratio between the impinging Ga and N fluxes lower than one. Instead, we use nominally Ga-rich growth conditions (in terms of the impinging fluxes) to compensate for the high desorption rate of Ga adatoms at elevated substrate temperatures. In a second approach, we utilize the two-step growth procedure introduced in Chapter 4 in which an initial low-temperature step favoring rapid nucleation is followed by a high-temperature elongation stage. Finally, in a third approach, we enhance GaN nucleation by introducing an AlN buffer layer. Afterward, we study the influence of the growth temperature on the ensemble morphology.

In Section 5.1.2, we discuss additional phenomena that we observed during the growth of GaN NWs at high temperature, namely the appearance of Si melt-back etching and an abrupt radial widening when growing long NW ensembles. Both effects have not been reported before for GaN NWs prepared at conventional growth temperatures.

In Section 5.1.3, we find that the obtained high-temperature GaN NW ensembles exhibit unprecedented structural and optical properties. The low-temperature PL spectra of the

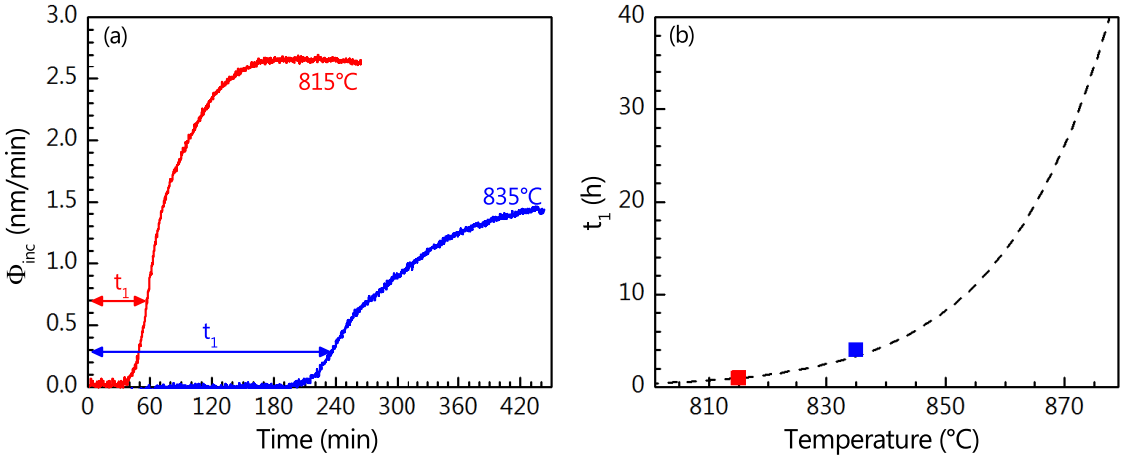

Figure 5.1: (a) Temporal evolution of the Ga incorporation rate per unit area for reference samples grown at 815°C and 835°C with identical fluxes. The arrows mark the respective average NW formation times t_1. (b) Increase of the average NW nucleation time with temperature if the impinging fluxes were kept constant. The squares correspond to the experimentally determined average NW formation times in (a). The dashed line gives the extrapolation to higher temperatures following eq. 3.6.

high-temperature-grown GaN NWs will turn out to be comparable to those of state-of-the-art free-standing GaN (FS-GaN) layers grown by HVPE. However, the improved properties cannot be solely explained by the higher growth temperature. It turns out, a significant Si incorporation is provoked by the onset of Si melt-back etching which affects the exciton recombination in the NWs.

In Section 5.2, we attempt to disentangle the contributions of high-growth temperature and Si incorporation. There, we report on the spontaneous formation of GaN NW ensembles on C-face SiC-6H(000$\bar{1}$) substrates at low and high growth temperatures. SiC is believed to be more stable against temperature compared to Si. Therefore, Si melt-back etching is not expected for these samples. In Section 5.2.2, we will discuss the properties of GaN NW ensembles grown on SiC(000$\bar{1}$) at different substrate temperatures. Finally, in Section 5.2.3, we will examine the impact of intentional Si doping on the optical properties of the samples.

Some of the results presented in this Chapter have been published in Ref. [134].

5.1. High-temperature growth of GaN nanowires on Si

5.1.1. Three growth methods to enable growth at high temperatures

In this section, we report on the growth of GaN NWs at high temperatures by reducing the incubation time that precedes NW formation. As we have discussed in Chapter 3.3.2, for given impinging Ga and N fluxes, the average delay time for NW formation increases exponentially with the substrate temperature.[50] In Figure 5.1(a), we show the temporal evolution of the Ga incorporation for samples grown using conventional growth conditions. For both samples, the impinging fluxes were identical, namely $\Phi_{Ga} = (5.5 \pm 0.5)$ nm/min and $\Phi_N = (11.0 \pm 0.5)$ nm/min. For the first sample, S815, the substrate temperature was set to 815°C, for the second (S835) 20°C higher. In fact, the former sample is the reference sample (sample A) already discussed in the previous

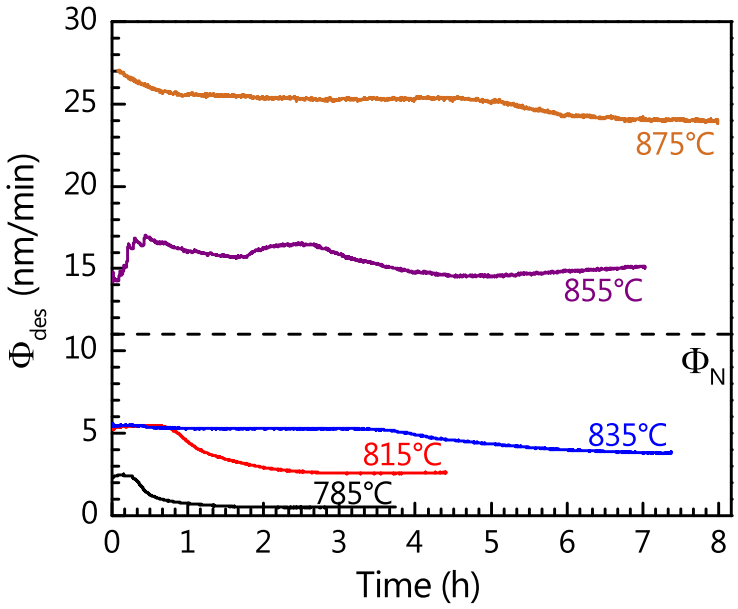

Figure 5.2: Temporal evolution of the desorbing Ga flux for GaN NW series grown at different temperatures. The dashed line corresponds to the impinging N flux Φ_N.

chapters. In Figure 5.1(a), the influence of the substrate temperature on the average delay time for NW formation t_1 for the two samples becomes obvious. While sample S815, NWs in average nucleate after 60 min, t_1 is as long as 240 min for sample S835. Figure 5.1(b) extrapolates the average delay time for NW formation t_1 for higher growth temperatures according to Equation 3.6. It thus represents a horizontal cut through the growth diagram depicted in Figure 3.11. When exceeding growth temperatures of 850°C, the NW formation in average takes more than 10 h. Thus, for the present conventional growth conditions, the used substrate of 835°C is already quite close to the practical limit for NW growth.

According to Equation 3.8, we can decrease the average delay time for NW formation at high growth temperatures by simultaneously increasing the Ga flux and thus using nominally Ga-rich growth conditions.[50] Figure 5.2 shows the temporal evolution of the desorbing Ga flux during the growth of GaN NW ensembles at different temperatures. The impinging N flux for all samples was $\Phi_N = (11.0 \pm 0.5)$ nm/min and is indicated in the graph. The samples at substrate temperatures between 785 and 835°C were grown using the conventional growth approach, namely, a constant III/V flux ratio lower than one. The growth time for the samples grown at 785 (S785) and 815°C (S815) was about 4 hours using Ga fluxes of $\Phi_{Ga} = (2.5 \pm 0.5)$ nm/min and $\Phi_{Ga} = (5.5 \pm 0.5)$ nm/min, respectively. In contrast, for the sample grown at 835°C (S835), we needed to increase the growth time up to 7.5 hours to obtain NWs with an average length comparable to that of the samples grown at lower temperatures. The samples at 855 (S855) and 875°C (S875) were grown using nominally Ga-rich growth conditions, using Ga fluxes of $\Phi_{Ga} = (16.5 \pm 0.5)$ nm/min and $\Phi_{Ga} = (25.0 \pm 0.5)$ nm/min, respectively. The use of these fluxes allowed a reduction of the average delay time for NW formation to 175 min for sample S855 and 325 min for sample S875. Thus, the first growth approach allows us to grow GaN NWs at substrate temperatures as high as 875°C in about the same time (7 and 8 h, respectively) as needed for the sample prepared at 835°C and a III/V ratio of 0.5. In Table 5.1 a summary of the growth conditions used for the samples presented in this section is given.

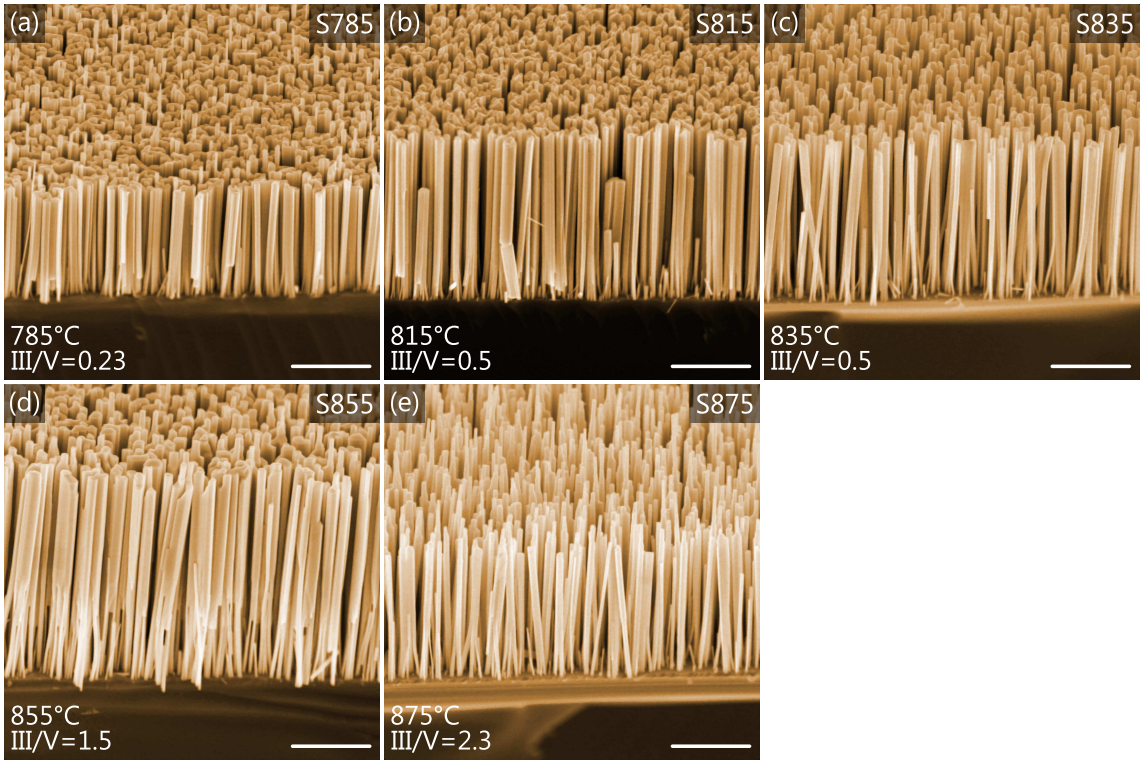

Figure 5.3: [(a)-(e)] Bird-eye scanning electron micrographs of GaN NW ensembles grown on bare Si using different temperatures and III/V flux ratios. The corresponding total growth time were 4, 4, 7.5, 7, and 8 h, respectively. The NW ensembles shown in (a)-(c) were grown using N-rich growth conditions while those shown in (d) and (e) were grown using nominally Ga-rich growth conditions. SEM measurements carried out by Anne-Kathrin Blum.

Table 5.1: Summary of the used growth parameters and NW properties. For the two-step samples the corresponding values for the nucleation step are given in brackets.

sample	S785	S815	S835	S855	S875	T855	T905	A875
remark						two-step	two-step	
substrate	Si(111)	Si(111)	Si(111)	Si(111)	Si(111)	Si(111)	Si(111)	AlN/Si(111)
substrate temperature (°C)	785	815	835	855	875	855 (815)	905 (815)	875
III/V ratio	0.23	0.5	0.5	1.5	2.3	1.5 (0.5)	3.2 (0.5)	0.9
total growth time (min)	225	264	437	422	480	363 (27)	526 (20)	270
time to observe RHEED spots (min)	11	24	133	97	180	25	20	1
average NW nucleation time (min)	24	59	241	175	325	116	246	$<$20
NW length (µm)	1.6	2.2	2.3	3.0	2.0	3.0	2.9	0.9

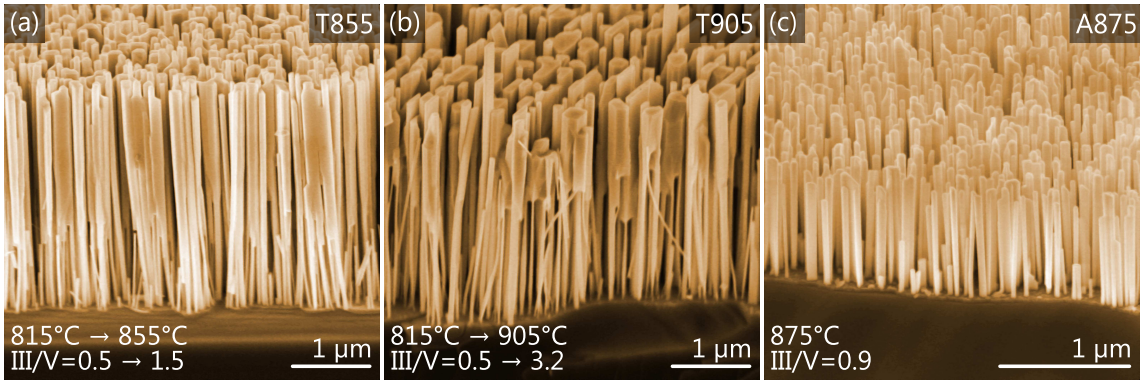

Figure 5.4: Bird-eye scanning electron micrographs of GaN NW ensembles prepared on Si at elevated substrates. In (a) and (b) we used a two-step growth scheme and in (c) we introduced an AlN buffer layer to enhance GaN nucleation. The corresponding total growth times were 6, 9, and 4.5 h, respectively. SEM measurements partially carried out by Anne-Kathrin Blum.

Figures 5.3(a)-(c) show scanning electron micrographs of GaN NW ensembles grown on bare Si at substrate temperatures between 785 and 835°C. Figures 5.3(d) and 5.3(e) illustrate the results obtained when the substrate temperature is increased using nominally Ga-rich growth conditions. The obtained GaN NW ensembles are of comparable density and morphology to those grown under N-rich growth conditions at lower temperatures [Fig. 5.3(a)-(c)]. We stress that, despite the large III/V flux ratios (up to 2.3) used to induce the formation of GaN NWs at 855 and 875°C, the growth still takes place under N excess because of the high desorption rate of Ga adatoms. Otherwise a compact layer would form due to NW radial growth.[65]

For growth temperatures above 850°C, Ga reacts with the Si substrate. This phenomenon referred to as "melt-back etching" is well-known from the growth of GaN on Si at high temperatures by other epitaxial growth techniques.[143] Its appearance in the high-temperature growth of GaN NWs will be discussed in detail in Section 5.1.2.

For the growth approach described above, the maximum achievable substrate temperature is still limited by the long incubation time that precedes the spontaneous formation of GaN NWs. The second growth approach thus aims at reducing further this incubation time by using a two-step growth scheme. The basic principle of a two-step growth was already extensively studied in Chapter 4. In a first step, conventional growth conditions, i. e., a moderate substrate temperature and a III/V flux ratio lower than one, are used to accelerate nucleation and thus keep the incubation time short. Once the formation of the first GaN NWs is detected by RHEED,[50,54,62] the substrate temperature is increased for the second step of the growth. For this second stage, the III/V flux ratio can be kept constant. However, the use of nominally Ga-rich growth conditions at this stage allows the use of even higher substrate temperatures.

Figure 5.4(a) presents a scanning electron micrograph of sample T855, a GaN NW ensemble prepared using the two-step growth scheme. As detailed in Section 4.2, for the first step, we used the low-temperature conditions employed for the growth of sample S815. After observing the onset of NW formation by RHEED, the substrate temperature and the III/V flux ratio were increased up to those of sample S855. The total growth time for sample T855 was about 6 h, i. e., approximately 1 h less than for the one-step sample S855. Nevertheless, despite the shorter growth time, the morphological properties of these

two samples are basically identical (compare Section 4.2, where the samples where labeled sample E and F, respectively).

Using this two-step growth approach, we attempted to grow GaN NWs at even higher substrate temperatures. Using a Ga flux of $\Phi_{\mathrm{Ga}} = (35 \pm 1)$ nm/min in the second growth step, we were able to obtain 2.9 µm long NWs at a substrate temperature of 905°C in a growth time of 9 h. Figure 5.4(b) presents a scanning electron micrograph of the obtained GaN NWs of sample T905. For this sample, we again observe the radial growth already discussed in Section 4.2 for the samples S855 and T855. Unfortunately, when preparing the sample, the mechanics for substrate rotation during growth were broken. Whereas in the samples above a uniform radial growth in all directions was observed, for sample T905, the radial growth was only observed on the NW sidewall where active N was impinging. This is in agreement with the calculations by Lymperakis and Neugebauer reporting that active N neither diffuses along the NW shell nor desorbs in order to be readsorbed on adjacent NW sidewalls. Instead, N tends to form molecular N and thus desorbs without contributing to growth.[109] As the resulting GaN NWs rather exhibit the shape of nanowalls, their properties will not be characteristic of high-temperature GaN NWs anymore. Therefore, this sample will not be considered in the further analysis. It shows, however, that the growth temperature of 875°C up to which we were able to maintain a typical NW morphology, is neither a maximum nor an optimized growth temperature.

Our third growth approach takes advantage of the fact that the incubation time depends not only on the growth conditions but also on the type of substrate.[40,104,105,144,145] For instance, it has been shown previously that the introduction of an AlN buffer layer favors GaN nucleation on Si substrates.[104,144,145] Therefore, for a single-step growth approach and identical impinging fluxes, one would expect to achieve higher growth temperatures on AlN-buffered Si substrates. Figure 5.4(c) demonstrates that this is actually the case. The introduction of a 26 nm thick AlN buffer layer for sample A875 enables the direct growth of GaN NWs at temperatures as high as 875°C under N-rich growth conditions (III/V = 0.9) in a growth time of 4.5 h owing to the significantly shorter incubation time ($<$ 5 min) compared to growth directly on Si. Of course, combining this approach with the use of nominally Ga-rich conditions facilitates even higher growth temperatures.

In the following, we investigate the influence of the growth temperature on the morphology of the NW ensembles. Therefore, we again employed a statistical shape analysis on plan-view scanning electron micrographs of the respective samples to determine NW area coverage, coalescence degree, average diameter and number density. Since the two-step growth as it was applied here has no influence on the morphology, as reported in section 4.2, sample T855 will not be discussed separately. It's properties are well comparable to those of sample S855. In contrast, the high-temperature NWs grown on the AlN-buffer provide additional insight and will be accordingly investigated and discussed.

Figure 5.5[(a)-(e)] depicts the circularity distributions of the GaN NWs grown at different temperatures. The amount of identified objects is comparable for all samples while a slight narrowing of the distribution is observed with temperature. In contrast, for sample A875, grown on the AlN-buffer at high temperature, the circularity distribution is narrower and contains more identified NWs. For each sample, the coalescence degree calculated according to Equation 3.2 is given. Its behavior with temperature, however, can only be understood when also regarding the changes in diameter and number density as will be discussed below.

Figure 5.6 shows the development of (a) the area coverage, (b) the coalescence degree, (c)

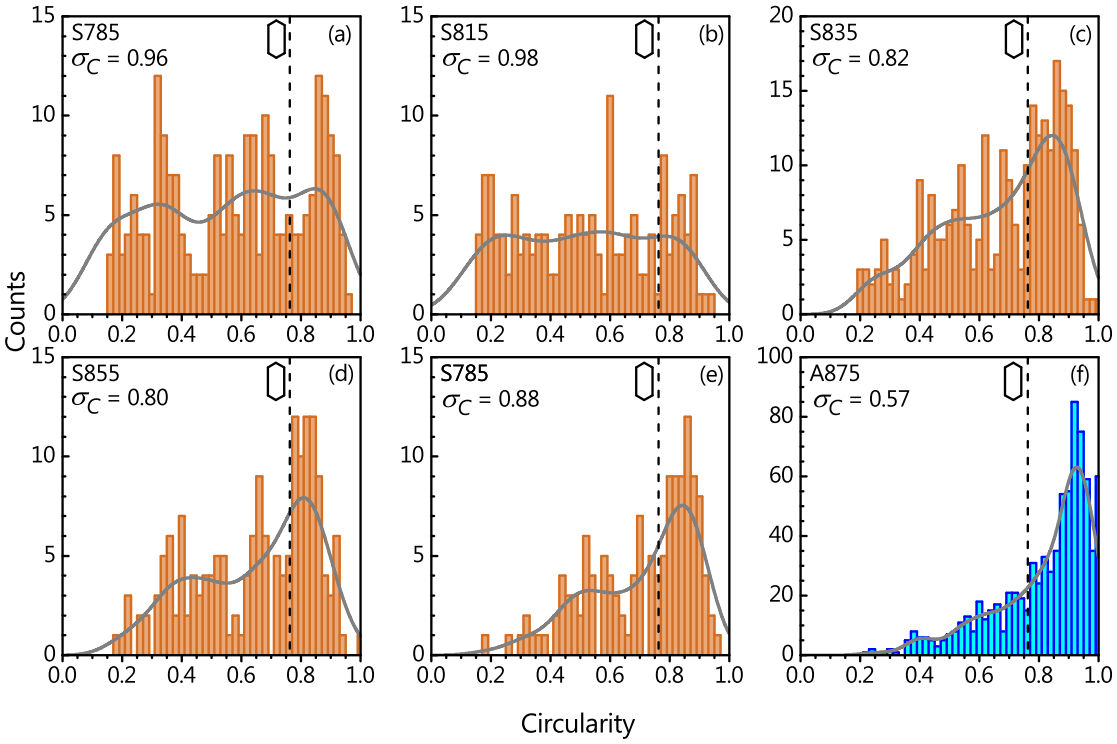

Figure 5.5: Circularity distributions of GaN NW samples grown at different temperatures. (a)–(e) correspond to the NWs grown on Si presented in Fig. 5.3. (f) corresponds to the NWs grown on AlN-buffered Si presented in Fig. 5.4(c).

the average uncoalesced diameter, and (d) the total NW number density as a function of the growth temperature. The black circles correspond to the temperature series on Si, the blue diamond refers to the sample prepared on the AlN-buffer at high temperature. For the area coverage and the average diameter, no clear correlation to the growth temperature is observed. In contrast, a weak influence of the growth temperature on the coalescence degree and a more pronounced effect on the total NW number density is found. A more detailed correlation is not straight forward as for those samples, by design of the experiment, not solely the temperature was changed but also the impinging Ga flux to compensate for desorption.

The average NW radius is determined by a self-regulated process governed by the effective Ga/N ratio at the NW tip.[65] In the given temperature series the effective III/V ratio of each sample is determined by both the impinging fluxes and the substrate temperature (which governs diffusion and the exchange of Ga atoms between adjacent NWs). Thus the obtained values of the NW diameter do not follow a well-defined temperature dependence but rather indicate the spread in the effective III/V ratio throughout the series. In addition, the sample prepared at 855°C suffers from a change in diameter along the NW axis. This phenomenon will be discussed in detail in Section 5.1.2.

The area coverage of the NWs is governed by the average NW diameter and the NW number density. As a consequence of the variation in the NW diameter, also for the area coverage no clear temperature dependence is obtained. However, as was discussed in Section 3.2.2, the quotient of area coverage and average uncoalesced diameter can be used to determine the total NW number density. By this, the number of constituent single NWs is estimated for each coalesced NW aggregate. As is evident in Figure 5.6 (d)

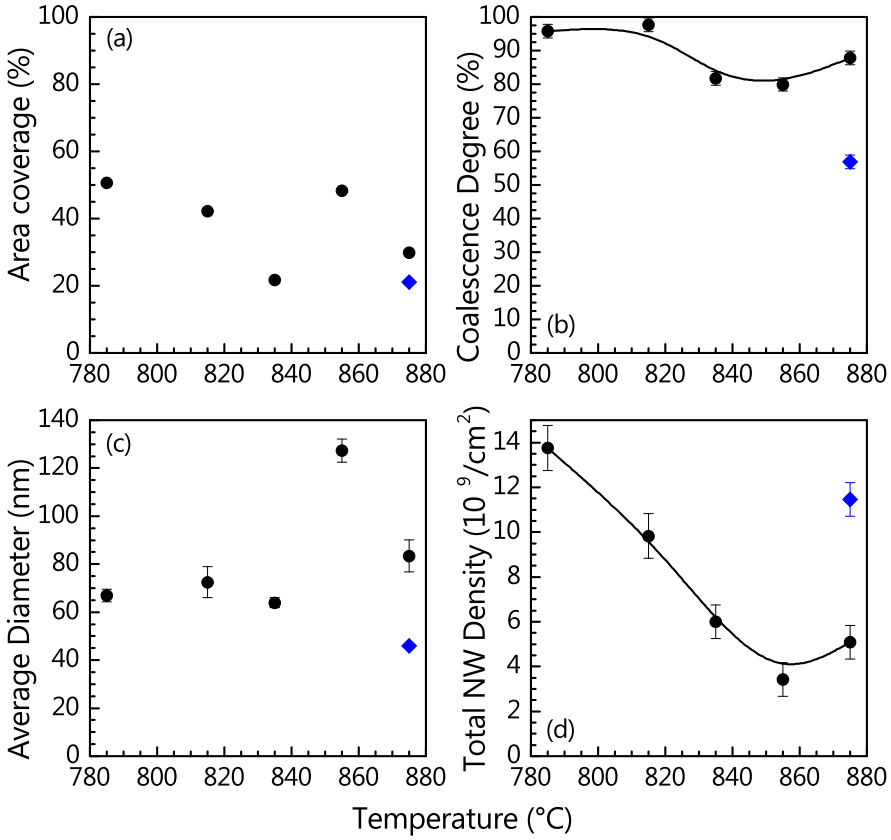

Figure 5.6: NW ensemble properties as a function of the growth temperature as obtained from statistical shape analysis. The black circles correspond to the NWs grown on Si presented in Fig. 5.3. The blue diamond corresponds to the NWs grown on AlN-buffered Si presented in Fig. 5.4(c). While the NW diameter [(c)] and the area coverage [(a)] are governed by the III/V ratio, the total NW number density [(d)] and coalescence degree [(b)] appear to depend primarily on temperature.

the total NW number density shows a clear temperature dependence decreasing from $1.4 \cdot 10^{10}$ NWs/cm^2 at 785°C down to $5 \cdot 10^9$ NWs/cm^2 at 875°C. In contrast, a total NW number density of $1.1 \cdot 10^{10}$ NWs/cm^2 is obtained for the NW ensemble grown at 875°C on the AlN-buffer where nucleation takes place in a time frame comparable to low-temperature growth on Si. The decrease in NW number density observed for the samples on Si is good agreement with previous reports where the total NW density was determined by manual counting and estimating.[73] However, as we extend the range of substrate temperatures used, we also achieve lower NW number densities. In Ref. [73], this trend was related to the decrease in the density of the spherical cap shaped islands as predicted by the standard island nucleation theory. In principle, the underlying mechanism is assumed to be the increase in diffusion length of the Ga adatoms on the Si substrate.[67] However, the number density may also be influenced by the shadowing of neighboring NWs. The question which parameters how determine the number density of a NW ensemble (and thereby also the coalescence degree) is not well-understood yet.

Owing to the decrease in NW number density, we also observe a slight drop in the coalescence degree with temperature. However, two additional effects come into play that distort the observation of a more pronounced decrease in coalescence degree. As

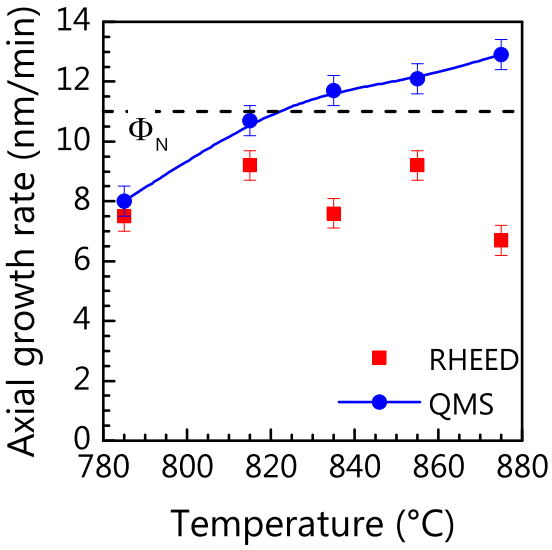

Figure 5.7: The axial growth rate of the NWs grown on Si as a function of the substrate temperature. Both results, relying on RHEED and QMS, are displayed.

discussed in Section 4.2, a pronounced radial growth is observed for the samples grown at 855°C. This radial growth is expected to cause an increase in the coalescence degree. For the samples prepared on Si at 835°C and 875°C, on the other hand, electrostatic attraction has lead to an additional coalescence of the long and thin NWs.[56,141] We believe this electrostatic charging to be caused by electrons in the MBE chamber originating either from the N plasma source or the RHEED electron gun. For shorter NW ensembles neither the radial growth (compare Section 5.1.2) nor the electrostatic attraction will become relevant and significantly lower coalescence degrees are expected. A comparable effect can be seen for the sample prepared on the AlN buffer. Despite the high NW number density a low coalescence degree of 57% is obtained. Due to the low impinging Ga flux at high temperature, the axial growth rate of that sample was no longer N-limited and the resulting NWs in average only 900 nm long. Thus, electrostatic attraction was not sufficient to cause an additional coalescence. In addition, the low average diameter and the good epitaxial alignment of the GaN NWs on the AlN buffer facilitated the preparation of a dense, homogeneous NW ensemble exhibiting a comparatively low coalescence degree. It must be noted, however, that GaN NWs prepared on AlN buffer layers at lower growth temperatures typically exhibit significantly higher degrees of coalescence.

Finally, we want to discuss the axial growth rate of the NW ensembles. Figure 5.7 depicts the axial growth rates obtained from QMS and RHEED measurements as a function of the substrate temperature for the series of GaN NWs prepared on Si. For the measurements obtained from QMS, the average delay time for NW nucleation t_1 was taken into account to determine the average NW growth time for each sample.[50] We observe a clear increase in the axial growth rate with temperature, eventually even exceeding the expected limit of the impinging N flux. At low temperatures, the high density of quickly nucleating NWs seems to result in an area coverage where the impinging Ga flux is not sufficient to achieve the self-regulated equilibrium and thereby an N-limited axial growth rate. For the sample grown at 785°C, the axial growth rate is actually Ga-limited.

At this point it is not yet clear why at high temperatures the NWs appear to be growing faster than the impinging N flux. One hypothesis is that, in contrast to current understanding,[109] there might be a certain diffusion of active N on the NW sidewalls that may lead a surplus of available active N on the NW tip and thus an axial growth rate above the

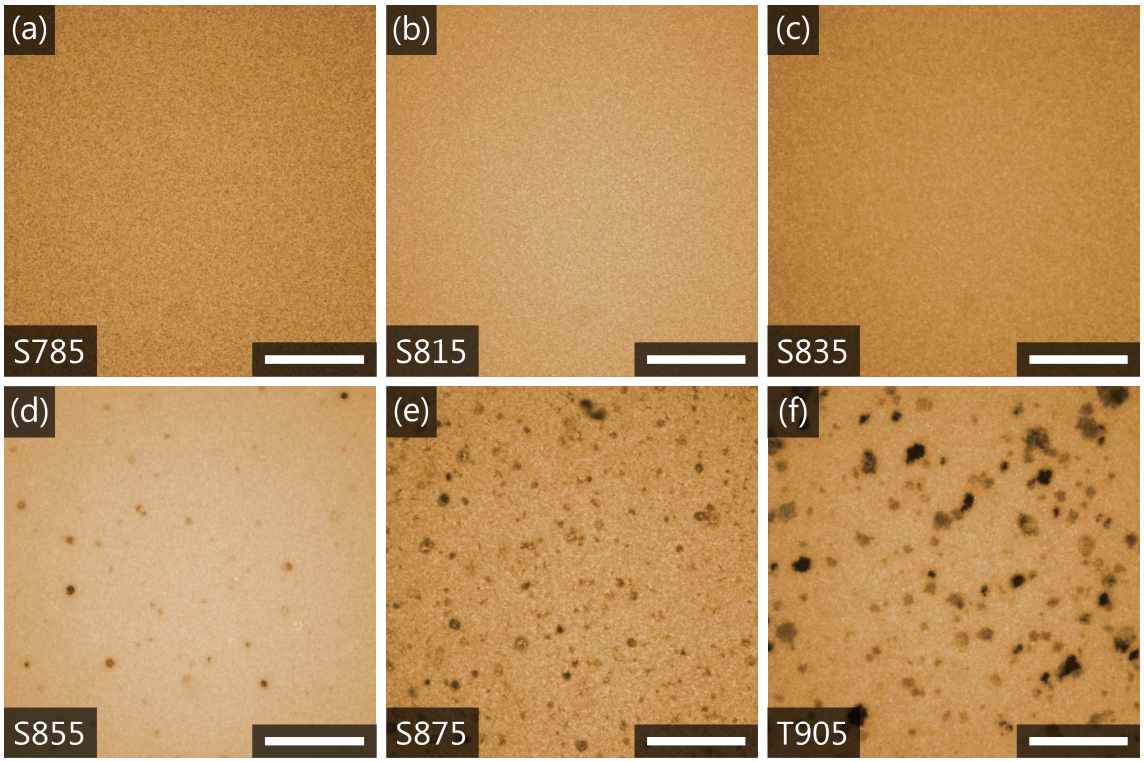

Figure 5.8: Optical micrographs of GaN NW ensembles grown on Si at different substrate temperatures. For temperatures above 850°C, Si melt-back etching is observed, apparent in the micrographs as grey and black spots. The scale bars correspond to 50 µm.

limit imposed by impinging N flux. At the moment, however, this explanation is solely an hypothesis and requires further verification.

For the determination of the axial growth rate using RHEED, the appearance of the GaN related spots in RHEED was used, as it has been previously done in literature.[113] However, as the RHEED measurement only determines the nucleation of the very first GaN NWs, the obtained growth times and rates are distorted by the influence of the NW formation rate τ_1. Only when NW formation takes place very fast, the error is low and the axial growth rates obtained from RHEED are in agreement with those of QMS. This means that especially for the high temperature growth, the axial growth rate can only be correctly determined from QMS.

5.1.2. Additional phenomena occurring at high-temperature

In the previous section, we have introduced three routes to fabricate GaN NWs in MBE at higher substrate temperatures. In addition, we have analyzed the basic morphological properties of such prepared NW ensembles and the influence of the growth temperature on the same. However, we have also observed clear morphological characteristics that have not been observed before for GaN NW growth at conventional temperatures.

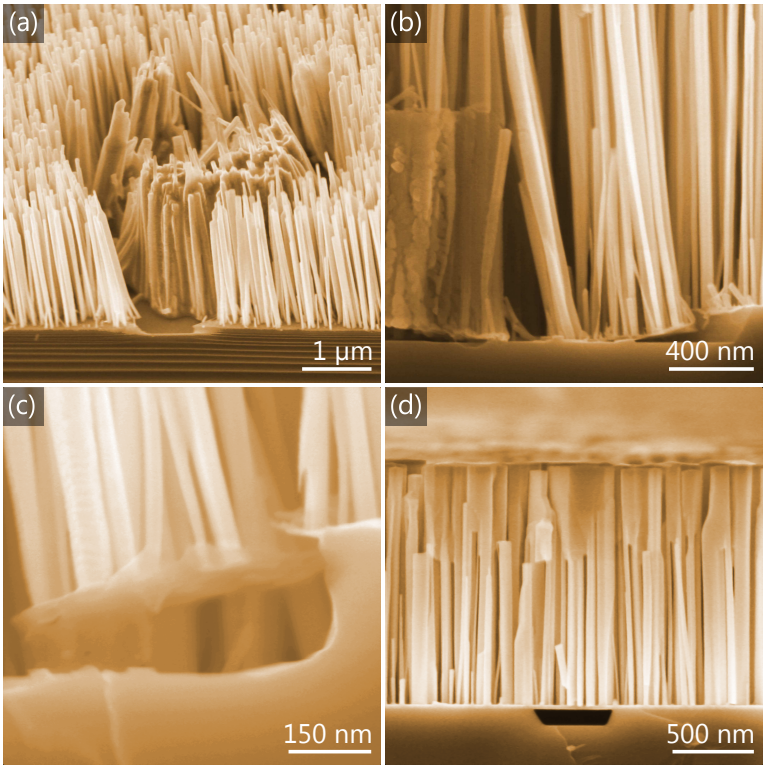

Figure 5.9: Scanning electron micrographs of high-temperature GaN NW ensembles exposed to Si melt-back etching. (a) The typical clustering of NWs above a melt-back etching site. (b) Shell formation on NWs above melt-back etching site. (c) melt-back etching into Si substrate. (d) melt-back etching through an AlN buffer layer substrate. SEM measurements partially carried out by Anne-Kathrin Blum.

Melt-back etching

For growth temperatures above 850°C, Ga reacts with the Si substrate. This "melt-back etching" is well-known from the growth of GaN on Si at high temperatures by other epitaxial growth techniques.[143] The consequence of Ga-induced melt-back etching on the NW morphology can be observed in both optical and scanning electron micrographs. In the former, we see a high density of dark spots. Fig. 5.8 shows plan-view optical micrographs of the temperature series on Si. With increasing substrate temperature the density and size of the dark spots increases. Fig. 5.9 shows scanning electron micrographs of these dark spots. They correspond to the formation of holes in the Si substrate. These holes can be as deep as a few hundred nanometers. The holes also provoke the tilting and clustering of the adjacent GaN NWs [Fig. 5.9(a)]. The use of AlN buffer layers has turned out not to be a sufficient protection to completely prevent Si melt-back etching [see Fig. 5.9(d)]. We believe that grain boundaries or pinholes present in the buffer layer[145] may serve as diffusion channels and thus enable melt-back etching.

In order to study the influence of the Ga flux on the NW morphology and the melt-back etching, additional samples were prepared on Si at high temperature (875°C). Figure 5.10 depicts tilted-view scanning electron micrographs of this Ga series, the corresponding optical micrographs are shown in Figure 5.11. In Figure 5.10(a), sample S875 from in the temperature series is shown again. Sample S875b, shown in Figure 5.10(b), was prepared using an even higher Ga flux of $\Phi_{\mathrm{Ga}} = (42 \pm 1)$ nm/min. For this sample, the melt-back

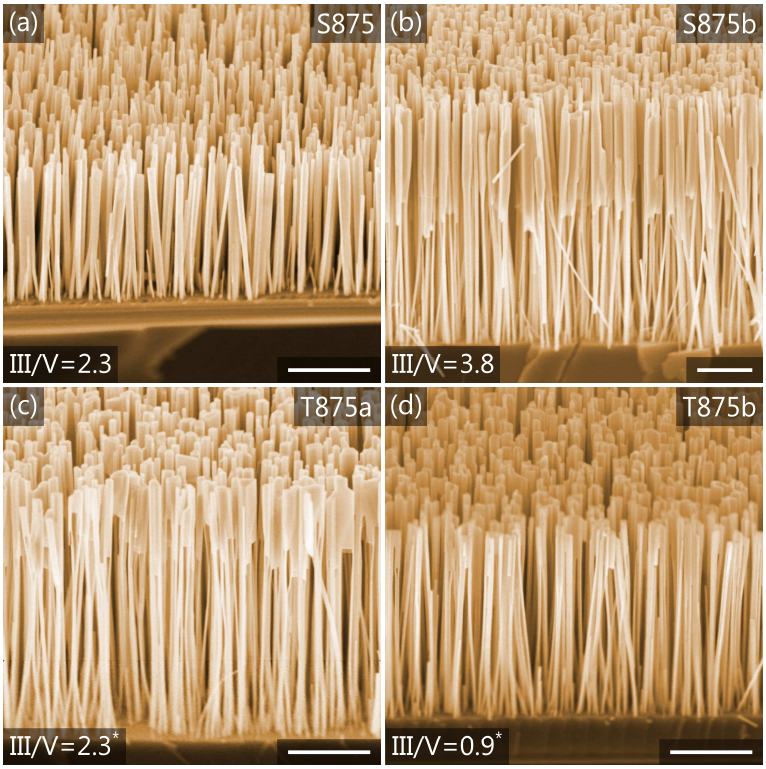

Figure 5.10: (a)-(d) Bird-eye scanning electron micrographs of GaN NW ensembles grown on Si at 875°C using different III/V flux ratios as indicated. For the samples in (c) and (d) a modified two-step growth method was employed, where a well-developed NW template was grown at low temperature before the temperature was raised for NW elongation. The indicated III/V ratio is that of the high-temperature elongation step. The scale bars correspond to 1 µm. SEM measurements partially carried out by Anne-Kathrin Blum.

etching is even more pronounced [see Figure 5.11(b)]. In addition, we observe again a variation in diameter as discussed before. The apparent radial growth points toward a change in the effective III/V ratio at the NW tip occurring for these samples. For the two samples shown in Figures 5.10(c) and (d), a two-step growth process was used where in the first step a well-developed NW ensembles was grown at low temperature. At the time the growth conditions were changed, the NWs were around 800 nm long, i.,e., long enough for the substrate to be shadowed by the existing NWs. For sample T875a, a Ga flux equivalent to that of sample S875, namely $\Phi_{\mathrm{Ga}} = (25.0 \pm 0.5)$ nm/min was used in the second step. We observe a similar amount of melt-back etching [Fig. 5.11(c)] and, in contrast to the sample prepared in a one-step fashion, again radial growth. For sample T875b, the Ga flux was only increased to $\Phi_{\mathrm{Ga}} = (10.0 \pm 0.5)$ nm/min in the high-temperature step, keeping the growth conditions also nominally III/V N-rich. For that sample, only sparse melt-back etching [compare Fig. 5.11(d)] is observed. Concerning the diameter variation, it seems as if here the growth was stopped just after the onset of the radial growth phase.

Summarizing, we can state that the melt-back etching occurs not only during NW nucleation but may also initiate later during growth. Thus, a two-step growth procedure with a a well-developed NW template does not per se prevent melt-back etching. The use of lower Ga fluxes in the high-temperature step, however, may reduce its extent. Principally, melt-back etching is occurring for growth temperatures above 850°C and

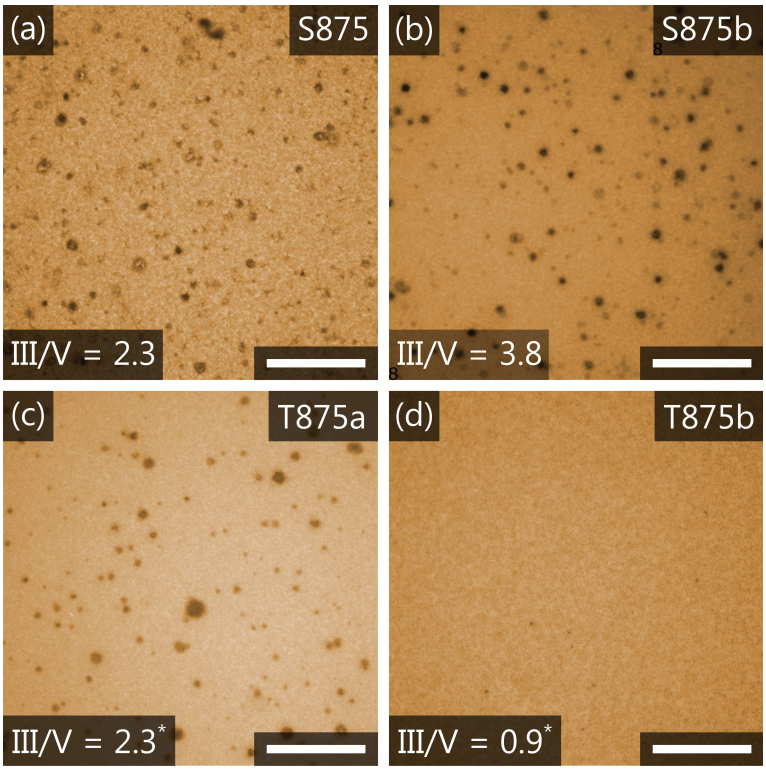

Figure 5.11: (a)-(d) Optical micrographs of GaN NW ensembles grown on Si at 875°C using different III/V flux ratios as indicated. For the samples in (c) and (d) a two-step growth method was employed, where a well-developed NW template was grown at low temperature before the temperature was raised for NW elongation. The indicated III/V ratio is that of the high-temperature elongation step. The scale bars correspond to 50 µm. The Si melt-back etching increases with increasing Ga flux.

quickly becomes predominant. The use of AlN buffer layers has turned out not to be a sufficient protection to completely prevent Si segregation. In addition, for many of the longer ensembles prepared at high temperatures, radial growth setting in at a later stage of the elongation phase is observed. This phenomenon will be discussed in the next section.

Abrupt radial growth

A detailed analysis of the high-temperature samples has shown that the NW length seems to be an important criterion whether radial growth is observed or not. For NW ensembles below 2.4 µm length, no indications of radial growth are found. In contrast, all NW ensembles grown at high temperature that are longer than 2.4 µm show signs of radial growth that become more pronounced the longer the final NW ensemble is. We believe that the decomposition of the existing NW base becomes relevant at temperatures above 850°C. After the Ga-N bond is broken, N then forms molecular nitrogen and desorbs.[109] Ga, however, may diffuse along the NW sidewall or desorb and be readsorbed on adjacent NWs.[125] Thereby, once the contribution of the Ga from decomposed GaN becomes significant, the effective III/V ratio at the NW tip may rise and result in an increase in NW diameter.[65] An alternative explanation where the radial growth is induced by NW coalescence can be ruled out from close inspection of the scanning electron micrographs.

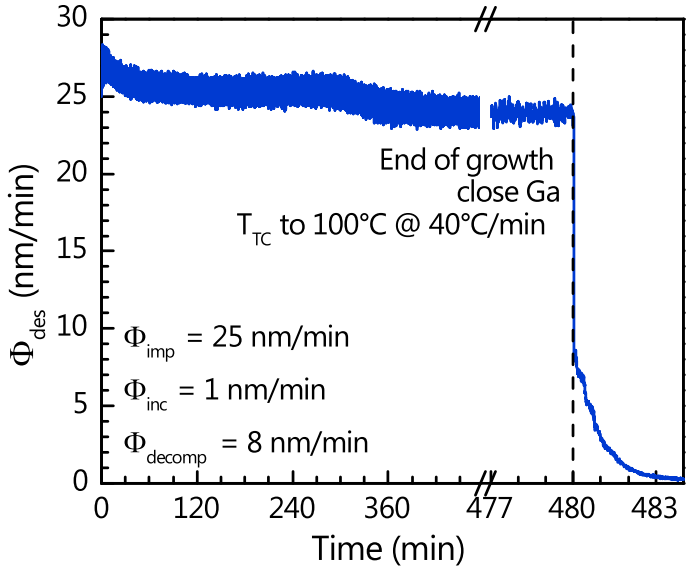

Figure 5.12: Desorbing Ga flux during high-temperature NW growth at 875°C obtained from QMS. At the end of growth, a significant Ga signal is measured even after the Ga shutter is closed.

In addition to indirectly observing GaN decomposition through radial growth, QMS measurements also provide direct evidence of NW decomposition. Figure 5.12 depicts the temporal evolution of the desorbing Ga flux Φ_{des} per unit area during the growth of sample S875. Here, the QMS signal is given without FFT filtering and not smoothened as described in Section 3.2.1 to achieve a better time resolution. After the completion of nucleation and height equilibration, Φ_{des} is as high as 96% of the impinging flux Φ_{inc}. For finishing the high-temperature growth of GaN NWs, the Ga shutter was closed. Then, the substrate temperature was immediately decreased to 100°C at 40°C/min with the N shutter kept open. Interestingly, significant Ga desorption is still measured after the Ga shutter is closed. This signal is attributed to decomposition. For the sample described above, the measured decomposition level Φ_{dec} is 8 nm/min. As the substrate temperature is decreased, also Φ_{dec} declines. We expect that the measured decomposition level in active N atmosphere does not significantly differ from the one during growth. Thus, we must acknowledge that GaN decomposition plays a significant role during NW growth at these temperatures. However, we must stress that Φ_{inc} and Φ_{dec} cannot be directly compared. While Ga incorporation during NW growth only takes place at the NW tip, decomposition may take place also on the NW sidewalls.

At this point, however, we must note that our hypothesis on the decomposition-induced radial growth presented here contradicts our model for the intentional thermal decomposition of GaN NWs that will be presented in the next chapter. There, we find the decomposition to proceed primarily in a layer-by-layer mode starting from the tip of the NW. A decomposition mechanism inducing radial growth as presumed here would have to start on the NW sidewall. The origin for this discrepancy may lie in the specifics of high-temperature NW growth (high impinging fluxes, significant Si incorporation) but are still not completely understood.

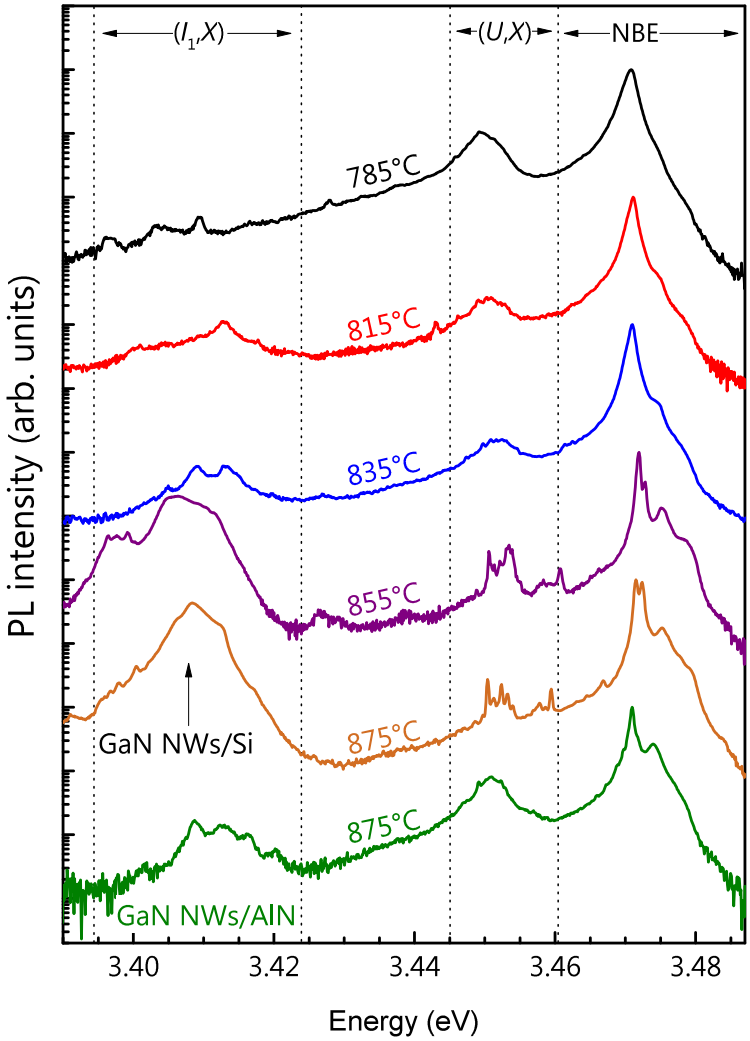

Figure 5.13: Normalized and vertically shifted PL spectra at 10 K of GaN NW ensembles grown on bare and AlN-buffered Si substrates at different temperatures. PL measurements carried out by Pierre Corfdir and Christian Hauswald.

5.1.3. Properties of GaN nanowires grown at high temperatures on Si

The results presented so far show that using non-conventional growth approaches, it is possible to synthesize GaN NWs at temperatures significantly higher than those previously reported in the literature.[37,38,74,133] The high-temperature growth of GaN NWs is, however, accompanied by Ga-induced melt-back etching of the Si substrate. In addition, for NWs exceeding 2.5 µm in length, radial growth is observed for NWs grown at temperatures above 850°C. The radial growth is believed to be caused by GaN decomposition. In the following, we examine the influence of the growth temperature on the optical properties of GaN NW ensembles by low-temperature (10 K) PL spectroscopy. Furthermore, the micro-strain present in the high-temperature NWs will be examined by XRD.

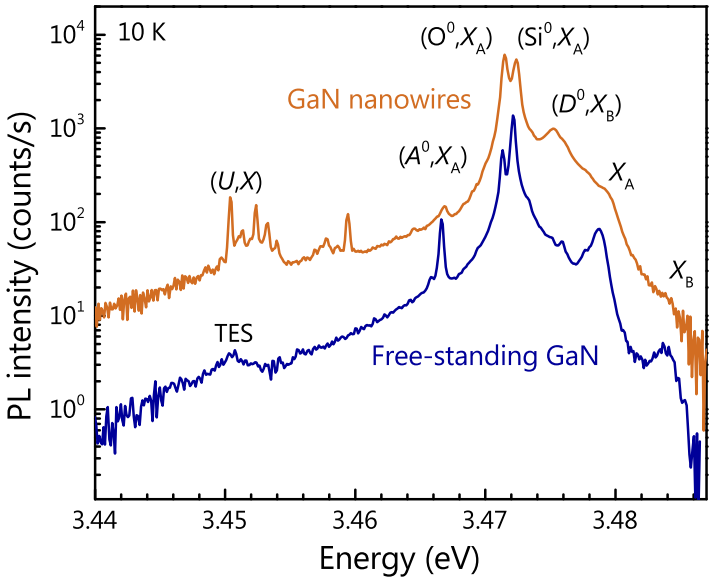

Figure 5.14: Comparison of GaN NWs grown on Si at 875°C with state-of-the-art FS-GaN (courtesy of Ke Xu and Hui Yang from the Suzhou Institute of Nano-Tech and Nano-Bionics). PL measurements carried out by Pierre Corfdir and Christian Hauswald.

Optical properties

Figure 5.13 shows the PL spectra at 10 K of GaN NW ensembles grown at different temperatures discussed in Section 5.1.1. As it was done for the morphological analysis, sample A875, grown on an AlN-buffered Si substrate, is discussed along the temperature series on bare Si.

Independent of the substrate temperature, the PL spectra of the NW ensembles are dominated by the donor-bound exciton transition (D^0, X_A) at 3.471 eV as is expected for a GaN crystal free of homogeneous strain.[81,146,147] For the samples grown at temperatures up to 835°C, this transition is accompanied by an exponential tail toward lower energies. Besides the (D^0, X_A) transition, we also observe in all samples the (U, X) transition[79,80] [recently attributed to inversion domain boundaries[148] and positioned at the same energy as the two-electron satellite (TES) peak in FS-GaN] as well as the (I_1, X) emission associated with the recombination of excitons bound to basal-plane stacking faults (SFs).[44,81,149,150] For the samples grown on bare Si, we found that the intensity of the SF-related luminescence monotonically increases with increasing substrate temperature.

For samples grown at 875°C, the (D^0, X_A) transition is sufficiently narrow that we can spectrally resolve the individual contributions of neutral O and Si donors, namely the (O^0, X_A) and (Si^0, X_A) transitions. Apart from these lines, we also observe the acceptor-bound exciton $[(A^0, X_A)]$ at lower energy and the donor-bound B exciton $[(D^0, X_B)]$ as well as the free-excitons (X_A, X_B) at higher energies. All these lines are easily resolved in this NW ensemble because the PL transitions become narrower with increasing substrate temperature. As shown in Fig. 5.15, the linewidth of the (O^0, X_A) transition for the NWs prepared on bare Si monotonically decreases from 2.2 to 0.5 meV when the substrate temperature is increased from 785 to 875°C. The linewidth for the sample grown at 875°C is thus much lower than the values reported in the literature for both undoped and doped

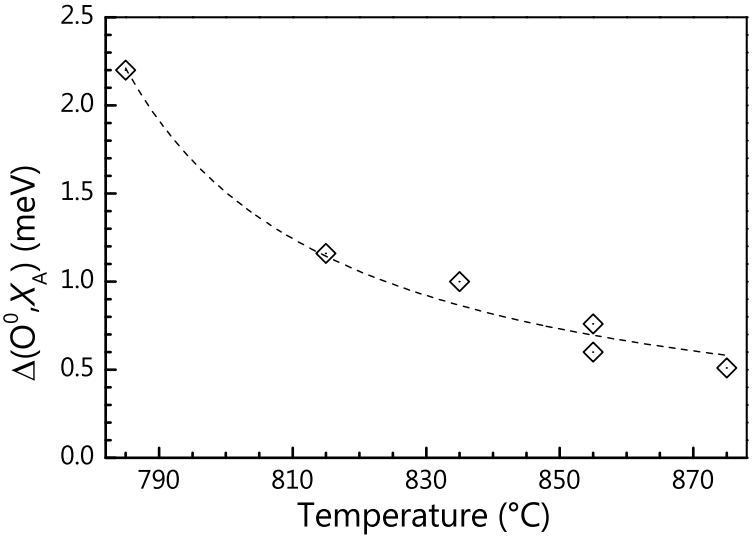

Figure 5.15: Variation in the linewidth of the (O^0, X_A) transition with the growth temperature for the GaN NW ensembles prepared on bare Si. The dashed black line is a guide to the eye. PL measurements carried out by Pierre Corfdir and Christian Hauswald.

GaN NW ensembles grown at lower temperatures ($1 - 3$ meV).[38,43,44,76,77,82,151,152]

For growth directly on Si, the narrowing of the PL lines with increasing substrate temperature is accompanied by a change in the intensity ratio between the (Si^0, X_A) and (O^0, X_A) transitions as shown in Fig. 5.13 and discussed in detail in Ref. [86]. Specifically, the higher the substrate temperature, the larger this ratio, indicating that Si incorporation occurs at higher temperatures. This Si incorporation is likely to originate from the melt-back etching of the substrate.[85] Since the presence of Si adatoms decreases the formation energy of basal plane SFs,[153] the melt-back etching may also explain the monotonic increase in the intensity of the (I_1, X) transition with substrate temperature.[85]

The linewidth of the excitonic transitions in GaN layers is determined by inhomogeneous strain induced by structural defects, in particular threading dislocations.[154] Single GaN NWs are free of threading dislocations, but the inadvertent coalescence of adjacent NWs may generate boundary dislocations which in term induce inhomogeneous strain.[57,76] In addition, the bound exciton transitions in NWs may also broaden due to the energy dispersion of these states resulting from their varying distances to the NW sidewall surfaces.[43,44] As detailed in Ref. [86], the moderate Si doping of the NWs induced by the melt-back etching of the Si substrate may lead to the ionization of surface donors and thereby diminish surface-induced broadening effects.

The explanation of a doping-mediated reduction of the surface-induced broadening is supported by the Ga series presented in Section 5.1.2. For sample S875b where the melt-back etching was even more pronounced, the linewidth of the (O^0, X_A) and (Si^0, X_A) transitions were again slightly narrow than for sample S875 (down to 0.4 meV for the (Si^0, X_A) transition). In contrast, the linewidth of sample T875b where the melt-back etching was almost entirely suppressed was again somewhat larger, namely 0.7 meV for the (O^0, X_A) while the (Si^0, X_A) exciton was not observed.

If the contribution of surface donors to the photoluminescence of our high-temperature GaN NW ensembles is indeed negligible, the PL spectra must reflect the structural per-

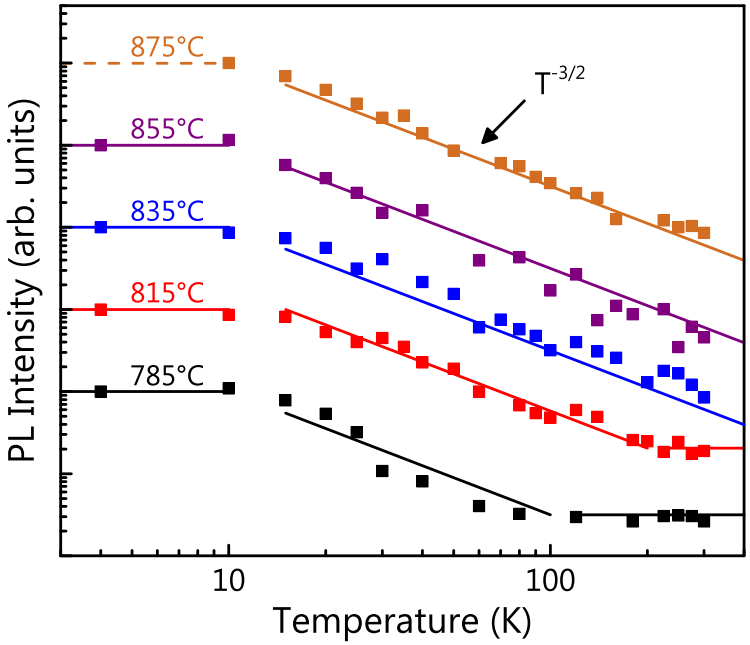

Figure 5.16: Temperature dependence of the integrated PL intensity of GaN NW ensembles grown on Si at different temperatures. PL measurements carried out by Pierre Corfdir and Christian Hauswald.

fection of the NW cores. Figure 5.14 displays the near band-edge (NBE) PL spectrum of sample S875 compared to that of a state-of-the-art 350 µm thick free-standing GaN (FS-GaN) layer grown by HVPE with a dislocation density lower than 10^6 cm^{-2}. The FS-GaN layer was courtesy of Ke Xu and Hui Yang from the Suzhou Institute of Nano-Tech and Nano-Bionics. We observe that both the energies and the linewidths of the bound- and free-exciton transitions of both samples are comparable. Therefore, despite the large lattice-mismatch between Si and GaN (17%), these $\approx$ 2 µm long GaN NWs are free of homogeneous strain and exhibit inhomogeneous strain in a similar magnitude as 350 µm thick FS-GaN layers. In addition, due to the enhanced light extraction efficiency for the NW morphology, we found that the integrated NBE PL intensity between 3.46 and 3.49 eV is one order of magnitude higher for the NW ensemble. Thus, the fabrication of GaN NWs at so far unexplored substrate temperatures along with the likely ionization of surface donors caused by unintentional Si doping have resulted in NW ensembles with unprecedented optical properties.

In addition to the spectral properties of the samples discussed above, we also investigated their temperature dependence as well as their dynamics. Figure 5.16 shows the temperature dependence of the PL intensities integrated over the (D^0, X) and FX transitions. The intensity decreases following a $T^{-3/2}$ dependence, demonstrating (i) that the dynamics of the FX and the (D^0, X) are dominated by nonradiative recombination already at cryogenic temperature, and (ii) that the decay rate of this nonradiative recombination channel is essentially constant over the whole temperature range since the radiative decay rate of the FX decreases with $T^{3/2}$.[85,87] Remarkable are the two samples prepared at the lowest temperatures (S785 and S815) where at some point, the intensity does not decrease further but stays constant (above 200 K and 100 K, respectively). At the moment, we cannot thoroughly explain this phenomenon. Our hypothesis is that we might deal with two kinds of NWs, one kind is dominated by nonradiative recombination while the other

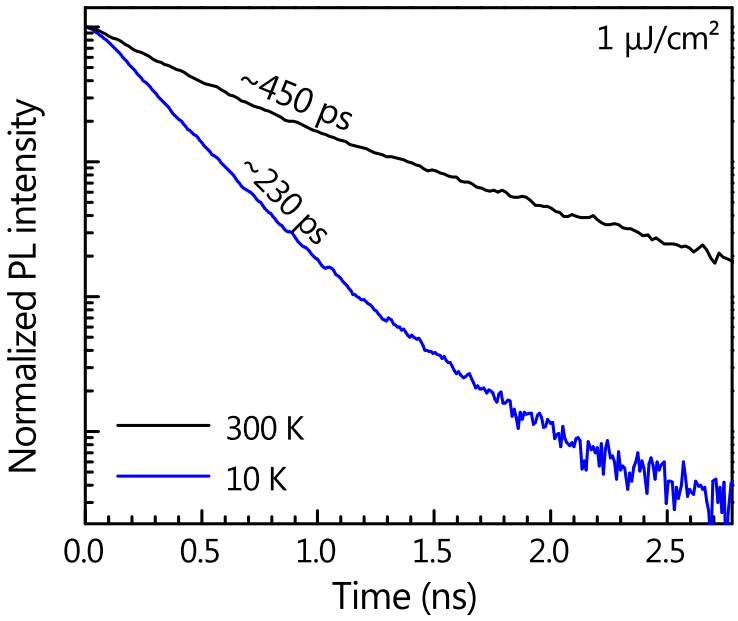

Figure 5.17: TRPL transient of GaN NWs grown at 875°C acquired at low and room temperature. PL measurements carried out by Pierre Corfdir and Christian Hauswald.

less frequent kind is purely radiative. Nevertheless, more experiments are required to completely understand this behavior.

Next, we studied the decay dynamics of the high-temperature NWs using time-resolved photoluminescence spectroscopy. In principle, exciton recombination in GaN NWs is assumed to be predominantly radiative owing to their high structural quality.[127] However, this expectation is inconsistent with the experimentally observed short decay times of bound excitons in GaN NWs. Even at low temperatures, TRPL measurements typically yield decay times in the range of a few tens to about 200 ps,[44,77,87,155–159] i.e., significantly shorter than the radiative lifetime of the bound exciton state in bulk GaN of at least 1 ns.[128,129] Recently, we have shown that the exciton lifetime in the GaN NW ensembles is limited by nonradiative recombination.[87] The lifetime is independent of the ensembles mean surface-to-volume ratio and coalescence degree, implying that the nonradiative process is neither caused by surface recombination nor by dislocations formed due to NW coalescence.[87] The remaining possibility for the origin of this nonradiative channel are point defects.[87] As we discussed in Section 3.3.1, the limited kinetics in GaN growth in MBE, owing to the inherent temperature limitations, result in a comparably high concentration of point defects. Simultaneously, given that the diffusion length of free excitons in GaN is larger than 50 nm, a defect density as low as 10^{15} cm^{-3} may suffice to introduce an effective nonradiative decay channel via the free exciton state.[87]

Figure 5.17 depicts the TRPL transient of sample S875, GaN NWs prepared at 875°C on Si. At cryogenic temperatures, the (D^0, X_A)decays with an effective decay time of $\tau_{eff} = 230 \pm 10$ ps. At room temperature, an effective decay time of $\tau_{eff} = 450 \pm 20$ ps is measured for the free exciton. While these values are at the upper limit to what is typically measured for GaN NWs,[44,77,87,155–159] they are still far from the decay times found in bulk GaN.[128,129]

Figure 5.18 summarizes the effective lifetimes obtained at 10 K for the temperature series. The sample grown at 835°C was measured twice in two different measurement

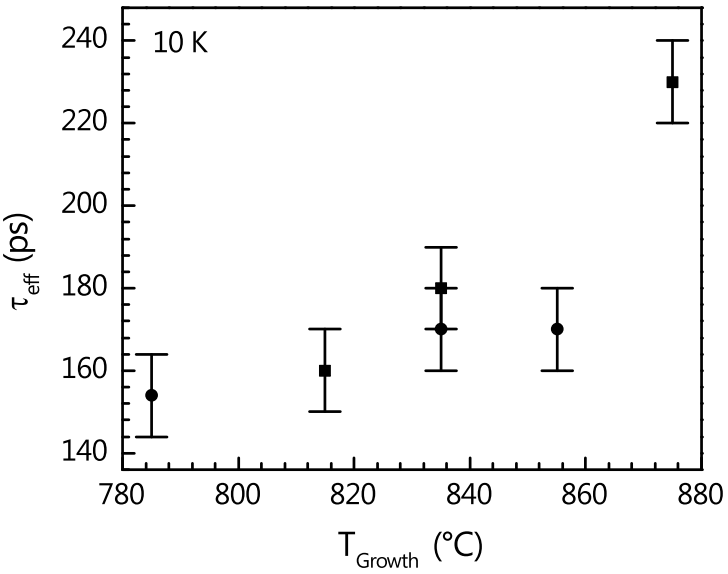

Figure 5.18: Effective lifetime τ_{eff} obtained at 10 K for GaN NW ensembles grown at different temperatures. PL measurements carried out by Pierre Corfdir and Christian Hauswald.

sessions with slightly varying results. In general, no clear temperature dependence can be identified. The sample prepared at 875°C seems to stand out of the series. It must be mentioned, however, that additional TRPL measurement on these samples by Daniel Kage yielded that the measured effective lifetime depends strongly on the time (in days) the samples have been stored in UHV conditions.[160] The observed effect behaved differently than the desorption of oxygen from the NW sidewalls reported by Pfüller et al.[79] In addition to the potential influence of the growth temperature on the density of point defects, the ionization of surface donors through the moderate Si doping may also change the electron-hole overlap in the NWs and thereby influence the exciton decay.[45]

Summarizing, the decay of high-temperature GaN NWs remains predominantly nonradiative. A significant impact of the growth temperature on the effective decay time is not observed. As only few point defects are required in a NW to introduce an effective nonradiative decay channel via the free state,[87] the increase in growth temperature up to 875°C may simply be not high enough to substantially decrease the density of point defects. The NBE PL spectra of those NW ensembles prepared at elevated substrate temperatures, however, are comparable to that of state-of-the-art FS-GaN and exhibit excitonic transitions with linewidths below 500 µeV.

Inhomogeneous strain

As stated earlier, the linewidth of the excitonic transitions in GaN layers is determined by inhomogeneous strain.[154] In NWs, this strain-induced broadening is superimposed by the broadening induced by the distribution of donors in the NWs and their varying distance to the NW sidewall surfaces.[43,44] As we believe the latter effect to be diminished in our high-temperature NW samples, an investigation of the inhomogeneous strain present in the same is highly interesting.

Single spontaneously formed GaN NWs are initially single crystalline and free of homogeneous strain.[37,38,76,77,117] Nevertheless, spontaneously formed GaN NW ensembles

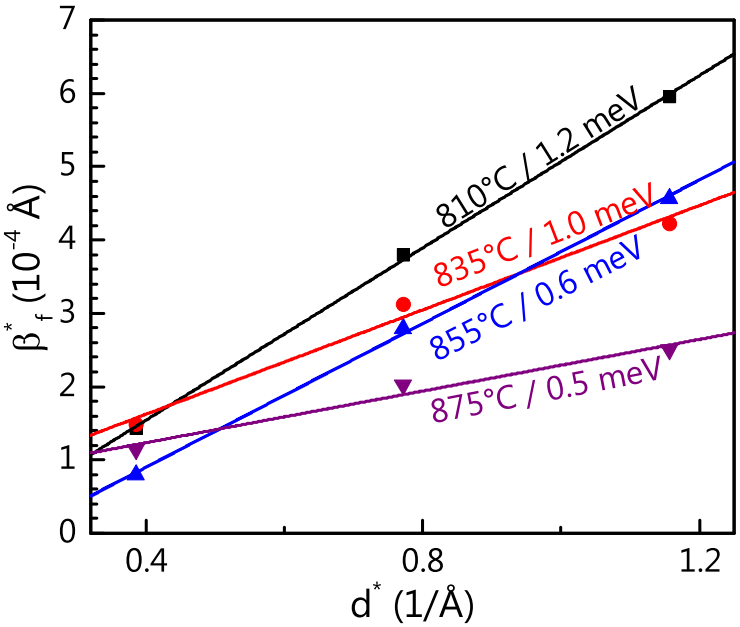

Figure 5.19: Williamson-Hall plot for GaN NW ensembles grown on Si at different temperatures. Along with the linear fits, the growth temperatures as well as the (D^0, X_A) linewidths measured by PL spectroscopy are given.

often exhibit a high degree of coalescence[56,71,73,75,95,111,161] accompanied by inhomogeneous strain on a microscopic scale, so-called micro-strain.[69,70] Both, random distortions at the interface between the substrate and the NWs,[70] and strain induced by coalescence boundaries[69,70] have been suggested as the origin for the inhomogeneous measured in XRD. Recently, a correlation between the structural and optical properties of spontaneously formed GaN NWs has quantitatively evaluated the impact of NW coalescence on the presence of inhomogeneous strain.[76] From the comparison of the properties of multiple samples grown directly on Si and AlN buffer layers, it was concluded that (i) the inhomogeneous strain detected by XRD in NW ensembles is mainly caused by the coalescence of closely spaced NWs, (ii) the magnitude of the coalescence-induced strain inhomogeneity depends on both the coalescence degree and the mutual misorientation of adjacent NWs, and (iii) the linewidth of the excitonic transitions observed by PL spectroscopy does not exhibit a monotonic increase with the coalescence degree but scales with the rms strain.[76]

The strain state of the high-temperature GaN NW ensembles was determined from $\theta/2\theta$ scans along the 0002, 0004, and 0006 reflections in XRD. Figure 5.19 depicts Williamson-Hall plots in the reciprocal space representation for the GaN NW temperature series grown directly on Si. The magnitude of the micro-strain ε is obtained from the slope of the linear fits. Along with the linear fits, the growth temperatures as well as the (D^0, X_A) linewidths measured by PL spectroscopy are given. At a first glance, the sample grown at 855°C contradicts the observation in Ref. [76] according to which the excitonic linewidth monotonically increases with ε. For the other three samples measured, the observation holds up.

Before further discussing this discrepancy, we want to put our result in the context of previously published results in the inhomogeneous strain in spontaneously formed GaN

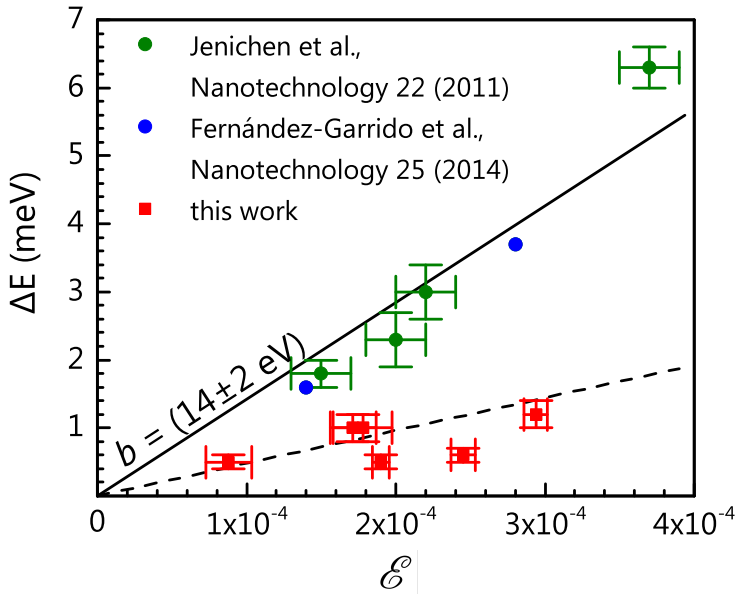

Figure 5.20: Linewidth of the (D^0, X_A) transition as a function of the micro-strain obtained for GaN NW ensembles grown on Si at different temperatures (red squares). We also include values reported in literature.

NW ensembles. Figure 5.20 presents the linewidth of the (D^0, X_A) transition as a function of ε for various samples from the temperature and Ga series presented in Sections 5.1.1 and 5.1.2, respectively. In addition, the values reported in Refs. [69] and [76] are given. In Ref. [76] the relation of excitonic linewidth and strain values is found to be best described by a slope of $b = 14 \pm 2$ eV. This result is close to the value of 16.5 eV expected for pure biaxial strain.[162] Clearly, the relation of excitonic linewidth and strain values obtained for our samples, high-temperature as well as conventional growth temperatures, contradicts the previously reported data. Despite the record low excitonic transitions, the values we obtain for the micro-strain are rather comparable to previous reports. Only our best sample, grown at 875°C and not suffering from radial growth, exhibits a micro-strain of only about 2/3 of the lowest previously reported value.

At this point, we must discuss the differences of the NWs ensembles used in this work and those in the cited references. All of our NW ensemble measured here are comparatively long, i.e., longer than 2.2 µm. In contrast, the NW ensembles discussed in Refs. [69] and [76] are only about 1 µm long. X-ray diffraction and PL spectroscopy exhibit different sensitivities to the film thickness, or in our case, the average NW length. While XRD usually probes the entire structure, the PL measurement depends on the penetration depth of the laser excitation. The exact absorption profile of spontaneously formed GaN NWs is rather difficult to determine. In general, it depends on the average NW diameter as well as the NW number density. It is presumed, however, that PL spectroscopy probes only the upper few hundred nms to a micron of the NW ensemble. Furthermore, it has been reported previously, the ε decreases very quickly with NW length.[70]

The samples measured in this work divide into two classes. The samples where the conventional NW morphology was maintained, i.e., no radial growth was observed, are all close to 2.4 µm long. For these samples, the linewidth of the excitonic transitions still monotonically increases with ε. The different measurement sensitivities of XRD and

PL spectroscopy lead to a lower slope as indicated by the dashed line in Figure 5.20. In contrast, the samples where radial growth is observed, exhibit even lower linewidth in relation to their actual strain state. Here, the radial growth seems to induce additional inhomogeneous strain. The measured PL signal, however, will predominately originate from the thick part on top, that then may fully profit from the improved structural quality as well as the diminishing of the surface induced broadening. For all high-temperature NW samples, however, the inhomogeneous strain present is not significantly lower than in previous reports.

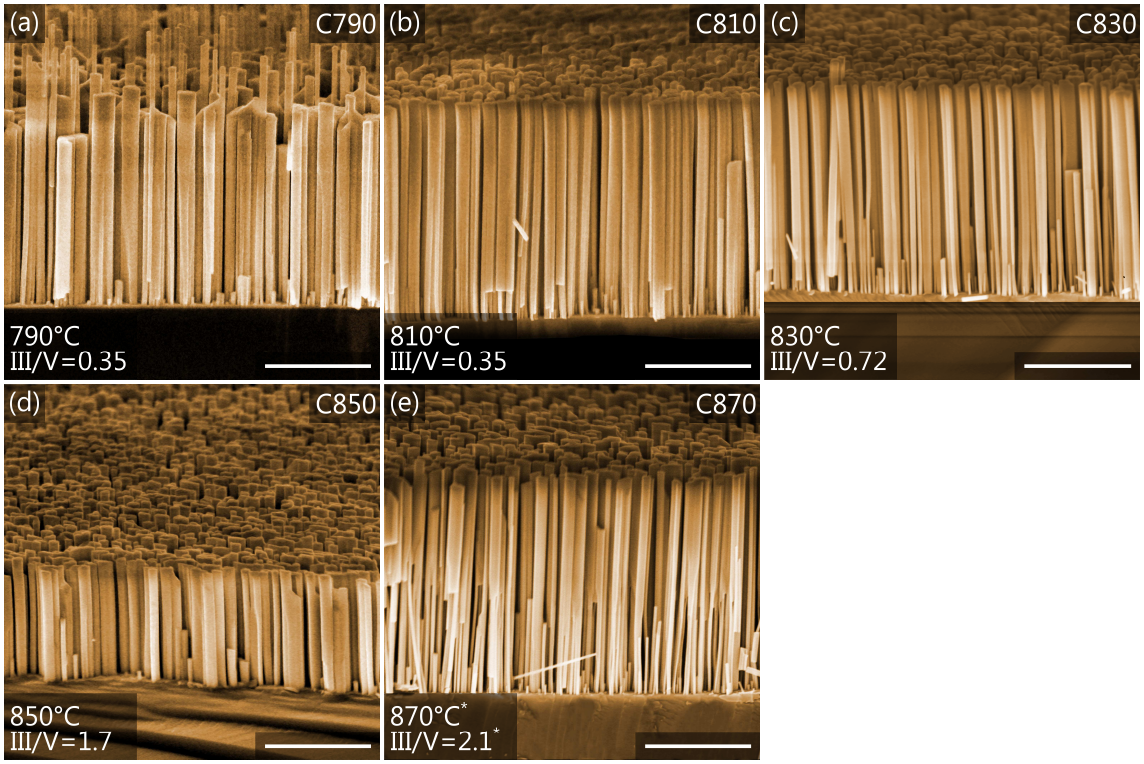

Figure 5.21: Scanning electron micrographs of GaN NW ensembles grown on SiC(000$\bar{1}$) at different temperatures. The scale bars correspond to 1 µm. SEM measurements carried out by Anne-Kathrin Blum.

5.2. Growth of GaN nanowires on 6H-SiC(000$\bar{1}$)

Owing to the nature of the melt-back etching, the moderate Si doping in the last section remained unintentional. Therefore, in this section, we attempt to separate the effects of growth temperature and Si doping by growing in an alternative substrate where melt-back etching is not expected, namely SiC, and later on by intentionally doping the NW ensembles using Si. Thus, we aim to clarify our theory that the narrow excitonic transitions discussed are a result of a moderate Si doping.

5.2.1. Growth of GaN nanowires on SiC at different temperatures

An ideal substrate for the conceived experiments would be entirely Si-free. Potential candidates as substrates where unintentional Si doping due to melt-back etching is impossible are diamond, titanium or amorphous sapphire.[39–41] However due to issues of availability, for our experiments, SiC(000$\bar{1}$) was chosen. SiC is known to be stable against temperature up to 1400°C, therefore, a melt-back etching reaction comparable to Si(111) was not expected.

To our knowledge, no spontaneous formation of GaN NWs has been reported directly on SiC in MBE. However, N-polar NWs have been found to nucleate on AlN-buffered SiC(000$\bar{1}$).[120] Therefore, NW nucleation directly on SiC(000$\bar{1}$) seems quite likely, as it serves both potential prerequisites discussed in Section 3.3, i.e., lattice mismatch and polarity.

Figure 5.21 depicts scanning electron micrographs of GaN NW ensembles grown directly

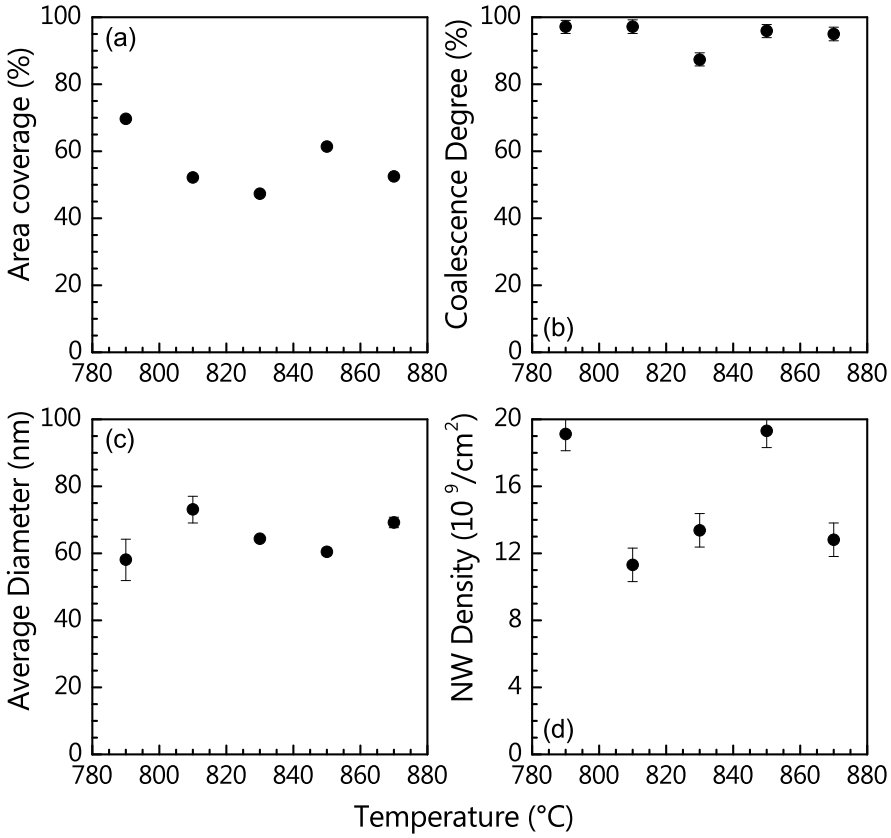

Figure 5.22: NW ensemble properties as obtained from statistical shape analysis. While the NW diameters [(c)] are comparable to those obtained on Si, the total NW number density [(d)] and thereby the area coverage [(a)] is significantly higher. Therefore, also the coalescence degree [(b)] remains high. Due to the varying experimental growth conditions, no clear temperature dependence is observed.

on SiC(000$\bar{1}$) at different temperatures. The temperature and Ga flux were varied in range comparable to the series on Si(111). The growth time of all samples was 315 min. However, due to various experimental difficulties described below, the resulting NW ensembles cannot be directly compared to those prepared on Si(111).

The measurement of the desorbing Ga flux Φ_{des} was not possible due to the limited size of the sample. Also, the plasma source had to be exchanged midway through the series. Therefore, samples C790, C810, and C830 were grown with $\Phi_{\mathrm{N}} = 11.0 \pm 0.5$ nm/min and C850 and C870, as well as D850a and D850b introduced later, with $\Phi_{\mathrm{N}} = 7.8 \pm 0.5$ nm/min. Simultaneously, for the same group of samples, also the substrate rotation malfunctioned. Without operating substrate rotation, RHEED measurements were often impossible due to the misalignment of the substrate.

Figure 5.22 presents the area coverage, coalescence degree, average uncoalesced diameter, and total NW number density for the given temperature series prepared on SiC(000$\bar{1}$) as obtained from statistical shape analysis. While a detailed analysis is not possible due to the varying experimental conditions described above, general observations can be made to identify the differences to NW growth on Si(111). In principle, it was found that the incubation time is much shorter on SiC[000$\bar{1}$] for comparable growth conditions. For samples C790 and C810, the nucleation of the first NWs was observed in RHEED within less

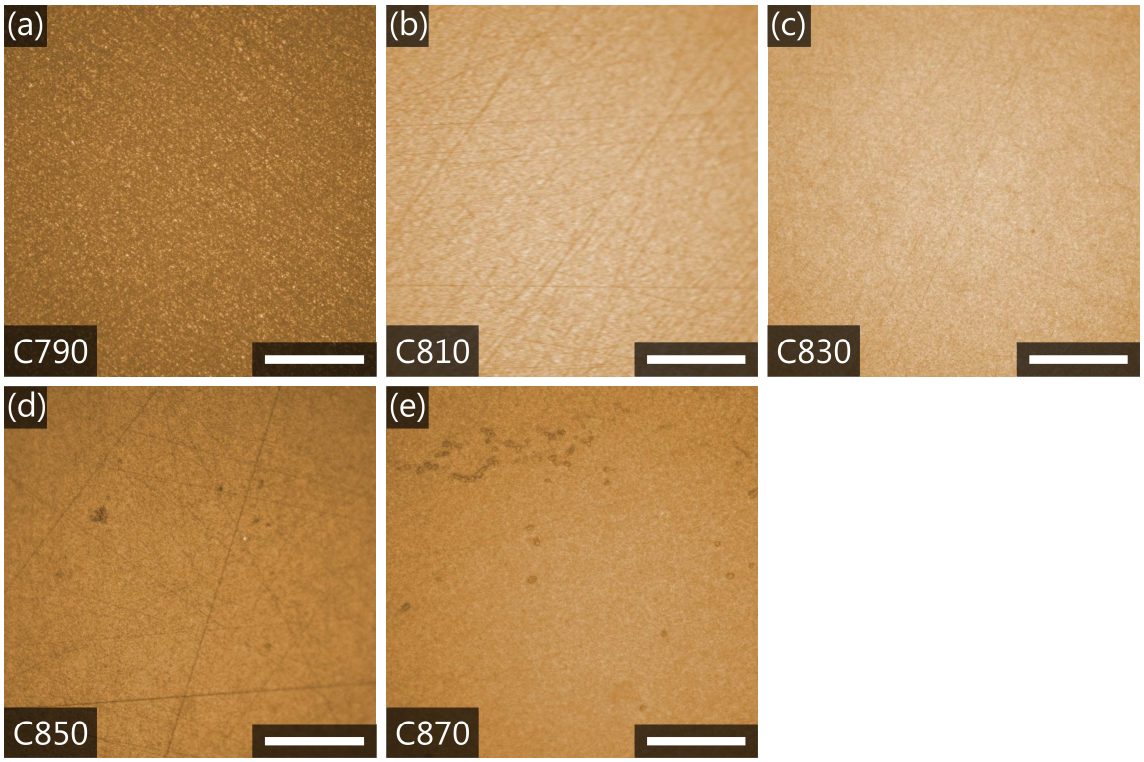

Figure 5.23: Optical micrographs of GaN NW ensembles grown on SiC at different substrate temperatures. For temperatures above 850°C, some grey spots are observed.

than two minutes. Due to the lack of good RHEED measurement, a good quantification of the incubation time was not possible for all samples of the series. However, a clear increase in the incubation time with substrate temperature was evident. As it was the case on Si(111), the increase in Φ_{Ga} only partially compensated for the higher Ga adatom desorption during the incubation stage. At the highest substrate temperature of 870°C, the introduction of a low-temperature nucleation step was required to obtain a dense array of NWs within the given growth time.

The NW ensembles on SiC(000$\bar{1}$) exhibit significantly higher area coverages (roughly factor 2) than observed on Si(111) within the whole substrate temperature range used. As the average uncoalesced NW diameter remains comparable to the values obtained in Chapter 5.1.1, the difference originates in the significantly higher number density that is observed on SiC(000$\bar{1}$). According to [67], this points towards a lower diffusion length of GaN on SiC compared to Si. However, also a faster nucleation rate in combination with shadowing effects can explain this observation. The varying experimental conditions prevent a verification of a decrease in number density with growth temperature (accompanied by a decrease in area coverage and thereby coalescence degree) as observed on Si(111). Due to the lower Φ_N used for the samples C850 and C870, these two samples cannot be compared to those grown at lower temperatures. However, regarding only the lower three substrate temperatures, a similar behavior with temperature seems likely.

Figure 5.23 depicts the plan-view optical micrographs corresponding to the scanning electron micrographs presented in Fig. 5.21. The NW ensembles grown at lower temperatures exhibit the typical noisy pattern expected for NWs. In addition, straight scratch marks induced by wafer polishing are visible. For growth temperatures above 850°C, a

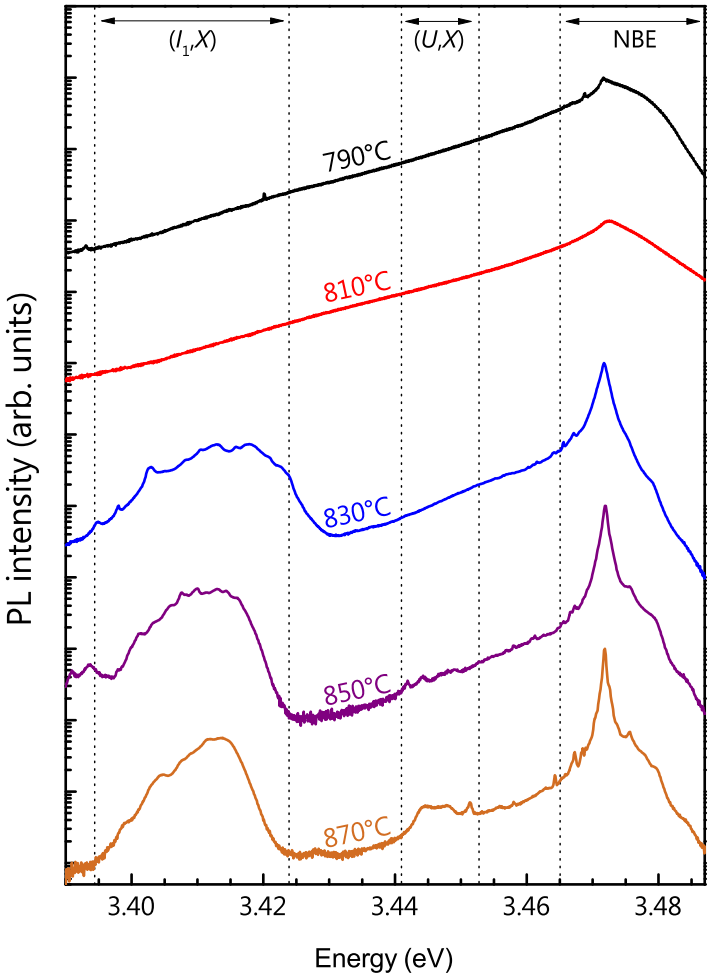

Figure 5.24: Normalized and vertically shifted PL spectra at 10 K of GaN NW ensembles grown on SiC(000$\bar{1}$) at different temperatures. PL measurements carried out by Pierre Corfdir.

few grey spots comparable to those induced by Si melt-back etching on Si(111) appear. They usually lie in direct proximity of the scratch marks. In SEM, however, no evidence of a melt-back etching process into the substrate was found. Nevertheless, a certain amount of Si may be present on the surface close to the scratch marks due to the wafer polishing. The potential unintentional presence of Si for NW growth on SiC(000$\bar{1}$) will be further discussed below.

5.2.2. Properties of GaN nanowires grown on SiC

Figure 5.24 depicts the low-temperature PL spectra of the GaN NW series discussed above. The NWs prepared at 790°C and 810°C exhibit very broad spectra centered at the (D^0, X_A) exciton transition energy. This linewidth is larger than what is expected for these growth temperatures based upon the results from the growth on Si(111). For the NWs grown at higher temperatures, a clear reduction of the linewidth of the (D^0, X_A) exciton transition is observed as illustrated in Figure 5.25. Simultaneously, a pronounced stacking fault emission is appearing around 3.41 eV. For sample C870 grown at 870°C, the linewidth

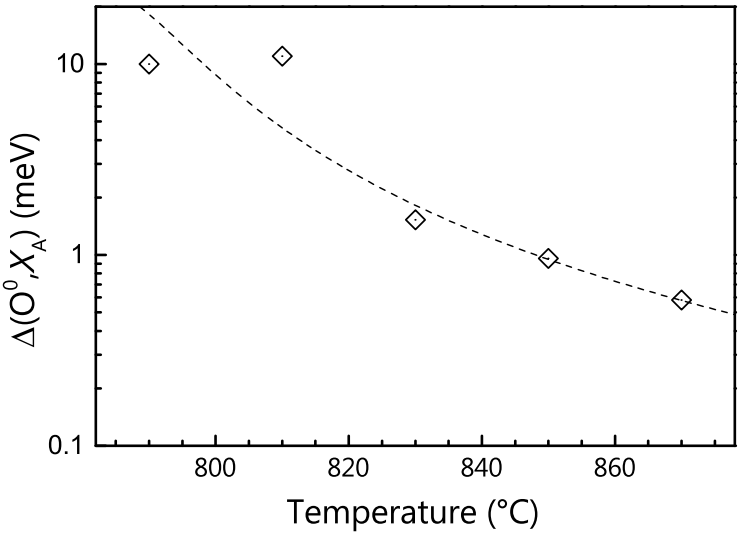

Figure 5.25: Variation in the linewidth of the (O^0, X_A) transition with the growth temperature for GaN NW ensembles prepared on SiC(000$\bar{1}$). The dashed black line is a guide to the eye. PL measurements carried out by Pierre Corfdir.

of the (D^0, X_A) exciton transition is as low as 0.6 eV. In contrast to the samples prepared on Si(111), no pronounced (Si^0, X_A) is observed. However, at least for sample C850, a shoulder at the corresponding energy of 3.472 eV points toward some Si incorporation (Figure 5.24).

The observed decrease in linewidth is comparable to that observed for growth on Si(111) despite significantly lower Si incorporation levels. However, both the optical micrographs and the PL spectra suggest that SiC reacts during growth and this may induce unintentional Si doping. According to our calculations,[86] doping levels as low as 5×10^{16} atoms/cm^2, i.e., only slightly above the typical background doping level, are sufficient to ionize surface donors in GaN NWs. Thus, the few present Si atoms may already provoke the doping-mediated reduction of the surface induced broadening discussed in Section 5.1.3. Before we study the influence of intentional Si doping on these NW ensembles, we will briefly discuss the structural properties of the GaN NWs presented above.

Figure 5.26 illustrate the improved epitaxial alignment of GaN NWs on SiC(000$\bar{1}$) compared to Si(111). The presented x-ray diffraction scans were recorded on the sample S875 and C870, prepared at around 870°C. However, the epitaxial alignment is not affected by the growth temperature and the comparison is therefore valid for the whole temperature range. The sample prepared on Si exhibits typical twist and tilt values between 3 and 4 degrees.[69,70,76] In contrast, the determined average NW tilt and twist on SiC(000$\bar{1}$) range between 0.4 and 0.6 degrees and 1.5 and 2.1 degrees, respectively. These values are in good agreement with reports of GaN NWs prepared on AlN-buffered SiC(000$\bar{1}$).[76]

Generally, one might think the better epitaxial alignment in these NWs on SiC(000$\bar{1}$) results in lower values of inhomogeneous strain compared to NWs on Si(111). However, as the number density and thereby the area coverage also significantly increases, the relative volume affected by NW coalescence is much higher. Thus, neither the coalescence degree nor the NW tilt and twist by themselves are sufficient to estimate the resulting inhomogeneous strain.[76]

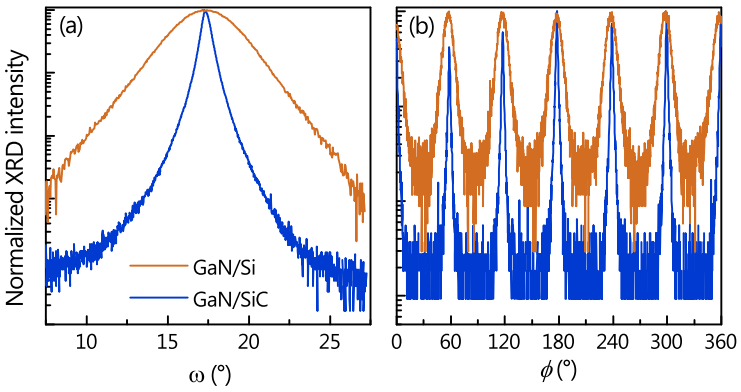

Figure 5.26: (a) X-ray diffraction scans of GaN NW ensembles on Si(111) and SiC(000$\bar{1}$) across the 0002 reflection measured along ω. (b) Azimuthal ϕ scan across the 10$\bar{1}$5 reflection in skew geometry.

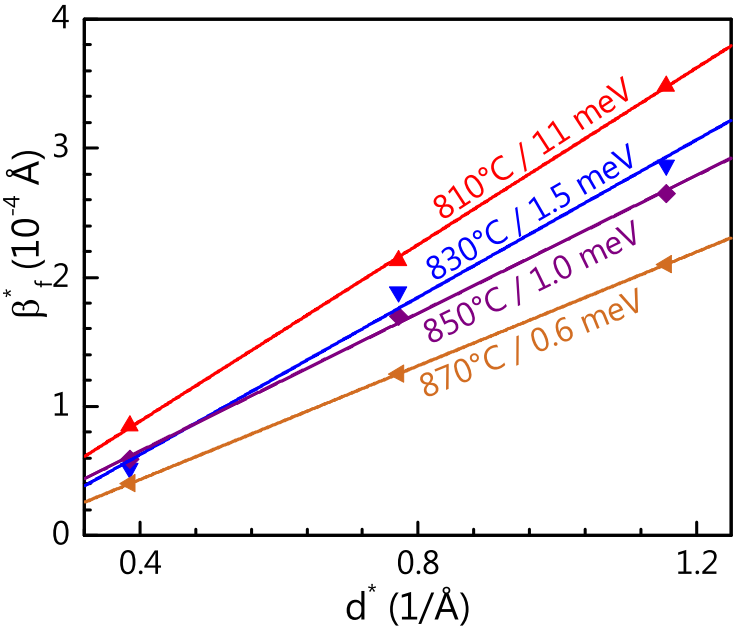

Figure 5.27: Williamson-Hall plot for GaN NW ensembles grown on SiC(000$\bar{1}$) at different temperatures.

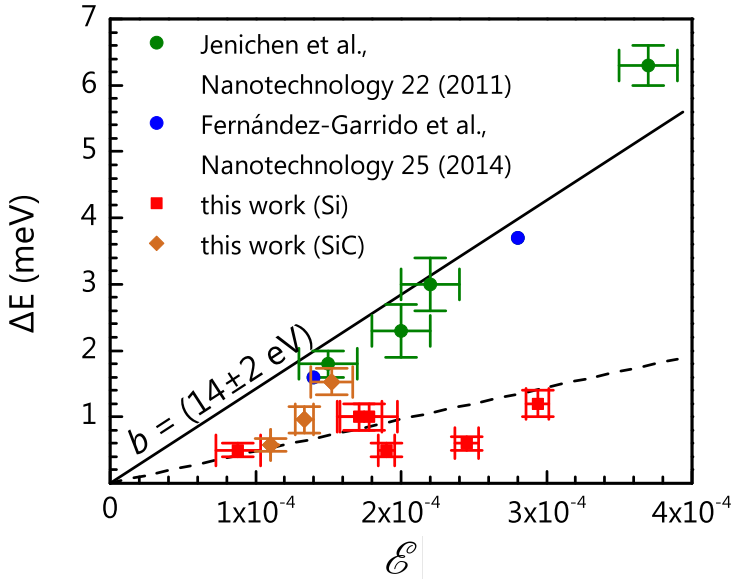

Figure 5.28: Linewidth of the (D^0, X_A) transition as a function of the micro-strain ε obtained for GaN NW ensembles grown on SiC(000$\bar{1}$) at different temperatures and compared to values reported in literature.

Figure 5.27 shows the Williamson-Hall plots for the GaN ensembles prepared on SiC. In contrast to the series on Si (compare Fig. 5.19), a monotonous dependence of the slope, i.e., the inhomogeneous strain, on the growth temperature and thereby the linewidth of the (D^0, X_A) transition is observed. The reason is that the NW ensembles on SiC(000$\bar{1}$) remained sufficiently short such that no radial growth was occurring during high-temperature NW growth. Interestingly, the variation in the coalescence degree seems to have a lower effect on the inhomogeneous strain than the growth temperature.

In Figure 5.28, a comparison of the inhomogeneous strain of these samples to the values reported in literature and those in Section 5.1.3 is given for sake of completeness. The obtained values spread between the reported literature values from shorter NWs and the series on Si(111) where the GaN NWs were generally longer. In addition, also the area coverage and NW diameters influence the photoexcitation during the PL measurements. Thus, again, XRD and PL may be probing different volumes. Nevertheless, we can conclude that the high-temperature GaN NW ensembles grown on SiC(000$\bar{1}$) exhibit a very low degree of inhomogeneous strain, comparable to the samples prepared on Si(111) at similar temperatures. Furthermore, the inhomogeneous strain decreases with the growth temperature. Thus, also the contribution of the inhomogeneous strain to the broadening of the (D^0, X_A) exciton transition should decrease.

5.2.3. Silicon doping of high temperature GaN NWs on SiC

The original idea behind the growth of GaN NWs on SiC(000$\bar{1}$) was to separate the influences of substrate temperature and Si incorporation on the linewidth of the NW ensemble. Unfortunately, as discussed above, there are reasons to believe some Si incorporation is already present without intentional Si doping. These low Si incorporation levels may be sufficient to ionize surface donors in NWs and thereby reduce their broadening effects.[86]

In this section, we present the results of intentionally doped GaN NWs grown on

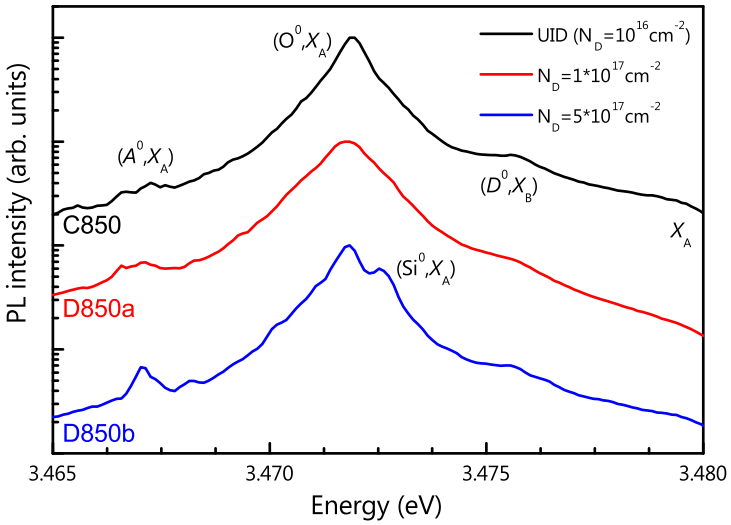

Figure 5.29: Low-temperature NBE PL spectra of GaN NW ensembles grown on SiC(000$\bar{1}$) at 850°C with different Si doping levels. PL measurements carried out by Pierre Corfdir.

SiC(000$\bar{1}$) at 850°C. According to our calculations,[86] moderate doping levels between 1×10^{16} and 5×10^{17} atoms/cm^2 are sufficient to ionize surface donors in GaN NWs. Therefore, two samples were prepared with targeted densities of 1×10^{17} (D850a) and 5×10^{17} atoms/cm^2 (D850b). The samples were then compared to the nominally undoped sample C850, where a background concentration of 1×10^{16} atoms/cm^2 is assumed. For doping concentrations higher than 10^{18}, the NWs become depleted and their luminescence broadens again.[86]

Figure 5.29 presents the low-temperature NBE PL spectra of those three samples. With increasing nominal Si incorporation, the $(\mathrm{Si}^0, X_\mathrm{A})$ peak appears as a shoulder on the high-energy side of the $(\mathrm{O}^0, X_\mathrm{A})$ peak. At 5×10^{17} atoms/cm^2, the relative intensity of the $(\mathrm{Si}^0, X_\mathrm{A})$ to the $(\mathrm{O}^0, X_\mathrm{A})$ exciton transition is comparable to the sample grown on Si(111) at a similar substrate temperature (S855). Simultaneously, the linewidth of the $(\mathrm{O}^0, X_\mathrm{A})$ transition of that sample has decreased from 1.0 to 0.85 meV. However, for the low doping sample, the linewidth is slightly larger than for the undoped sample, namely 1.1 meV. Unfortunately, at this point it cannot be distinguished whether the change in linewidth is actually induced by the intentional Si doping or it is a result of the limited reproducibility of the NW ensembles in terms of substrate temperature due to the experimental conditions at that time. As the linewidth of the undoped sample was already quite low, the potential improvement achievable by the intentional Si-doping was limited. However, due to the experimental difficulties with the MBE machine mentioned above, a repetition of the doping experiments was not possible within the time frame of this thesis. In order to unambiguously distinguish the influences of Si incorporation and substrate temperature, these experiments will have to be repeated instead on truly Si-free substrates. These experiments will be conducted at our institute outside of the framework of this thesis, most likely on sputtered Al_2O_3.

5.3. Summary and conclusion

In summary, we have introduced three different growth approaches to enhance nucleation and reduce the incubation time preceding the spontaneous formation of GaN NWs on Si(111). We achieve this by either using (i) nominally Ga-rich growth conditions, (ii) a low-temperature nucleation step, or (iii) an AlN buffer-layer. All three approaches enable the spontaneous formation of NWs at so far unexplored substrate temperatures. We demonstrate NW growth up to 905°C. However, substrate temperatures above 850°C result in unintentional Si incorporation originating from the melt-back etching of the Si substrate. The NBE photoluminescence spectra of the nanowire ensembles prepared at elevated substrate temperatures are comparable to that of state-of-the-art free-standing GaN layers and exhibit excitonic transitions with linewidths below 500 µeV. In contrast, high-temperature growth of GaN NWs does not significantly improve their recombination dynamics. If point defects are the origin for the strong nonradiative recombination observed in GaN NWs, the achieved increase in growth temperature was not sufficient to significantly lower their density. The inhomogeneous strain present in the high-temperature NWs is not significantly lower than in previous reports. The high-temperature growth of GaN NWs on 6H-SiC(000$\bar{1}$) resulted in comparable results, because a reaction with the substrate also was not entirely prevented on SiC. Nevertheless, our results demonstrate that NW growth at elevated temperatures along with unintentional Si doping facilitates the fabrication of GaN NW ensembles with optical properties not observed before in GaN grown by MBE on Si. The samples obtained here have led to several additional investigations and publications examining their linewidth[86], stacking fault luminescence[85], and polarization.[78]

6. Fabrication of ultrathin GaN nanowires by thermal decomposition

Spontaneously formed GaN NW ensembles usually exhibit diameters above 30 nm. The lowest NW diameters reported for longer NWs were about 15 nms and the thinnest NWs observed directly after shape transition already have diameters above 10 nms.[54,74,111,112] Thus, the critical diameter of 10 nms for the shape transition represents an intrinsic lower limit for the direct growth of spontaneously formed NWs. In order to achieve excitonic confinement in GaN NWs, even thinner diameters are desirable. When growing GaN NWs at high temperatures in Chapter 5, we observed the onset of NW decomposition at high substrate temperatures. In this Chapter, we will study and utilize the decomposition of GaN NWs to reduce the diameters of grown NW ensembles and thus fabricate NWs of exceptionally low diameters (as small as 6 nm). We will demonstrate that these ultrathin NWs exhibit unprecedented excitonic properties evoked not by quantum but dielectric confinement.

In 1979, Keldysh demonstrated that excitonic phenomena in semiconductors can be dramatically enhanced by combining materials with significantly different dielectric constants (or, in modern terms, relative permittivities).[163] If the dielectric constant of the semiconductor is larger than that of the surrounding material, the redistribution of the polarization field caused by the dielectric mismatch at the interfaces results in an enhancement of the Coulomb interaction between free electrons and free holes. This effect, denoted as the dielectric confinement of the exciton, gives rise to a greatly increased exciton binding energy and oscillator strength[164–167] and is thus interesting for room temperature optoelectronic applications involving excitons[168–172] such as polariton lasers[168] or excitonic switches.[169]

The strongest dielectric confinement possible is realized in semiconductor nanostructures surrounded by a material with a dielectric constant of 1, i. e., vacuum or air.[173] However, the unpassivated surfaces of semiconductors are believed to invariably suffer from efficient surface recombination, rendering such structures unsuitable for optoelectronic devices. For instance, the surface recombination velocity at the sidewalls of GaAs nanowires is on the order of 5×10^5 cm s^{-1}.[174] As a result, GaAs nanowires with diameters below 100 nm do not emit any light at all.[175] Passivating the surface of GaAs nanowires with an (Al,Ga)As shell reduces the surface recombination velocity by orders of magnitude,[176] but at the same time also the dielectric mismatch. Consequently, the impact of the dielectric confinement on the exciton in semiconductor heterostructures is negligible.[177] ZnO nanowires exhibit intense excitonic emission at room temperature,[178] but the dielectric constant of ZnO is too small to give rise to a strong dielectric confinement. Stronger dielectric confinement of the exciton may, in principle, be obtained in hybrid structures combining insulating and semiconducting materials,[179] but the incompatible crystal structures are expected to lead to a high density of interface states and thus high interface recombination velocities.

In this context, GaN nanowires appear to be a more suitable platform for optoelectronic applications based on dielectrically enhanced excitons. GaN, the compound semiconduc-

tor that enables solid-state lighting,[180] is also a promising material for excitonics because the exciton binding energy is equal to $k_B T$ at room temperature already in the bulk. GaN nanowires form spontaneously on a wide variety of substrates and are free of homogeneous strain and threading dislocations.[66] In addition, the dangling bond states for GaN polar and nonpolar surfaces are located far from midgap[181] so that surface recombination is expected to be comparatively inefficient. In fact, a surface recombination velocity as low as 210 $\mathrm{cm\,s^{-1}}$ was reported recently for unpassivated GaN nanowires,[86] a value three orders of magnitude smaller than that measured for GaAs nanowires[174] and comparable to the interface recombination velocity in GaAs/(Al,Ga)As double heterostructures grown by molecular beam epitaxy.[182]

Here, we report on room temperature luminescence from dense ensembles of ultrathin epitaxial GaN nanowires with diameters as small as 6 nm. In Section 6.1, we describe the decomposition of GaN NWs in MBE. By thinning as grown nanowire ensembles using a post-growth thermal annealing process similar to those reported in Refs. 183 and 184, ultrathin nanowires were fabricated with diameters down to 6 nm. We will experimentally determine the activation energy for dissociating GaN in GaN NWs. Furthermore, we will utilize QMS to enable the fabrication of ultrathin nanowire ensembles with tailored dimensions. In Section 6.2, we will develop a model to describe the decomposition of GaN NWs based on our observations by SEM and QMS. In Section 6.3, we will report on the unprecedented excitonic properties of these ultrathin NWs. In contrast to GaAs nanowires,[183] thinned GaN nanowires show intense luminescence at room temperature even in the absence of surface passivation, demonstrating that the impact of surface recombination in this material system is indeed minor. The narrowest nanowires are in fact those exhibiting the largest radiative efficiency at elevated temperatures. We show that the mismatch in dielectric constants at the nanowire surface leads to a strong enhancement of excitonic effects, reducing the exciton' radiative lifetime at room temperature and promoting radiative processes over nonradiative ones. Since the fabrication of these thinned nanowires is monitored in situ, we can control the degree of dielectric confinement of the exciton. Finally, in Section 6.4, we will give a brief outlook on the devices that may be realized with this new class of ultrathin nanowires.

Some of the results presented in this Chapter have been published in Ref. [185].

6.1. Thermal decomposition of GaN nanowires

For the growth of the NW ensembles that were subsequently decomposed, a two-step growth procedure as described in Chapter 4 was used to facilitate the fabrication of homogeneous nanowire ensembles with small diameters and low coalescence degrees without suffering from a long incubation time. The samples were grown using a Ga flux of $\Phi_{\mathrm{Ga}} = (4.5 \pm 0.5)$ nm/min and a N flux of $\Phi_{\mathrm{N}} = (7.8 \pm 0.5)$ nm/min. The substrate temperature was kept at 800°C during the first 25 min of the growth and then raised to 810°C. The growth was terminated after a total growth time of 4 h by closing simultaneously the Ga and N shutters. After the growth of the GaN nanowire ensemble, the N-plasma was switched off to re-establish UHV conditions and the substrate temperature was reduced to 600°C. For the subsequent decomposition step, the substrate temperature was then raised to 920°C. The desorbing Ga flux $\Phi_{\mathrm{Ga}}^{\mathrm{des}}$ was monitored in situ during the experiments by QMS. The decomposition of the nanowire ensemble was terminated by cooling down the substrate.

Figure 6.1(a) presents a scanning electron micrograph of a GaN nanowire ensemble

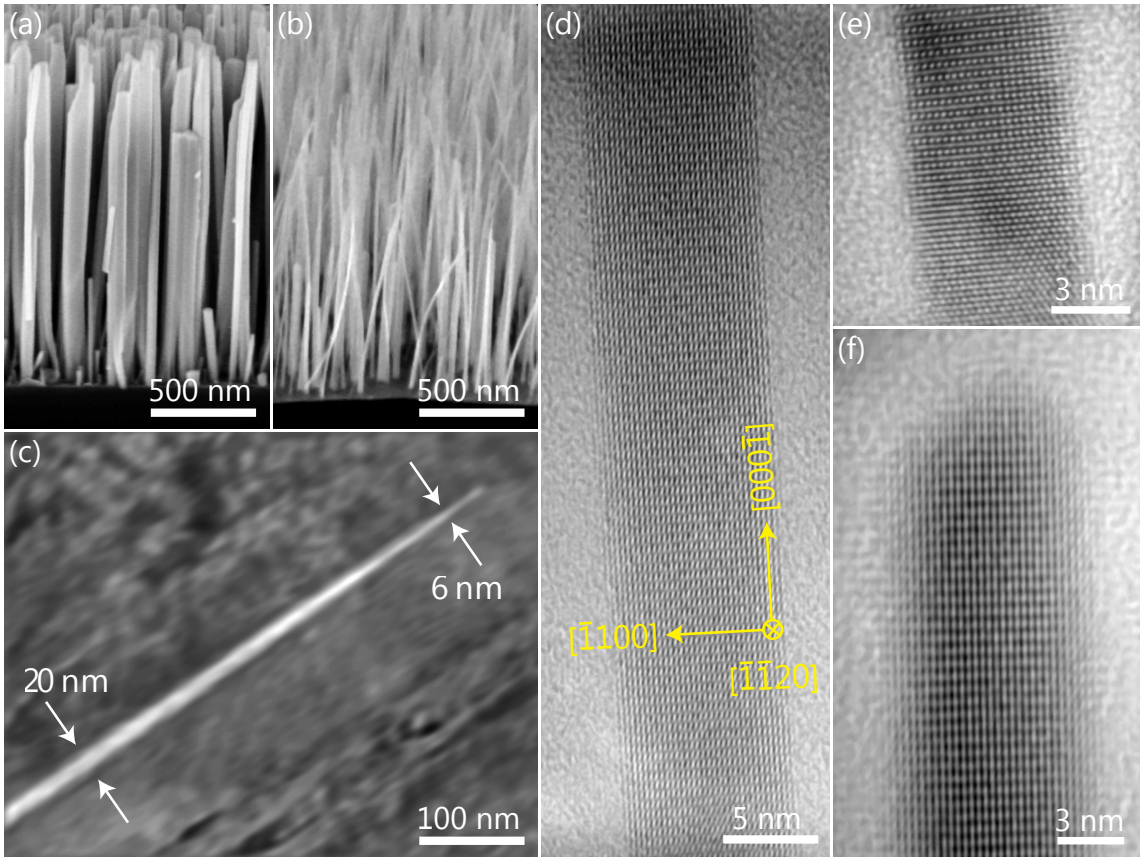

Figure 6.1: Sample morphology before and after thermal decomposition. [(a), (b)] Bird's eye view scanning electron micrographs of GaN nanowire ensembles (a) before and (b) after thermal decomposition for 30 minutes at 920°C in UHV. The nanowire length decreases from 1.6 to 1.1 µm. The areal density for the as-grown nanowires is 9×10^9 cm^{-2}. (c) Scanning electron micrograph of a partially decomposed GaN nanowire dispersed on a Si substrate. The decomposition process results in some tapering. The diameter at the tip of the nanowire is 6 nm. [(d), (e)] High-resolution transmission electron micrographs reveal that the partially decomposed nanowires are single crystals and exhibit smooth sidewalls. (f) High-resolution transmission electron micrograph of the tip of the nanowire shown in (d). The micrographs [(d)–(f)] have been enhanced by a Fourier filter selecting the relevant spatial frequencies corresponding to the distance of the $\{0002\}$ and the $\{1\bar{1}00\}$ planes. SEM measurements partially carried out by Anne-Kathrin Blum and Uwe Jahn. TEM measurements carried out by Esperanza Luna.

removed from the MBE chamber without undergoing a post-growth decomposition step. These nanowires exhibit a length of 1.6 µm and an areal density of 9×10^9 cm^{-2}. The 51 nm diameter of these nanowires is much larger than the exciton Bohr radius in GaN ($a_B = 3$ nm), and neither dielectric nor quantum confinement is expected. Dielectric confinement of the exciton starts to be noticeable for diameters of $5a_B$.[167,186,187] Nanowires this thin are difficult to obtain by direct growth.[66] As shown in Fig. 6.1(b), annealing an as-grown nanowire ensemble for 30 min at 920°C in UHV results in a reduction in the length and diameter of the nanowires. The analysis of cross-sectional and top-view micrographs reveals that the average length decreases to approximately 1.1 µm, while the areal density of nanowires is not drastically reduced. Although partially decomposed nanowires also appear to be much thinner than the as-grown ones, a reliable assessment of the final nanowire diameter by scanning electron microscopy is not straightforward. Under electron irradiation, the nanowires bend and bundle due to charging, leading to an overestimation of their diameter when analyzing top-view and cross-sectional images.[56,183] Upon thermal decomposition, the nanowires also exhibit a pronounced tapering, suggesting that the nanowire diameter decreases faster at their tip than at the bottom part. For instance, the average base diameter for the nanowires in Fig. 6.1(b) is 32 nm, while the diameter along the top 600 nm of the nanowire in Fig. 6.1(c) decreases from approximately 20 to 6 nm. Our systematic observation of wire tapering contrasts with the homogeneous reduction in nanowire diameter during thermal decomposition of the CVD synthesized GaN NW "bales" reported in Ref. [184]. This discrepancy might be related to the fact that the decomposition process in Ref. [184] took place in H_2 or NH_3 atmospheres instead of in UHV.

High-resolution transmission electron micrographs taken close to the tip of individual partially decomposed nanowires are shown in Figs. 6.1(d) and 6.1(e). The nanowires are single crystals and are free of any dislocations as the as-grown nanowires.[188] Despite the pronounced tapering detected by scanning electron microscopy [Fig. 6.1(c)], the nanowire sidewalls remain atomically abrupt upon thermal decomposition. The direct observation of atomic planes allows one to accurately determine the nanowire diameter, which we find equal to (8.8 ± 0.3) and $(5.8 \pm 0.39$ nm (corresponding to 32 and 21 atomic planes, respectively) in Figs. 6.1(d) and 6.1(e), respectively. Figure 6.1(f), taken at the top of the nanowire shown in Fig. 6.1(d), shows that the tip diameter of this thinned nanowire is below 5 nm.

As shown above, thermal decomposition facilitates the fabrication of ultrathin GaN nanowires while preserving their high structural perfection. In contrast to previous decomposition studies,[183,184] we monitor the decomposition in situ by QMS[50,63,64] and can thus control this process. Since the dissociation of GaN in UHV is thermally activated,[95,189,190] the decomposition rate of GaN nanowires is controlled primarily by the substrate temperature. Figure 6.2(a) depicts the change of substrate temperature and the resulting temporal evolution of the desorbing Ga flux $\Phi_{\mathrm{Ga}}^{\mathrm{des}}$ as measured by QMS in units of ion current during the post-growth decomposition of the sample shown in Fig. 6.1(b). For the decomposition, the temperature was ramped within 10 min from 680 to 920 °C, and then kept constant for 30 min. Note that, after reaching 920 °C, the reading of the substrate temperature (acquired with an optical pyrometer) was not constant but steadily decreased until stabilizing at 905 °C. This effect is attributed not to actual temperature changes but to the decrease in the effective refractive index of the GaN NW ensemble during decomposition. Thereby, the emissivity of the sample changes which distorts the temperature measurement. The temperature dependence of $\Phi_{\mathrm{Ga}}^{\mathrm{des}}$ displayed

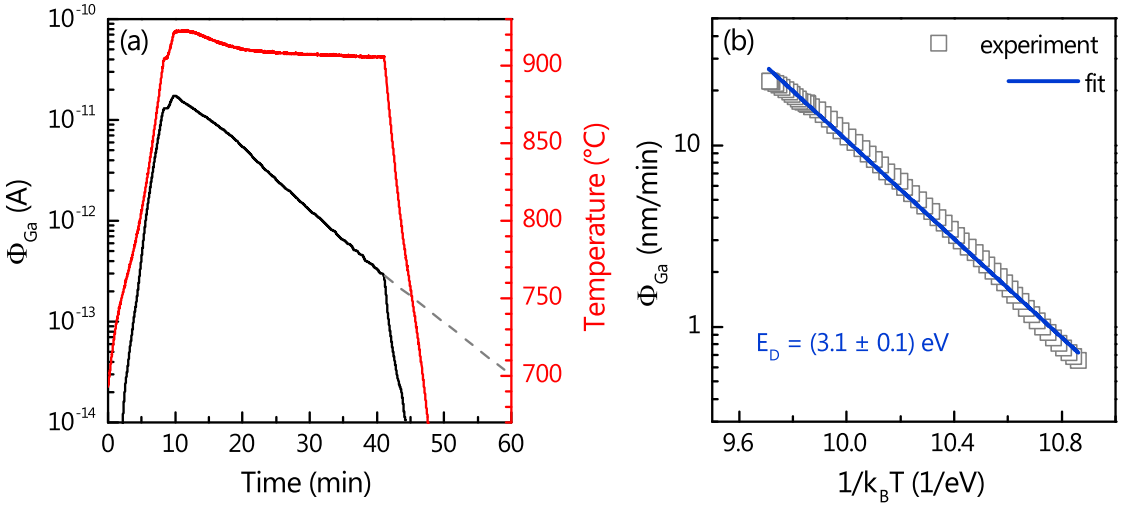

Figure 6.2: Thermal decomposition of GaN nanowires. (a) Change of substrate temperature and the resulting temporal evolution of the desorbing Ga flux $\Phi_{\mathrm{Ga}}^{\mathrm{des}}$ (red and blue lines, respectively) during the decomposition of a GaN nanowire ensemble. The ion flux is given in units of ion current. The dashed line shows an exponential extrapolation of $\Phi_{\mathrm{Ga}}^{\mathrm{des}}$ to the background level. (b) Arrhenius representation of the temperature dependence of $\Phi_{\mathrm{Ga}}^{\mathrm{des}}$ during the decomposition of a GaN nanowire ensemble. The line shows a fit with an activation energy of $E_D = (3.1 \pm 0.1)$ eV.

in Fig. 6.2(b) has been obtained from the 10 min temperature increase in Fig. 6.2(a) (see the methods section for more details on the conversion of $\Phi_{\mathrm{Ga}}^{\mathrm{des}}$ to equivalent growth rate units of nm/min). Within this temperature range, $\Phi_{\mathrm{Ga}}^{\mathrm{des}}$ increases by almost two orders of magnitude and is as high as 15 nm/min at 920°C. Despite the thermally-induced morphological changes in the nanowire ensemble (Fig. 6.1), $\Phi_{\mathrm{Ga}}^{\mathrm{des}}$ approximately follows an Arrhenius-like temperature dependence [Fig. 6.2(b)]:

$$\Phi_{\mathrm{Ga}}^{\mathrm{des}}(T_S) = C_1 \exp\left(-E_D/k_B T_S\right), \tag{6.1}$$

where E_D denotes the activation energy for the nanowire decomposition, T_S the substrate temperature, and C_1 a constant. The best fit to the data yields $E_D = (3.1 \pm 0.1)$ eV, identical to the value reported for the layer-by-layer decomposition of GaN(0001) films in vacuum.[95]

In contrast to the layer-by-layer decomposition of GaN films, where $\Phi_{\mathrm{Ga}}^{\mathrm{des}}$ remains constant at a fixed temperature,[95] for a nanowire ensemble this quantity decays exponentially [Fig. 6.2(a)]. Therefore, in the nanowire case, the decomposition rate is somehow proportional to the amount of remaining material. Extrapolating $\Phi_{\mathrm{Ga}}^{\mathrm{des}}$ to the background level allows one to estimate the total GaN volume fraction that has been decomposed during the thermal annealing process. For instance, the QMS data in Fig. 6.2(a) indicate that a 30 min annealing at 920 °C in UHV leads to the decomposition of $(96 \pm 2)\%$ of the material. To confirm this analysis, we performed quantitative Rutherford backscattering measurements on this sample and on the as-grown nanowire ensemble, and we obtained a volume fraction of decomposed material of $(96.2 \pm 1.6)\%$ (see appendix A.1). QMS appears to be sufficiently accurate for a quantitative in situ control of the decomposition of GaN nanowires, enabling the fabrication of ultrathin nanowire ensembles with tailored dimensions.

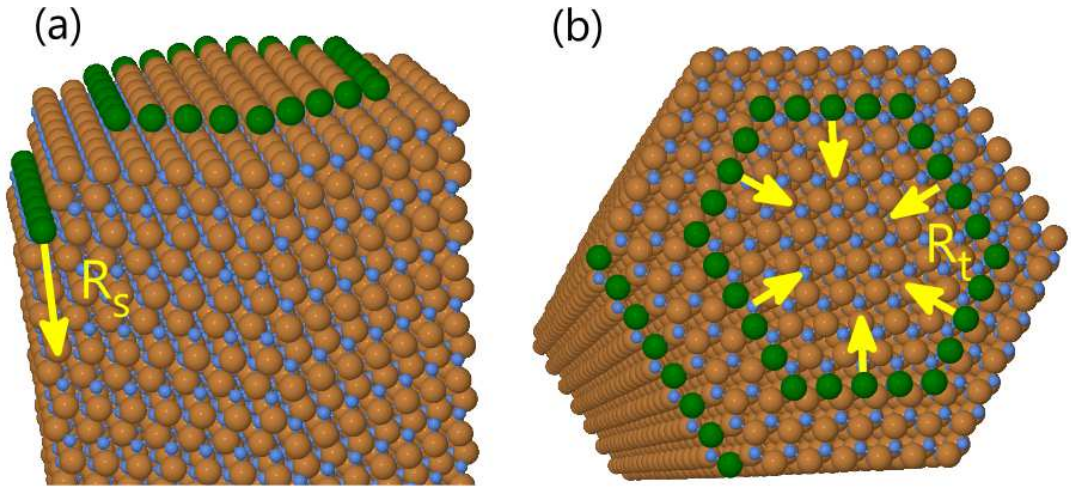

Figure 6.3: Schematic representation of the layer-by-layer decomposition process along the (a) sidewalls and (b) top facets. The green atoms denote the respective step edge and the yellow arrows indicate how the decomposition process at the side and top facets proceeds.

6.2. Modelling nanowire decomposition

The temporal evolution of $\Phi_{\mathrm{Ga}}^{\mathrm{des}}$ gives further insight into the decomposition of GaN nanowires in UHV. The micrographs in Fig. 6.1 indicate that both the diameter and the length reduce over time. Based on the value taken by E_D [Fig. 6.2(a)] and considering the smooth sidewalls after partial decomposition [Figs. 6.1(d)–6.1(f)], we infer that the top and side facets of the nanowire decompose layer-by-layer, as illustrated in Figs. 6.3(a) and 6.3(b). Assuming that the decomposition rate is limited by the creation of kinks at the edges between the sidewalls and the top facet, it is possible to obtain an analytic expression for the temporal evolution of $\Phi_{\mathrm{Ga}}^{\mathrm{des}}$.

Since $\Phi_{\mathrm{Ga}}^{\mathrm{des}}$ is proportional to the average decrease in the volume of individual nanowires, its temporal evolution is given by:

$$\Phi_{\mathrm{Ga}}^{\mathrm{des}} = -C_2 \frac{dV}{dt}, \tag{6.2}$$

where C_2 denotes a constant, V the nanowire volume, and t the time. We assume for simplicity that the nanowire has a cylindrical shape. The volume of the nanowire is thus:

$$V = \pi r^2 h, \tag{6.3}$$

where r and h represent the nanowire diameter and height, respectively. Then, $\Phi_{\mathrm{Ga}}^{\mathrm{des}}$ can be written as

$$\Phi_{\mathrm{Ga}}^{\mathrm{des}} = -C_2 \pi r \left[2h \frac{dr}{dt} + r \frac{dh}{dt} \right]. \tag{6.4}$$

The micrographs in Fig. 6.1 demonstrate that both r and h vary over time. The specific temporal evolution of these parameters is a priori unknown. If the layer-by-layer decomposition rate is limited by the creation of kinks at the edges of the sidewalls with the top facet, the temporal evolution of r and h is proportional to the perimeter of the nanowire cross-section and does not depend on h because the different atomic layers decompose

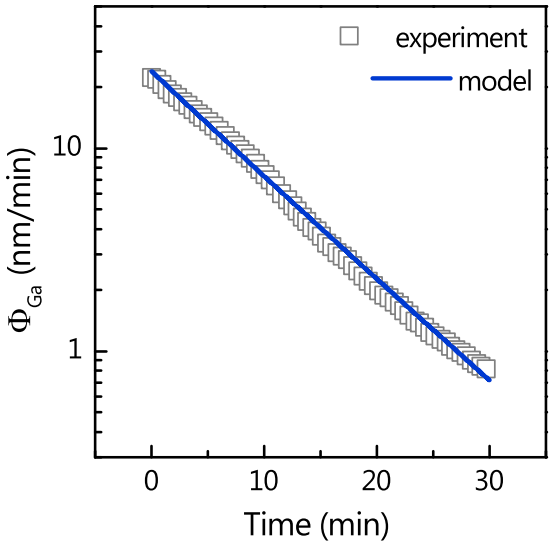

Figure 6.4: Temporal evolution of Φ_{Ga}^{des} during thermal decomposition at 920 °C. The line shows the result of a fit using the modeling described below and yields layer-by-layer decomposition rates for the top facet and for the sidewalls of $\pi R_s = 0.094$ and $\pi R_t = 0.528$ nm/min, respectively.

before a new kink is created. Under such an assumption, r and h can be written as:

$$\frac{dr}{dt} = -R_s \pi r, \tag{6.5}$$

$$\frac{dh}{dt} = -R_t \pi r, \tag{6.6}$$

$$r(t=0) = r_0, \tag{6.7}$$

$$h(t=0) = h_0, \tag{6.8}$$

where R_s and R_t represent the decomposition rate constants for the nanowire side and top facets, respectively [see Figs. 6.3(a) and (b)], and where $r_0 = 25.5$ nm and $h_0 = 1.6$ µm are the initial NW radius and height, respectively. We thus obtain the following analytical expression for the temporal evolution of the dissociation rate:

$$\Phi_{Ga}^{des} = C_2(\pi r_0)^2 \exp\left(-3\pi R_s t\right) \cdot \left[6 r_0 R_t + 2\exp\left(\pi R_s t\right)\left(h_0 R_s - 2 r_0 R_t\right)\right]. \tag{6.9}$$

Eq. 6.9 was then fitted to the data in Fig. 6.4(c) using the experimentally determined length and diameter distributions of the as-grown ensemble. We then obtained $R_s = 2.5 \times 10^{-4}$ s^{-1} and $R_t = 2.8 \times 10^{-3}$ s^{-1} as the decomposition rates for the sidewalls and top facet, respectively. While on an absolute scale the top facet decomposition proceeds faster, due to the NW morphology, the change in diameter is more impacting. Despite our model does not take into account that in reality a new layer can start decomposing before the previous one has be completely decomposed [what results in the nanowire tapering illustrated in Fig. 6.7(c)], it describes well the temporal evolution of Φ_{Ga}^{des} during the thermal decomposition process, as shown in Fig. 6.4.

As a result, also the NW diameter and height distributions of the decomposed ensemble is calculated. Due to the difficulties in determining the former experimentally, these calculations may serve as a good estimate for the diameter distribution of the ultrathin NWs. However, besides not including tapering, the model can also not distinguish

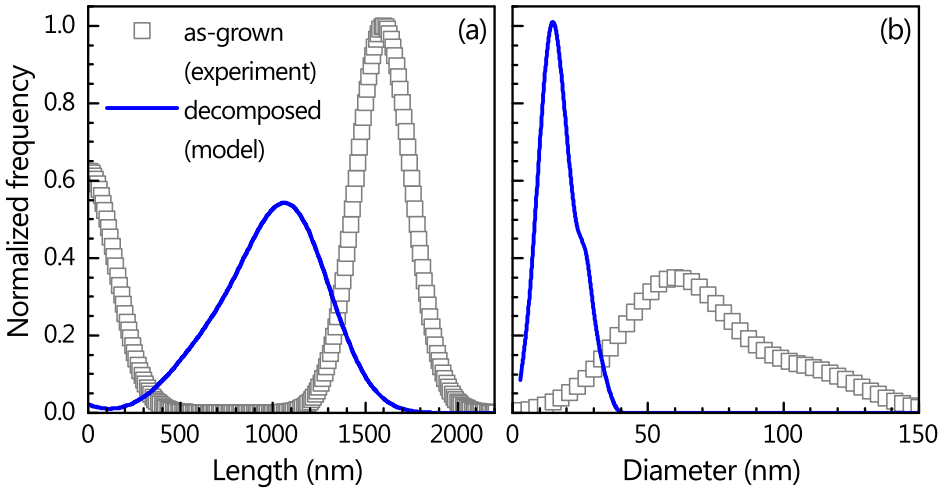

Figure 6.5: (a) height and (b) diameter distribution of the NW ensemble before and after decomposition. While the distributions of the as-grown NW ensemble could be reliably obtained from statistical shape analysis (grey squares), the distributions of the ultrathin NWs are a result of the ensemble simulations (blue lines).

uncoalesced and coalesced NWs. The ladder in reality are expected to separate again at some point and continue to decompose individually. However, as is shown in Figure 6.5, the model yields not only a NW length distribution after decomposition that agrees well with the experimental observation (approximately 1100 nm in average) but also a reasonable diameter distribution.

Analogously, the temporal evolution of height and diameter of an individual NW during decomposition can be modeled. Figure 6.6 depicts the effect of the decomposition of an average uncoalesced NW on its height and diameter. As explained above, with proceeding decomposition both the NW height and diameter are reduced. Since the decomposition rate depends on the perimeter of the NW, the reduction in height and diameter slow down, as the diameter decreases. This behavior also is in agreement with the observations made in Section 5.1.2, were thin but supposedly stable bottom parts of the NWs during high-temperature growth of long NWs were observed. There the decomposition of these bottom parts has slowed down drastically so that the NWs actually remain on the substrate and do not fall off even for long growth runs.

Despite its simplicity, our modeling describes the temporal evolution of $\Phi_{\mathrm{Ga}}^{\mathrm{des}}$ very well. According to the deduced decomposition rates, the NW top facets decompose faster than the sidewalls, in agreement with our experimental observations [Fig. 6.1]. Our understanding on the evolution of the shape of the nanowires during thermal decomposition is illustrated and summarized in Figs. 6.7(a)–(c). Prior to decomposition, the nanowires have a (more or less regular) hexagonal cross-sectional shape with an abrupt vertical edge between side and top facets [Fig. 6.7(a)]. The decomposition of the facets proceeds layer-by-layer, and is initiated at the edges between the side and top facets [Fig. 6.7(b)]. For simplicity, in our decomposition model we assume that the creation of kinks at the edges between the side and top facets is the rate limiting step for the decomposition process. Consequently, the decomposition rate is proportional to the nanowire's cross-sectional perimeter at the top facet. In reality, a new layer may start decomposing before the previous one is completely decomposed. This explains the tapering observed experimentally and illustrated in Fig. 6.7(c).

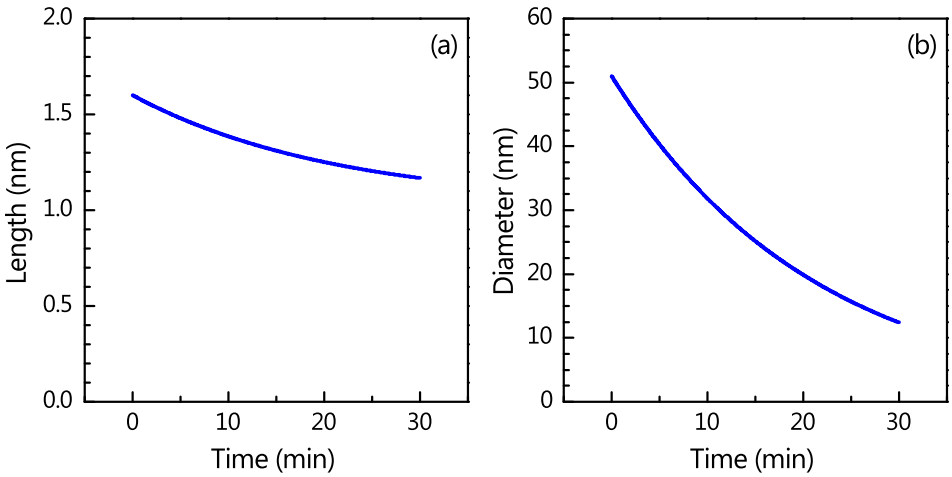

Figure 6.6: Temporal evolution of (a) NW height and (b) NW diameter during the decomposition step as obtained from the simulation.

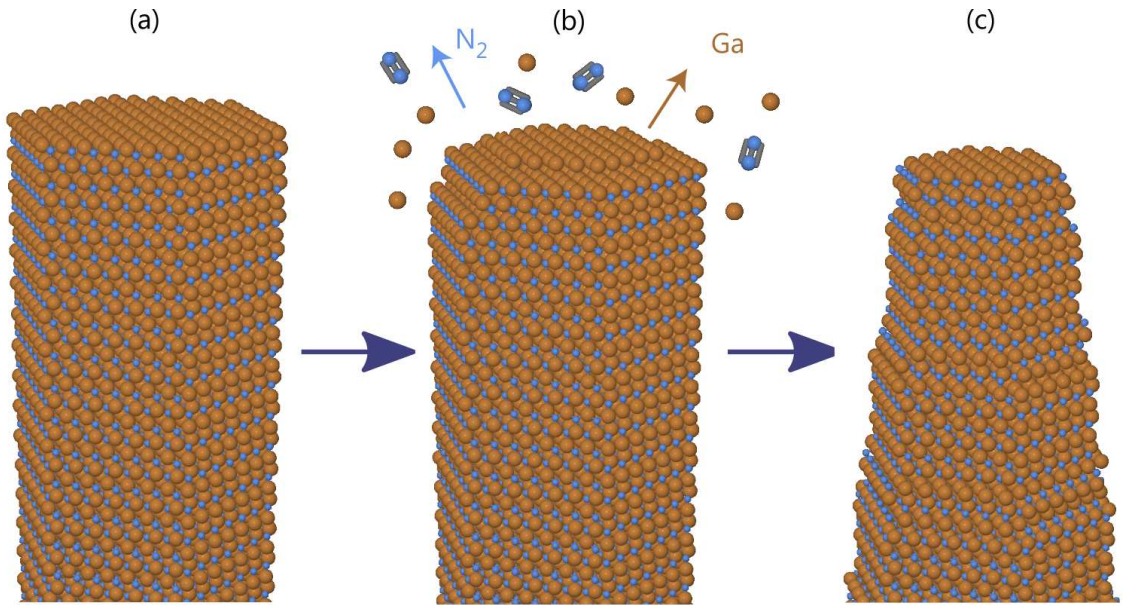

Figure 6.7: Schematic representation of the morphology of a GaN nanowire during thermal decomposition in UHV. Panel (a) shows the initial morphology of the as-grown nanowire, (b) the morphology at the onset of lateral and axial decomposition, and (c) the final morphology, which is characterized by a pronounced tapering caused by the simultaneous decomposition of several atomic layers.

6.3. Properties of ultrathin GaN nanowires

Because of the NW tapering and the experimental difficulty to obtain the diameter of the NWs at their tip, we will characterize the NWs in all what follows by their base diameter d_B. This latter value can be reliably obtained by a statistical analysis of cross-sectional scanning electron micrographs and was found to scale with the decomposed volume as obtained by QMS. Note, however, that the photoluminescence signal of these thinned nanowires is certainly not dominated by recombination of carriers at their base (NW bases are usually optically dead due to Si indiffusion from the substrate). Therefore, their emission properties are not determined by their base diameter, but rather by their diameter closer to the tip. These values are very different: for instance, the thinned nanowires obtained after a 30 min annealing at 920°C shown in Figs. 6.1(b)–6.1(f) exhibit a base diameter of $d_B = 32$ nm, but a diameter close to the tip of less than 10 nm [cf. Fig. 6.1(d)].

The obtained diameters are still significantly larger than the Bohr radius of the exciton in bulk GaN ($a_B = 3$ nm), i. e., no quantum confinement should occur in any of the samples under investigation. Yet, as shown in Fig. 6.8(a), the photoluminescence peak energy at 300 K for ensembles of partially decomposed GaN nanowires increases from 3.412 to 3.454 eV with progressive decomposition. This observation is a signature of dielectric confinement: the image charges resulting from the large mismatch between the relative dielectric constants of GaN and vacuum lead to a renormalization of the bandgap and to an increase in the strength of the Coulomb interaction.[163,165,166,173] With decreasing d_B, the radial dielectric confinement of the exciton becomes stronger, and consequently, the photoluminescence line of thinned nanowires is blueshifted. Furthermore, the smaller d_B, the larger the emission broadening [Fig. 6.8(a)], since the emission energy increasingly depends on diameter. A similar behavior is observed at 5 K, where the near band-edge emission of the GaN nanowire ensemble is dominated by the recombination of excitons bound to donors and to stacking faults [Fig. 6.8(b)].[86] Both the donor-bound and the stacking fault-bound exciton transitions blueshift and broaden with decreasing nanowire diameter.

Since we are dealing with bare GaN nanowires with free, unpassivated surfaces, one would expect surface recombination to become more important for the thinner nanowires. The emission intensity from the thinned nanowires should thus be considerably weaker than for the as-grown ensemble, as reported for GaAs nanowires.[175,183] Figure 6.8(c) compares the photoluminescence intensity at 300 K of the as-grown nanowires with that of thinned nanowires with $d_B = 32$ nm. The photoluminescence spectrum of the thinned nanowires was normalized by the volume fraction of material left after decomposition. The normalization factor was obtained independently from the QMS analysis shown in Fig. 6.2(a) and from Rutherford backscattering experiments (see appendix A.1). Contrary to what is expected in the presence of efficient surface recombination, the normalized integrated emission intensity for the thinned nanowires is actually larger (2.6 times) than that of the as-grown ensemble [Fig. 6.8(c)]. This high emission intensity from the thinned nanowires does not originate from an increase in nanowire-light coupling with decreasing diameter. In fact, in our experimental geometry (see Methods), the light coupling between the thinned nanowires and free space is reduced compared to the as-grown nanowires.[191] The observation in Fig. 6.8(c) thus demonstrates that nonradiative recombination at the sidewalls of thinned nanowires is negligible at 300 K.

To get a deeper insight into the radiative efficiency of ultrathin GaN nanowires, we investigate our samples by time-resolved photoluminescence spectroscopy. For sponta-

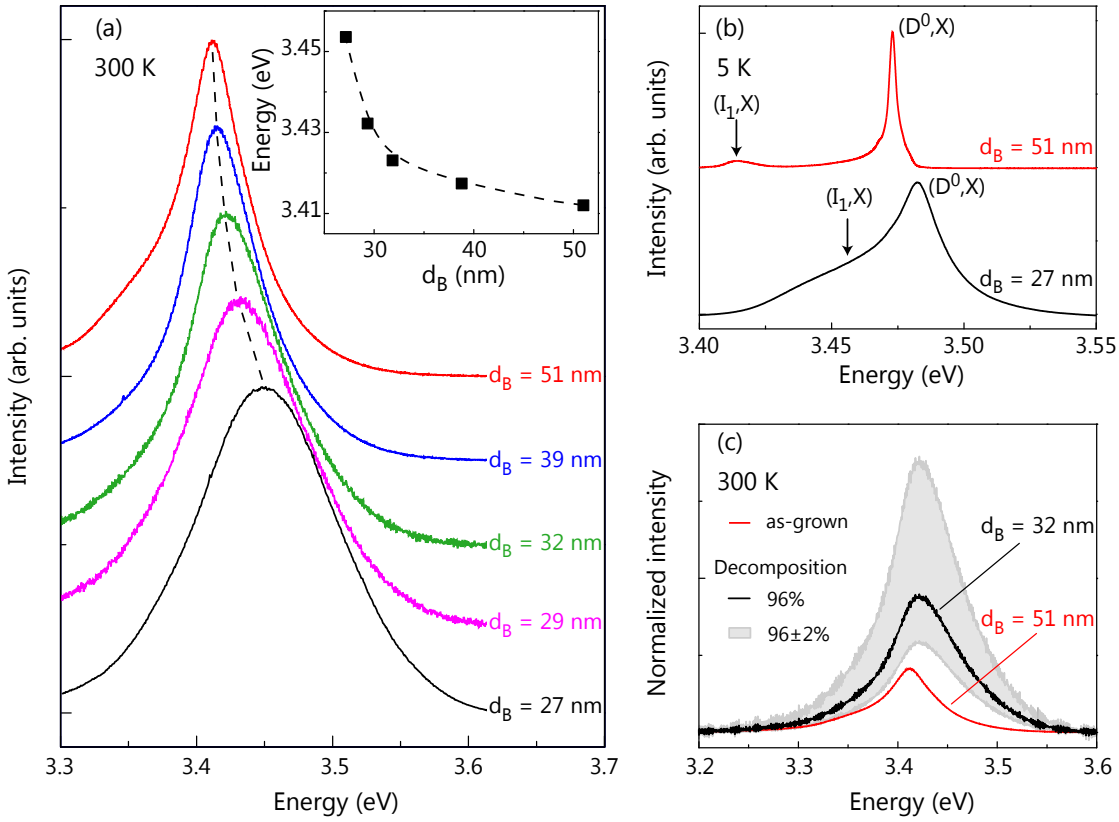

Figure 6.8: Dielectric confinement in ultrathin GaN nanowires.(a) Photoluminescence spectra at 300 K from an ensemble of as-grown GaN nanowires (top spectrum) and from partially decomposed GaN nanowire ensembles with different average base diameters d_B as indicated in the figure. The spectra have been normalized and shifted vertically for clarity. The dashed lines are guides to the eye. The free exciton transition shows a 42 meV blueshift with decreasing diameter (see inset). This blueshift arises from the radial dielectric confinement of the exciton due to the dielectric mismatch between GaN and vacuum. (b) At 5 K, the photoluminescence spectra are dominated by the recombination of excitons bound to donors. The weaker band highlighted by arrows arises from the recombination of excitons bound to basal plane stacking faults. Both excitonic transitions blueshift with decreasing d_B due to dielectric confinement. (c) Photoluminescence spectra recorded at 300 K from the ensemble of as-grown nanowires (red) and from the ensemble of thinned nanowires with $d_B = 32$ nm [Fig. 6.1(b)]. The black line shows the photoluminescence spectrum of the thinned nanowires after normalizing their emission intensity by the volume ratio. The grey shaded area shows the intensity uncertainty corresponding to the $\pm 2\%$ error from the QMS and RBS analysis. PL measurements carried out by Pierre Corfdir and Christian Hauswald.

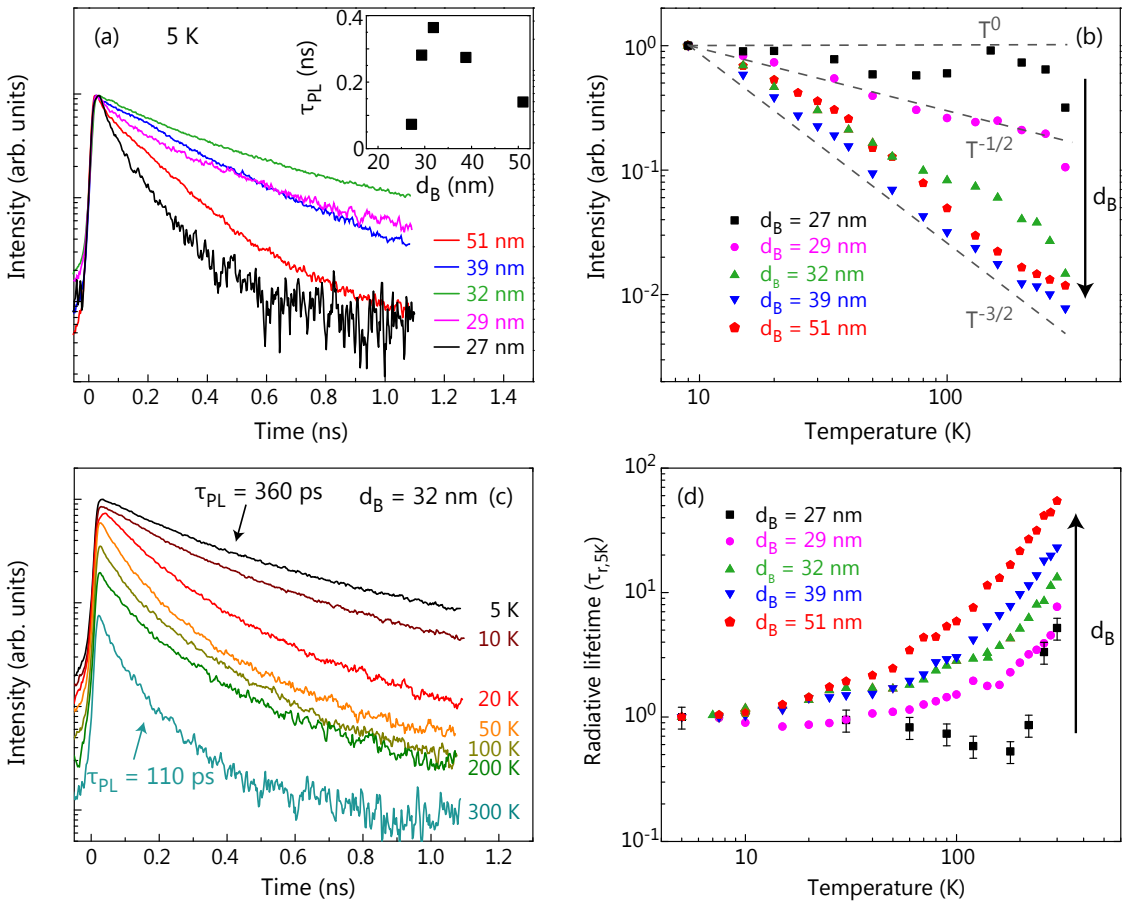

Figure 6.9: Radiative and nonradiative recombination of excitons in ultrathin GaN nanowires. (a) Photoluminescence transients recorded at 5 K for the same samples as in Fig. 6.8(a). The inset shows the photoluminescence decay time τ_{PL}, obtained using an exponential fit, as a function of d_B. The nonmonotonic diameter dependence of τ_{PL} demonstrates that surface recombination at the nanowire sidewalls does not dominate recombination even for very thin nanowires. (b) Spectrally integrated photoluminescence intensity as a function of temperature for the samples under investigation. The dashed lines are guides to the eye. The thinner the nanowires, the weaker the photoluminescence quenching with temperature, and the larger the radiative efficiency at 300 K. (c) Photoluminescence transients as a function of temperature for the ensemble of thinned nanowires with $d_B = 32$ nm. The nonradiative lifetime only decreases by a factor of 3 over a temperature range from 5 to 300 K. This reduction is too small to account for the quenching of the photoluminescence intensity observed in panel (a) for this sample. (d) Temperature dependence of the exciton radiative lifetime for the samples under investigation. The radiative lifetimes are given in units of the radiative lifetime at 5 K ($\tau_{r,5K}$). For all samples, the temperature dependence of the radiative lifetime is consistent with the one of the emission intensity. The thinner the nanowire, the weaker the increase in radiative lifetime with temperature and the larger the radiative efficiency. PL measurements carried out by Pierre Corfdir and Christian Hauswald.

neously formed GaN nanowires grown by molecular beam epitaxy, the exciton decay has been shown to be largely nonradiative even at low temperatures, as reflected by decay times τ_{PL} between 150 and 200 ps.[87] Figure 6.9(a) shows photoluminescence transients recorded at 5 K from the samples under investigation. The decay times derived from the photoluminescence transients are shown in the inset. For the as-grown ensemble, we observe a decay time of 140 ps, similar to those obtained from comparable samples studied previously.[86,87] Strikingly, the decay time of the thinned nanowires is not shorter, but (with the exception of the sample with the thinnest nanowires) longer than that of the as-grown ensemble. Since the decay of excitons in these GaN nanowires at 5 K is dominated by nonradiative recombination at point defects,[87] this observation suggests a reduction in point defect density after the thermal annealing process.

Figure 6.9(b) shows the temperature dependence of the near band-edge emission intensity for the samples under investigation. The photoluminescence intensity for thick nanowires follows a $T^{-3/2}$ dependence. This behavior is characteristic for spontaneously formed GaN nanowires in general (behaving like bulk GaN) and reflects the increase in radiative lifetime with temperature with the nonradiative lifetime staying essentially constant.[87] Remarkably, the quenching in photoluminescence intensity with temperature for our thinned nanowires is less pronounced. In particular, for the ensemble with $d_B = 27$ nm, the photoluminescence intensity remains constant between 5 and 150 K and quenches only for higher temperatures. As for the as-grown nanowires, the quenching is mainly controlled by the temperature dependence of the radiative lifetime. For example, the photoluminescence intensity of the sample with a base diameter of 32 nm is reduced by a factor of 70 when increasing the temperature from 5 to 300 K. In the same temperature interval, the photoluminescence decay time τ_{PL} (which essentially represents the nonradiative lifetime) is reduced by a factor of only 3.3 as shown in Fig. 6.9(c).

Since relaxation processes are fast in comparison to recombination mechanisms, the radiative lifetime is proportional to the inverse of the emission intensity at zero delay. Figure 6.9(d) shows the thus obtained evolution of the radiative lifetime as a function of temperature for all samples, normalized to the value of the radiative lifetime at 5 K ($\tau_{r,5K}$). The thinner the nanowires, the slower the increase in radiative lifetime between 5 and 300 K [Fig. 6.9(d)], and thus the weaker the quenching of the photoluminescence intensity [Fig. 6.9(b)].

Due to the delocalization of carriers in $\mathbf{k}$-space with increasing temperature, the radiative lifetime of a population of excitons with a dimensionality n increases as $T^{n/2}$.[86] The slower increase in radiative lifetime observed for the thinnest nanowires is thus evidence of reduced exciton dimensionality in these structures. In other words, the impact of the dielectric mismatch in ultrathin GaN nanowires is strong enough to quantize the center-of-mass motion of the exciton perpendicular to the nanowire axis, i. e., thinned GaN nanowires are actually quantum wires.

Note that below 200 K, the increase in radiative lifetime for our thinnest nanowires is even slower than the $T^{1/2}$-dependence expected for ideal quantum wires.[192] We attribute this finding to the fact that we do not deal with a purely one-dimensional exciton distribution, but rather with one-dimensional free excitons thermalized with a distribution of zero-dimensional excitons bound to donors and to stacking faults [Fig. 6.8(b)]. The presence of these localized states and their coupling with free excitons[86,87] leads to a slower increase in exciton radiative lifetime with temperature.[193,194] Finally, the delocalization of excitons from donors and stacking faults leads to an increase in exciton coherence length, giving rise to the decrease in radiative lifetime observed between 50 and 150 K for thinned

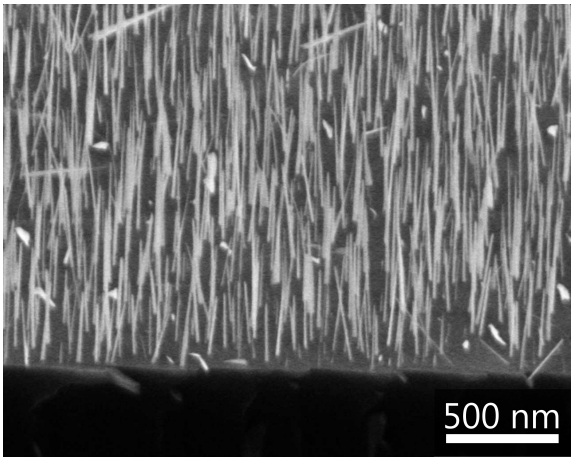

Figure 6.10: Scanning electron micrograph of an ultrathin NW ensemble where the NW number density was drastically decreased.

nanowires with $d_B = 27$ nm.

6.4. New prospects opened by ultrathin GaN nanowires

Above, we have overcome the third fundamental limitation of spontaneous GaN NW formation, namely the difficulty to fabricate ultrathin GaN nanowires. When decomposing the NWs for longer times, eventually also the NW number density is significantly reduced (Fig. 6.10). This additional effect may pave the way for core-shell growth of III-N NWs by MBE and therefore the realization of alternative devices concepts. Most importantly, however, these unpassivated, ultrathin nanowires exhibit intense excitonic emission at room temperature, demonstrating that surface recombination at the sidewalls of GaN nanowires is slow in comparison to other recombination processes. Excitonic effects in thinned nanowires are enhanced by the mismatch in dielectric constants of GaN and vacuum. The dielectric confinement of the exciton gives rise to an increase in the internal radiative efficiency, which is largest for the thinnest nanowires. Thinned GaN nanowires are thus a promising system for optoelectronic devices operating in the strong coupling regime.[195,196] In particular, microcavities with thinned (In,Ga)N nanowires as an active medium pave the way for achieving polariton lasing in the visible range. Ultrathin nanowires form also an attractive platform for quantum optics applications. For instance, the in situ control of the nanowire diameter facilitates the realization of quantum dots with a well-defined lateral shape, and it paves the way for the tuning of the radial confinement of the exciton in crystal-phase quantum dots.[86,197] The samples obtained here have led to subsequent investigations and a publication crystal-phase quantum dots included in the ultrathin nanowires.[42]. Additional experiments on InN quantum dots in ultrathin GaN NWs acting as single photon emitters are planned.

7. Conclusions and Outlook

In this thesis, we have studied the spontaneous formation of GaN nanowires in molecular beam epitaxy. As for any self-organized or self-controlled process, the amount of control that can generally be achieved is limited. A higher control over the morphology and properties of GaN NWs, however, is highly desirable. The results obtained in this work are not only highly relevant for fundamental studies of the NWs themselves but also open new perspectives for the development of new devices based both on spontaneously formed and selective-area-grown NWs.

We have started out recapturing recent findings on the impact of the growth conditions on the nucleation and growth of GaN NWs. Based on these experiments conducted here at the Paul-Drude-Institut für Festkörperelektronik and other reports in literature on the matter, we identified the four major limitations in the spontaneous formation of GaN NWs: (i) the limited control over the number density, (ii) the high coalescence degree that comes as a direct consequence of the high number density and introduces crystal defects, (iii) the NW diameter that is usually larger than 30 nm and thus too large for lateral quantum confinement and (iv) the limited feasible substrate temperature that is believed to diminish the structural quality of the NWs by allowing the incorporation of point defects.

In the main part of this work, we have utilized unconventional growth conditions and procedures to one-by-one overcome these limitations and enable the fabrication of spontaneously formed GaN NW ensembles with unprecedented properties in many different aspects.

First, we have introduced a two-step growth approach where we altered the growth conditions during NW nucleation in order to influence their morphology. Thereby, we managed to prepare long NW arrays with area coverages down to 17%. While the NWs density was only slightly affected, a more pronounced effect was observed regarding average diameter decreasing from 70 to 45 nm and the coalescence degree that was reduced from 97% to 74%. In addition, we observed an electrostatic charging of our thin, long NWs that lead to an attraction of adjacent NWs and thereby introduced an additional, non-intrinsic coalescence. The electrostatic charging we believe to be caused by electrons originating from the N-plasma combined with the poor grounding of the NWs due to the Si_xN_y interlayer. If additional measures are introduced to prevent the electrostatic charging of the NWs, such as negatively biasing the substrate to deflect the impinging electrons or using a more conductive substrate like metals, we expect that the coalescence degree of long NW ensembles grown under comparable growth conditions can again be drastically reduced. The preparation of GaN NW ensembles with lower coalescence degrees will enable the fabrication of NW-based devices with more uniform properties.

Extended experiments on the two-step growth have allowed to us to obtain a better understanding of the NW nucleation processes. We discovered that NW nucleation cannot be entirely suppressed using a two-step growth approach. In fact, new NWs continuously nucleate, their formation rate can only be slowed down. However, at the same time also the elongation rate of the already existing NWs will drop in a comparable manner as these NWs lack a significant Ga flux due to the absence of collective effects for lower

NW number densities. For any growth conditions, as long as some degree of growth proceeds, NW nucleation will continue until eventually reaching the typical high number density on the order of 10^9–10^{10} cm^{-3}. These observations represent an improvement in the understanding of the nucleation mechanisms of spontaneously formed NWs and contribute to the complete comprehension of this nucleation process.

In addition, an alternative form of the two-step growth allowed us to fabricate GaN NWs faster without influencing their structural or optical properties. Here, the growth conditions were altered at the end of the incubation stage instead of during the nucleation stage. This means that the incubation time which may become as long as several hours for certain growth conditions (low III/V ratio, high temperature) can be reduced to arbitrary times. This result contradicts what would be typically expected and again leads to an improved understanding of the nucleation process of spontaneously formed GaN NWs. It has turned out that the growth conditions during the incubation stage do not influence the properties of the final NW ensemble. More importantly, the presented approach allows the fabrication of a certain NW ensemble within a significantly shorter growth time. This approach has proven to be highly valuable in the subsequent chapters where GaN NW ensembles were prepared at high substrate temperatures or low III-V ratios.

Summarizing the effects of the two-step growth, we can state that while we could not yet decrease the NW number density of long and homogeneous NW ensembles, we managed to significantly reduce the coalescence degree. Thereby, we have overcome the first of the limitations of the spontaneous formation of GaN NWs. In addition, we provide proposals on how the coalescence degree may be further reduced. Simultaneously, we have obtained an improved understanding of GaN NW nucleation and developed a growth procedure that proved extremely valuable when growing at high temperature or using low III/V ratios in order to overcome the other limitations discussed above.

Next, we investigated the growth of GaN NWs at unexplored substrate temperatures. Three unconventional growth approaches were introduced to enable to nucleation and growth of GaN NWs in MBE at higher substrate temperatures. By using nominally Ga-rich growth conditions, utilizing the two-step growth approach discussed above, and growing on alternative substrates with a lower nucleation barrier, we demonstrated the fabrication of NW ensembles at substrate temperatures up to 905°C, around 70 degrees higher than in previous reports. Thus, we have overcome the next limitation of spontaneous GaN NW formation, the long incubation time usually preventing GaN NW formation at high substrate temperatures. At these temperatures, however, we observed that two additional effects quickly come into play. Both the onset of Si melt-back etching when growing on Si and GaN NW decomposition were discussed in detail.

Regarding the properties of these high-temperature NW ensembles, we demonstrated an outstanding optical quality with linewidths of the dominant donor-bound exciton transitions down to 0.4 meV. When comparing our samples to state-of-the-art free-standing GaN layers, we observed that in terms of linewidth and peak positions of the spectra, our high-temperature NW ensembles are quite comparable. As a matter of fact, in terms of intensity, the NW are even an order of magnitude brighter due to their enhanced light outcoupling. Supported by the excellent values of inhomogeneous strain determined from x-ray diffraction experiments, we can conclude that we can achieve a comparable materials quality when growing 2 µm long high temperature NW ensembles where for HVPE the fabrication of an 350 µm thick free-standing layer is required. Time-resolved measurements suggested, however, that our high-temperature NWs still possess a significantly higher point defect density compared to the free-standing GaN layer.

These findings will generate an increased interest in the fabrication of high-quality GaN NW ensembles. In addition, comparable growth approaches may be attempted for other material combinations. For (In,Ga)N NW segments or quantum disks, the use of comparable growth concepts to promote a higher growth temperature, may lead to an improved structural quality of the (In,Ga)N layer and affect the performance of (In,Ga)N/GaN NW LEDs. Analogously, the morphology and properties of (Al,Ga)N NWs in MBE can be drastically improved. (Al,Ga)N NWs usually suffer from a pronounced tapering during NW growth due to the limited diffusion of Al at standard GaN NW growth temperatures. Here, high-temperature growth of (Al,Ga)N NWs may lead to an enhanced Al diffusion and thereby an improved morphology with reduced tapering.

Furthermore, we for the first time demonstrated the spontaneous formation of GaN NWs also on SiC(000$\bar{1}$) both at conventional and high growth temperatures. In general, these samples behaved quite comparable to those on Si(111).

Finally, a post-growth decomposition step was introduced to tackle the limitations concerning the NW diameter and number density. Here, we demonstrated that we can reduce the diameters of the top parts of these NWs to well-below 10 nm in a process well-controlled by line-of-sight quadrupole mass spectroscopy. The activation energy we found for the decomposition of GaN NWs was in good agreement with previous reports for planar GaN layers. Using a comparably simple model of layer-by-layer decomposition, we managed to investigate and simulate the decomposition process of GaN NWs in detail. Analyzing the optical properties of the decomposed NW ensembles, we observed a clear blue shift of the donor-bound luminescence peak with diameter. Continuous wave and time resolved measurement of these ultrathin NWs yielded that these NWs remain very bright despite their low volume-to-surface ratio. Scaled by their volume, these NWs exhibit a more pronounced luminescence intensity, proving again, that the surface recombination in GaN is indeed negligible. As the Bohr radius in GaN is 3 nm, the observed confinement in the NWs is caused by dielectric confinement originating from the contrast in the dielectric constant of GaN and the surrounding material, i.e., vacuum or air. For the NWs presented here, this dielectric confinement acts like quantum confinement and works still at room temperature.

The reduction in the diameter of GaN NWs presented here will enable the realization of many interesting new device concepts. Using GaN/(Al,Ga)N or (In,Ga)N/GaN heterostructures, true quantum dots-in-a-wire may be formed. These structures are highly relevant for the development of single photon emitters that are required for quantum optics applications. The (In,Ga)N/GaN system would actually make possible single photon emitters across most of the visible spectrum and at all three telecom wavelengths 850 nm, 1310 nm, and 1550 nm.

Alternatively, the reduced diameter of the NWs can be utilized to enable Förster Resonant Energy Transfer from the NW to a suitable (organic) overlayer. For conventional NWs, this energy transfer does not work, because the electron is usually located at the center of the NW and the distance between the exciton and the surrounding organic shell is always larger than the critical 10 nm. Due to the reduced diameter of the ultrathin NW, however, this energy transfer should quickly become very efficient and facilitate the development of an hybrid inorganic/organic LED uniting the advantages of both inorganic and organic materials systems.

Summarizing, the here presented post-growth decomposition enabled the fabrication of ultrahin GaN nanowires that act as quantum wires. These results will generate a renewed interest in GaN NWs grown by MBE.

Last but not least, we also showed that a post-growth decomposition step, conducted for a longer time, eventually leads to a significant reduction in NW number density. Thereby, we also paved the way to overcome the fourth and final limitation of the spontaneous formation of GaN NWs in MBE. This reduction in density will, for example, allow the realization of GaN NW-based core-shell structures in MBE and thereby the realization of attractive alternative device architectures.

In conclusion, we have developed growth approaches to one-by-one overcome the fundamental limitations of the spontaneous formation of GaN NWs. With overcoming these limitations, we have fabricated NW ensembles with unprecedented properties concerning their diameter, excitonic linewidth and structural quality. Thereby, we have created new perspectives for the development of several new devices and device classes based on GaN NWs. In addition, the results presented here will also prove relevant also for other materials systems and growth approaches, e.g., the post-growth decomposition process can be easily transferred to selective-area-grow NWs.

There are a lot of new and interesting samples to be grown, measurements to be taken, studies to be performed, questions to be answered, and devices to be developed based on GaN nanowires.

A. Additional measurements

A.1. Rutherford backscattering spectrometry on ultrathin GaN nanowires

The measurements here presented were performed by Emanuel Schmidt and Carsten Ronning from the Institut für Festkörperphysik at the Friedrich-Schiller-University Jena.

As-grown and thermally decomposed GaN nanowires were investigated by Rutherford backscattering spectrometry (RBS). RBS measurements were performed with 2 MeV He-ions under 170 ° backscattering geometry using a standard passivated silicon particle detector with $\sim$ 4 msr solid angle. The ion charge was measured by a chopper wheel coated with a thin Au film and calibrated with a bulk lead glass standard. The samples were measured once with the incident ion beam orthogonal to the substrate surface and under varying "random" azimuthal angle 2 ° off the surface normal in order to avoid channeling effects of the substrate. Energy calibration of the detector was performed using a standard thin film sample containing various elements with well-distributed atomic masses.

The spectra of the random RBS measurements on as-grown and decomposed GaN nanowires are shown in Fig. A.1. The Ga signal starting at 1780 keV is clearly visible by the surface-edge in both RBS spectra. The signal of the silicon surface edge at 1280 keV is just visible in the spectrum of the sample with thermally decomposed nanowires. Due to the structure of the samples, the spectra are clearly distinct from what one would expect for a thin-film RBS measurement. The difference is caused by the statistical behavior of the energy loss of ions. In a thin film system, the energy loss of impinging ions is directly correlated to the energy loss of the ions on their way to the detector after the scattering process. In a structured material as nanowires, this correlation is disturbed and statistically distributed. Usually a correct calculation of a spectrum of an arbitrary structured sample can only be obtained by Monte-Carlo calculations[198]. However, the integrated signal of a film is in general not influenced by structural effects[199]. Thus, we can calculate the areal density of Ga atoms from the spectra by integrating the Ga signal over the concerning channels, as indicated in Fig. A.1. To compensate for the energy dependence of the Rutherford scattering cross-section, we calculate the RBS spectrum of a non-crystalline bulk GaN-sample and the ratio between the calculated yield over depth and the measured yield (not shown). The integration is performed from the energy of the ions scattered on the surface Ga atoms ($E_{0,Ga}$) to the energy of the backscattered ions on the Si surface ($E_{0,Si}$).
By integrating and comparing the spectra of the as-grown and the thermally decomposed nanowire ensembles it is possible to measure an areal density of Ga atoms of $(3.8 \pm 0.8 \times 10^{18})\,\mathrm{cm}^{-2}$ and $(1.45 \pm 0.3 \times 10^{17})\,\mathrm{cm}^{-2}$, respectively. Therefore, annealing a nanowire ensemble for 30 min at 920 °C in UHV leads to the decomposition of (96.2 ± 1.6)% of material. The uncertainties are calculated as the maximum possible deviations of the scattering cross-section of the He ions from the surface to the integrated depth. This

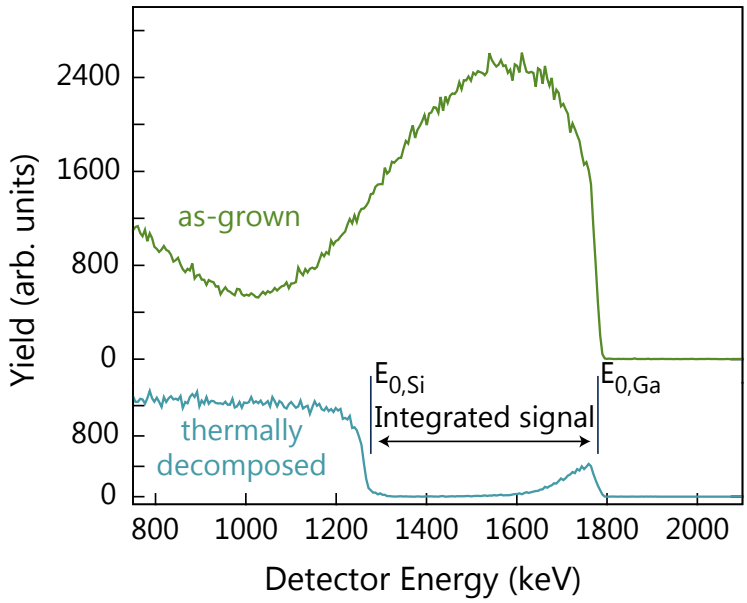

Figure A.1: RBS spectra of ultrathin GaN nanowires. Samples of GaN nanowires on crystalline Si-substrate as grown (top) and after thermal decomposition (bottom) were measured with 10 µC single charged 2 MeV He-ions in random orientation. The samples were tilted by 2 ° and rotated continuously during the measurement to prevent channeling effects of the Si-substrate. The energy of ions scattered on the surface of Ga ($E_{0,Ga}$) and Si ($E_{0,Si}$) is shown as well as the depth-scale of the ions scattered on Ga. The RBS measurement were carried out by Emanuel Schmidt and Carsten Ronning from the Friedrich-Schiller-University Jena.

is indicated by the systematic error affecting the concentration result by neglecting the nanowire structure.

B. List of samples

Sample number	Label	Substrate	Φ_N (nm/min)	Step	T_{sub} (°C)	Φ_{Ga} (nm/min)	Duration	Comments	Figures
M9926		Si(111)	14.2		820	5.0	5h		3.1
M9927		Si(111)	14.2		875	41.7	4h26m		3.1
M9930		Si(111)	14.2		820	5.0	5h	Ga-polishing	3.1
M9957	S875b	Si(111)	11.0		875	41.8	9h50m		5.9, 5.10, 5.11, 5.20, 5.28
M9959	S875	Si(111)	11.0		875	25.3	8h		3.1, 5.2, 5.3. 5.5–5.20, 5.26 5.28
M9960	A,S815	Si(111)	11.0		835	5.5	7h17m		5.1–5.35.5–5.7, 5.8,5.13 5.15, 5.16, 5.18–5.20,5.28
M9961	S835	Si(111)	11.0		815	5.5	4h24m		3.3, 3.6–3.8, 3.10, 4.1, 4.3–4.7 4.12, 4.14, 5.1–5.3, 5.5–5.7, 5.8 5.13–5.16, 5.18–5.20, 5.28
M9967	T875a	Si(111)	11.0	step 1	875	5.5	2h18m		5.9, 5.10, 5.20, 5.28
				step 2	875	25.3	4h25m		
M9968	T875b	Si(111)	11.0	step 1	875	4.0	3h40m		5.10, 5.20, 5.28
				step 2	875	10.0	4h10m		
M9969	C	Si(111)	11.0	step 1	815	5.0	1h05m		4.1–4.7
				step 2	845	5.0	3h20m		
M9972	B	Si(111)	11.0	step 1	815	5.0	1h20m		4.1–4.7
				step 2	845	5.0	3h05m		
M9973	D	Si(111)	11.0	step 1	815	5.0	50m		4.1, 4.3–4.7
				step 2	845	5.0	3h35m		
M9974	G	Si(111)	11.0	step 1	815	5.0	25m		4.12, 4.13
				step 2	845	5.0	4h		
M9975	H	Si(111)	11.0	step 1	815	5.0	25m		4.14, 4.15
				step 2	855	5.0	5h		
M9979		Si(111)	11.0	step 1	815	5.0	25m		2.7
				step 2	855	5.0	12h10m		
M9982	J	Si(111)	11.0	step 1	815	5.0	25m		4.14, 4.15
				step 2	855	5.0	8h		
M9992	S785	Si(111)	11.0		785	2.5	3h45m		5.2, 5.3, 5.5–5.7, 5.8 5.13, 5.15, 5.16, 5.18

Sample number	Label	Substrate	Φ_N (nm/min)	Step	T_{sub} ($^\circ$C)	Φ_{Ga} (nm/min)	Duration	Comments	Figures
M9993	E,S855	Si(111)	11.0		855	16.7	7h02m		4.8–4.11, 5.2, 5.3, 5.5–5.7 5.8, 5.13, 5.15, 5.16, 5.18 5.20, 5.28
M9995	F,T855	Si(111)	11.0	step 1	815	5.0	25m		4.8–4.11, 5.4, 5.15
				step 2	855	16.7	5h35m		
M91008	T905	Si(111)	11.0	step 1	815	5.0	25m	no rotation	5.4, 5.8
				step 2	905	35.2	8h46m		
M91015		AlN/Si(111)	11.0		905	41.7	3h	20 nm AlN buffer	5.9
M91019	A875	AlN/Si(111)	11.0		875	10.0	4h30m	26 nm AlN buffer	5.4–5.6, 5.13
M91036	C790	SiC(000$\bar{1}$)	11.0		790	3.9	5h15m		5.21–5.25
M91037	C810	SiC(000$\bar{1}$)	11.0		810	3.9	5h15m		5.21–5.25, 5.27, 5.28
M91039	C830	SiC(000$\bar{1}$)	11.0		830	7.9	5h15m		5.21–5.25, 5.27, 5.28
M91052	d_B=51	Si(111)	7.8	step 1	800	4.5	25m	no rotation	6.1, 6.8, 6.9
				step 2	810	4.5	3h35m		
M91060	d_B=39	Si(111)	7.8	step 1	800	4.5	25m	no rotation	6.1, 6.2, 6.4, 6.5, 6.8, 6.9
				step 2	819	4.5	3h35m		
				decomp.	920		30m		
M91067	$d_B \leq 32$	Si(111)	7.8	step 1	800	4.5	25m	no rotation, pieces with	6.8, 6.9
				step 2	810	4.5	3h35m	different d_B	
				decomp.	920		68m		
M91068	C850	SiC(000$\bar{1}$)	7.8		850	13.3	5h15m	no rotation	5.21–5.25, 5.27–5.29
M91072	D850a	SiC(000$\bar{1}$)	7.8		850	13.3	5h15m	no rotation, low Si doping	5.29
M91076	C870	SiC(000$\bar{1}$)	7.8	step 1	830	7.9	20m	no rotation	5.21–5.28
				step 2	870	16.7	5h		
M91077	D850b	SiC(000$\bar{1}$)	7.8		850	13.3	5h15m	no rotation, med Si doping	5.29
M91078		Si(111)	7.8	step 1	800	4.5	25m	no rotation	6.1, 6.10
				step 2	810	4.5	3h24m		
				decomp.	920		30m		

Bibliography

[1] H. Morkoç, *Handbook of Nitride Semiconductors and Devices, Materials Properties, Physics and Growth*. Wiley, 2009.

[2] S. Sze and K. Ng, *Physics of Semiconductor Devices*. Wiley, 2006.

[3] The Royal Swedish Academy of Sciences, "Press Release: The Nobel Prize in Physics 2014," http://www.nobelprize.org/nobel_prizes/physics/laureates/2014/press.html, 2014, accessed: 2015-08-09.

[4] J. R. Chelikowsky and M. L. Cohen, "Nonlocal pseudopotential calculations for the electronic structure of eleven diamond and zinc-blende semiconductors," *Phys. Rev. B*, vol. 14, no. 2, p. 556, 1976.

[5] A. A. Bergh and P. J. Dean, "Light-emitting diodes," *Oxford, Clarendon Press*, vol. 1, p. 598, 1976.

[6] H. Ibach and H. Lüth, *Solid-State Physics: An Introduction to Principles of Materials Science*, ser. Advanced texts in physics. Springer Berlin Heidelberg, 2009.

[7] H. Amano, N. Sawaki, I. Akasaki, and Y. Toyoda, "Metalorganic vapor phase epitaxial growth of a high quality GaN film using an AlN buffer layer," *Appl. Phys. Lett.*, vol. 48, no. 5, pp. 353–355, 1986.

[8] S. Nakamura, "GaN growth using GaN buffer layer," *Jpn. J. Appl. Phys.*, vol. 30, no. 10A, p. L1705, 1991.

[9] H. Amano, M. Kito, K. Hiramatsu, and I. Akasaki, "P-type conduction in Mg-doped GaN treated with low-energy electron beam irradiation (LEEBI)," *Jpn. J. Appl. Phys.*, vol. 28, no. 12A, p. L2112, 1989.

[10] S. Nakamura, T. Mukai, M. Senoh, and N. Iwasa, "Thermal annealing effects on p-type Mg-doped GaN films," *Jpn. J. Appl. Phys.*, vol. 31, no. 2B, p. L139, 1992.

[11] S. Nakamura, T. Mukai, and M. Senoh, "Candela-class high-brightness InGaN/AlGaN double-heterostructure blue-light-emitting diodes," *Appl. Phys. Lett.*, vol. 64, no. 13, pp. 1687–1689, 1994.

[12] Matsuoka Laboratory, Division of Electronic Materials Physics, IMR, Tohoku University, "Current Research Activities," http://www.matsuoka-lab.imr.tohoku.ac.jp/?TOPPAGE%2FRESEARCH_ENG, accessed: 2015-08-22.

[13] M. A. Moram and M. E. Vickers, "X-ray diffraction of III-nitrides," *Reports on Progress in Physics*, vol. 72, no. 3, p. 036502, 2009.

[14] P. Waltereit, O. Brandt, A. Trampert, H. T. Grahn, J. Menniger, M. Ramsteiner, M. Reiche, and K. H. Ploog, "Nitride semiconductors free of electrostatic fields for efficient white light-emitting diodes," *Nature*, vol. 406, no. 6798, pp. 865–868, 2000.

[15] W. B. Pearson, *A Handbook of Lattice Spacings and Structures of Metals and Alloys: International Series of Monographs on Metal Physics and Physical Metallurgy*. Elsevier, 2013, vol. 4.

[16] M. Leszczynski, H. Teisseyre, T. Suski, I. Grzegory, M. Bockowski, J. Jun, S. Porowski, K. Pakula, J. M. Baranowski, C. T. Foxon, and T. S. Cheng, "Lattice parameters of gallium nitride," *Appl. Phys. Lett.*, vol. 69, no. 1, p. 73, 1996.

[17] S. Bloom, G. Harbeke, E. Meier, and I. B. Ortenburger, "Band Structure and Reflectivity of GaN," *Phys. status solidi*, vol. 66, no. 1, pp. 161–168, 1974.

[18] C. G. Van de Walle and D. Segev, "Microscopic origins of surface states on nitride surfaces," *J. Appl. Phys.*, vol. 101, no. 8, p. 081704, 2007.

[19] M. Levinshtein, S. Rumyantsev, and M. Shur, *Properties of Advanced Semiconductor Materials: GaN, AIN, InN, BN, SiC, SiGe*. Wiley, 2001.

[20] R. Molnar, W. Götz, L. Romano, and N. Johnson, "Growth of gallium nitride by hydride vapor-phase epitaxy," *J. Cryst. Growth*, vol. 178, no. 1, pp. 147–156, 1997.

[21] P. Perlin, I. Gorczyca, N. Christensen, I. Grzegory, H. Teisseyre, and T. Suski, "Pressure studies of gallium nitride: Crystal growth and fundamental electronic properties," *Phys. Rev. B*, vol. 45, no. 23, p. 13307, 1992.

[22] D. R. Ketchum and J. W. Kolis, "Crystal growth of gallium nitride in supercritical ammonia," *J. Cryst. Growth*, vol. 222, no. 3, pp. 431–434, 2001.

[23] M. J. Cich, R. I. Aldaz, A. Chakraborty, A. David, M. J. Grundmann, A. Tyagi, M. Zhang, F. M. Steranka, and M. R. Krames, "Bulk GaN based violet light-emitting diodes with high efficiency at very high current density," *Appl. Phys. Lett.*, vol. 101, no. 22, p. 223509, 2012.

[24] M. Krames, O. Shchekin, R. Mueller-Mach, G. O. Mueller, L. Zhou, G. Harbers, and M. Craford, "Status and Future of High-Power Light-Emitting Diodes for Solid-State Lighting," *Display Technology, Journal of*, vol. 3, no. 2, pp. 160–175, 2007.

[25] J. Piprek, "LED droop: a critical review and novel solution," *Compd. Semicond*, vol. 20, pp. 44–48, 2014.

[26] D. J. Rogers, F. H. Teherani, P. Bove, R. McClintock, and M. Razeghi, "Improved LEDs and photovoltaics by hybridization and nanostructuring," *SPIE Newsroom*, vol. 10, no. 2.1201206, p. 004238, 2012.

[27] M.-H. Kim, M. F. Schubert, Q. Dai, J. K. Kim, E. F. Schubert, J. Piprek, and Y. Park, "Origin of efficiency droop in GaN-based light-emitting diodes," *Appl. Phys. Lett.*, vol. 91, no. 18, p. 183507, 2007.

[28] J. Piprek, "Efficiency droop in nitride-based light-emitting diodes," *Phys. status solidi*, vol. 207, no. 10, pp. 2217–2225, 2010.

[29] E. Kioupakis, P. Rinke, K. T. Delaney, and C. G. Van de Walle, "Indirect Auger recombination as a cause of efficiency droop in nitride light-emitting diodes," *Appl. Phys. Lett.*, vol. 98, no. 16, p. 161107, 2011.

[30] M. Binder, A. Nirschl, R. Zeisel, T. Hager, H.-J. Lugauer, M. Sabathil, D. Bougeard, J. Wagner, and B. Galler, "Identification of nnp and npp Auger recombination as significant contributor to the efficiency droop in (GaIn)N quantum wells by visualization of hot carriers in photoluminescence," *Appl. Phys. Lett.*, vol. 103, no. 7, p. 071108, 2013.

[31] A. Hangleiter, T. Langer, M. Gerhard, D. Kalincev, A. Kruse, H. Bremers, U. Rossow, and M. Koch, "Efficiency droop in nitride LEDs revisited: impact of excitonic recombination processes," *Proc. SPIE Gall. Nitride Mater. Devices X*, vol. 9363, p. 93631R, 2015.

[32] M. Kneissl, T. Kolbe, C. Chua, V. Kueller, N. Lobo, J. Stellmach, A. Knauer, H. Rodriguez, S. Einfeldt, Z. Yang, N. M. Johnson, and M. Weyers, "Advances in group III-nitride-based deep UV light-emitting diode technology," *Semicond. Sci. Technol.*, vol. 26, no. 1, p. 014036, 2011.

[33] K. Tomioka, J. Motohisa, S. Hara, and T. Fukui, "Control of InAs nanowire growth directions on Si." *Nano Lett.*, vol. 8, no. 10, pp. 3475–80, 2008.

[34] A. Urban, J. Malindretos, J.-H. Klein-Wiele, P. Simon, and A. Rizzi, "Ga-polar GaN nanocolumn arrays with semipolar faceted tips," *New J. Phys.*, vol. 15, no. 5, p. 053045, 2013.

[35] M. Yoshizawa, A. Kikuchi, M. Mori, N. Fujita, and K. Kishino, "Growth of Self-Organized GaN Nanostructures on Al_2O_3(0001) by RF-Radical Source Molecular Beam Epitaxy," *Jpn. J. Appl. Phys.*, vol. 36, no. Part 2, No. 4B, pp. L459–L462, 1997.

[36] E. Calleja, J. Ristić, S. Fernández-Garrido, L. Cerutti, M. A. Sánchez-García, J. Grandal, A. Trampert, U. Jahn, G. Sánchez, A. Griol, and B. Sánchez, "Growth, morphology, and structural properties of group-III-nitride nanocolumns and nanodisks," *Phys. status solidi*, vol. 244, no. 8, pp. 2816–2837, 2007.

[37] K. A. Bertness, N. A. Sanford, and A. V. Davydov, "GaN Nanowires Grown by Molecular Beam Epitaxy," *IEEE J. Sel. Top. Quantum Electron.*, vol. 17, no. 4, pp. 847–858, 2011.

[38] L. Geelhaar, C. Chéze, B. Jenichen, O. Brandt, C. Pfüller, S. Münch, R. Rothemund, S. Reitzenstein, A. Forchel, T. Kehagias, P. Komninou, G. P. Dimitrakopulos, T. Karakostas, L. Lari, P. R. Chalker, M. H. Gass, and H. Riechert, "Properties of GaN Nanowires Grown by Molecular Beam Epitaxy," *IEEE J. Sel. Top. Quantum Electron.*, vol. 17, no. 4, pp. 878–888, 2011.

[39] F. Schuster, F. Furtmayr, R. Zamani, C. Magén, J. R. Morante, J. Arbiol, J. A. Garrido, and M. Stutzmann, "Self-assembled GaN nanowires on diamond." *Nano Lett.*, vol. 12, no. 5, pp. 2199–204, 2012.

[40] M. Sobanska, K. Klosek, J. Borysiuk, S. Kret, G. Tchutchulasvili, S. Gieraltowska, and Z. R. Zytkiewicz, "Enhanced catalyst-free nucleation of GaN nanowires on amorphous Al_2O_3 by plasma-assisted molecular beam epitaxy," *J. Appl. Phys.*, vol. 115, no. 4, p. 043517, 2014.

[41] M. Wölz, C. Hauswald, T. Flissikowski, T. Gotschke, S. Fernández-Garrido, O. Brandt, H. T. Grahn, L. Geelhaar, and H. Riechert, "Epitaxial Growth of GaN Nanowires with High Structural Perfection on a Metallic TiN Film." *Nano Lett.*, vol. 15, no. 6, pp. 3743–3747, 2015.

[42] P. Corfdir, C. Hauswald, O. Marquardt, T. Flissikowski, J. K. Zettler, S. Fernández-Garrido, L. Geelhaar, H. T. Grahn, and O. Brandt, "Crystal-phase quantum dots in gan quantum wires," *Phys. Rev. B*, vol. 93, p. 115305, 2016.

[43] O. Brandt, C. Pfüller, C. Chèze, L. Geelhaar, and H. Riechert, "Sub-meV linewidth of excitonic luminescence in single GaN nanowires: Direct evidence for surface excitons," *Phys. Rev. B*, vol. 81, no. 4, p. 45302, 2010.

[44] P. Corfdir, P. Lefebvre, J. Ristić, P. Valvin, E. Calleja, A. Trampert, J.-D. Ganière, and B. Deveaud-Plédran, "Time-resolved spectroscopy on GaN nanocolumns grown by plasma assisted molecular beam epitaxy on Si substrates," *J. Appl. Phys.*, vol. 105, no. 1, p. 013113, 2009.

[45] O. Marquardt, C. Hauswald, M. Wölz, L. Geelhaar, and O. Brandt, "Luminous efficiency of axial $In_xGa_{1-x}N$/GaN nanowire heterostructures: interplay of polarization and surface potentials," *Nano Lett.*, vol. 13, no. 7, pp. 3298–3304, 2013.

[46] P. Deb, H. Kim, V. Rawat, M. Oliver, S. Kim, M. Marshall, E. Stach, and T. Sands, "Faceted and vertically aligned GaN nanorod arrays fabricated without catalysts or lithography," *Nano Lett.*, vol. 5, no. 9, pp. 1847–1851, 2005.

[47] S. D. Hersee, X. Sun, and X. Wang, "The controlled growth of GaN nanowires," *Nano Lett.*, vol. 6, no. 8, pp. 1808–1811, 2006.

[48] H.-M. Kim, D. Kim, Y. Park, D. Kim, T. Kang, and K. Chung, "Growth of GaN Nanorods by a Hydride Vapor Phase Epitaxy Method," *Adv. Mater.*, vol. 14, no. 13-14, pp. 991–993, 2002.

[49] M. A. Sánchez-García, E. Calleja, E. Monroy, F. Sanchez, F. Calle, E. Muñoz, and R. Beresford, "The effect of the III/V ratio and substrate temperature on the morphology and properties of GaN- and AlN-layers grown by molecular beam epitaxy on Si(111)," *J. Cryst. Growth*, vol. 183, no. 1-2, pp. 23–30, 1998.

[50] S. Fernández-Garrido, J. K. Zettler, L. Geelhaar, and O. Brandt, "Monitoring the formation of nanowires by line-of-sight quadrupole mass spectrometry: a comprehensive description of the temporal evolution of gan nanowire ensembles," *Nano letters*, vol. 15, no. 3, pp. 1930–1937, 2015.

[51] N. Newman, "The energetics of the GaN MBE reaction: a case study of meta-stable growth," *J. Cryst. Growth*, vol. 178, no. 1-2, pp. 102–112, 1997.

[52] B. Heying, R. Averbeck, L. F. Chen, E. Haus, H. Riechert, and J. S. Speck, "Control of GaN surface morphologies using plasma-assisted molecular beam epitaxy," *J. Appl. Phys.*, vol. 88, no. 4, p. 1855, 2000.

[53] T. Suzuki and Y. Hirabayashi, "First Observation of the Si(111) - 7×7 - 1×1 Phase Transition by the Optical Second Harmonic Generation," *Jpn. J. Appl. Phys.*, vol. 32, no. Part 2, No. 4B, pp. L610–L613, 1993.

[54] V. Consonni, M. Hanke, M. Knelangen, L. Geelhaar, A. Trampert, and H. Riechert, "Nucleation mechanisms of self-induced GaN nanowires grown on an amorphous interlayer," *Phys. Rev. B*, vol. 83, no. 3, p. 035310, 2011.

[55] V. Consonni, A. Trampert, L. Geelhaar, and H. Riechert, "Physical origin of the incubation time of self-induced GaN nanowires," *Appl. Phys. Lett.*, vol. 99, no. 3, p. 033102, 2011.

[56] O. Brandt, S. Fernández-Garrido, J. K. Zettler, E. Luna, U. Jahn, C. Chèze, and V. M. Kaganer, "Statistical Analysis of the Shape of One-Dimensional Nanostructures: Determining the Coalescence Degree of Spontaneously Formed GaN Nanowires," *Cryst. Growth Des.*, vol. 14, no. 5, pp. 2246–2253, 2014.

[57] V. Consonni, M. Knelangen, U. Jahn, A. Trampert, L. Geelhaar, and H. Riechert, "Effects of nanowire coalescence on their structural and optical properties on a local scale," *Appl. Phys. Lett.*, vol. 95, no. 24, p. 241910, 2009.

[58] A. Ichimiya, *Reflection high-energy electron diffraction*. Cambridge Univ. Press, 2010.

[59] W. Braun, *Applied RHEED: Reflection High-Energy Electron Diffraction During Crystal Growth*. Springer Berlin Heidelberg, 1999.

[60] C. Chèze, L. Geelhaar, O. Brandt, W. Weber, H. Riechert, S. Münch, R. Rothemund, S. Reitzenstein, A. Forchel, T. Kehagias, P. Komninou, G. Dimitrakopulos, and T. Karakostas, "Direct comparison of catalyst-free and catalyst-induced GaN nanowires," *Nano Res.*, vol. 3, no. 7, pp. 528–536, 2010.

[61] C. Chèze, L. Geelhaar, A. Trampert, and H. Riechert, "In situ investigation of self-induced GaN nanowire nucleation on Si," *Appl. Phys. Lett.*, vol. 97, no. 4, p. 43101, 2010.

[62] V. Consonni, M. Knelangen, L. Geelhaar, A. Trampert, and H. Riechert, "Nucleation mechanisms of epitaxial GaN nanowires: Origin of their self-induced formation and initial radius," *Phys. Rev. B*, vol. 81, no. 8, p. 085310, 2010.

[63] G. Koblmüller, R. Averbeck, H. Riechert, and P. Pongratz, "Direct observation of different equilibrium Ga adlayer coverages and their desorption kinetics on GaN (0001) and (000$\bar{1}$) surfaces," *Phys. Rev. B*, vol. 69, no. 3, p. 035325, 2004.

[64] J. S. Brown, G. Koblmüller, F. Wu, R. Averbeck, H. Riechert, and J. S. Speck, "Ga adsorbate on (0001) GaN: In situ characterization with quadrupole mass spectrometry and reflection high-energy electron diffraction," *J. Appl. Phys.*, vol. 99, no. 7, p. 074902, 2006.

[65] S. Fernández-Garrido, V. M. Kaganer, K. K. Sabelfeld, T. Gotschke, J. Grandal, E. Calleja, L. Geelhaar, and O. Brandt, "Self-Regulated Radius of Spontaneously Formed GaN Nanowires in Molecular Beam Epitaxy." *Nano Lett.*, vol. 13, no. 7, pp. 3274–3280, 2013.

[66] V. Consonni, "Self-induced growth of GaN nanowires by molecular beam epitaxy: A critical review of the formation mechanisms," *Phys. status solidi*, vol. 7, no. 10, pp. 699–712, 2013.

[67] J. Ristić, E. Calleja, S. Fernández-Garrido, L. Cerutti, A. Trampert, U. Jahn, and K. H. Ploog, "On the mechanisms of spontaneous growth of III-nitride nanocolumns by plasma-assisted molecular beam epitaxy," *J. Cryst. Growth*, vol. 310, no. 18, pp. 4035–4045, 2008.

[68] C. Foxon, J. Harvey, and B. Joyce, "The evaporation of GaAs under equilibrium and non-equilibrium conditions using a modulated beam technique," *J. Phys. Chem. Solids*, vol. 34, no. 10, pp. 1693 – 1701, 1973.

[69] B. Jenichen, O. Brandt, C. Pfüller, P. Dogan, M. Knelangen, and A. Trampert, "Macro- and micro-strain in GaN nanowires on Si(111)." *Nanotechnology*, vol. 22, no. 29, p. 295714, 2011.

[70] V. M. Kaganer, B. Jenichen, O. Brandt, S. Fernández-Garrido, P. Dogan, L. Geelhaar, and H. Riechert, "Inhomogeneous strain in GaN nanowires determined from x-ray diffraction peak profiles," *Phys. Rev. B*, vol. 86, no. 11, p. 115325, 2012.

[71] C. M. Park, Y. S. Park, H. Im, and T. W. Kang, "Optical properties of GaN nanorods grown by molecular-beam epitaxy; dependence on growth time." *Nanotechnology*, vol. 17, no. 4, pp. 952–5, 2006.

[72] C. A. Schneider, W. S. Rasband, and K. W. Eliceiri, "NIH Image to ImageJ: 25 years of image analysis," *Nat. Methods*, vol. 9, no. 7, pp. 671–675, 2012.

[73] V. Consonni, M. Knelangen, A. Trampert, L. Geelhaar, and H. Riechert, "Nucleation and coalescence effects on the density of self-induced GaN nanowires grown by molecular beam epitaxy," *Appl. Phys. Lett.*, vol. 98, no. 7, p. 071913, 2011.

[74] S. Fernández-Garrido, J. Grandal, E. Calleja, M. A. Sánchez-García, and D. Lopez-Romero, "A growth diagram for plasma-assisted molecular beam epitaxy of GaN nanocolumns on Si(111)," *J. Appl. Phys.*, vol. 106, no. 12, p. 126102, 2009.

[75] K. A. Grossklaus, A. Banerjee, S. Jahangir, P. Bhattacharya, and J. M. Millunchick, "Misorientation defects in coalesced self-catalyzed GaN nanowires," *J. Cryst. Growth*, vol. 371, pp. 142–147, 2013.

[76] S. Fernández-Garrido, V. M. Kaganer, C. Hauswald, B. Jenichen, M. Ramsteiner, V. Consonni, L. Geelhaar, and O. Brandt, "Correlation between the structural and optical properties of spontaneously formed GaN nanowires: a quantitative evaluation of the impact of nanowire coalescence," *Nanotechnology*, vol. 25, no. 45, p. 455702, 2014.

[77] E. Calleja, M. Sánchez-García, F. Sánchez, F. Calle, F. Naranjo, E. Muñoz, U. Jahn, and K. H. Ploog, "Luminescence properties and defects in GaN nanocolumns grown by molecular beam epitaxy," *Phys. Rev. B*, vol. 62, no. 24, pp. 16 826–16 834, 2000.

[78] P. Corfdir, F. Feix, J. K. Zettler, S. Fernández-Garrido, and O. Brandt, "Importance of the dielectric contrast for the polarization of excitonic transitions in single GaN nanowires," *New J. Phys.*, vol. 17, no. 3, p. 033040, 2015.

[79] C. Pfüller, O. Brandt, F. Grosse, T. Flissikowski, C. Chèze, V. Consonni, L. Geelhaar, H. T. Grahn, and H. Riechert, "Unpinning the Fermi level of GaN nanowires by ultraviolet radiation," *Phys. Rev. B*, vol. 82, no. 4, p. 45320, 2010.

[80] D. Sam-Giao, R. Mata, G. Tourbot, J. Renard, A. Wysmołek, B. Daudin, and B. Gayral, "Fine optical spectroscopy of the 3.45 eV emission line in GaN nanowires," *J. Appl. Phys.*, vol. 113, no. 4, p. 043102, 2013.

[81] P. Paskov, R. Schifano, B. Monemar, T. Paskova, S. Figge, and D. Hommel, "Emission properties of a-plane GaN grown by metal-organic chemical-vapor deposition," *J. Appl. Phys.*, vol. 98, no. 9, p. 093519, 2005.

[82] F. Furtmayr, M. Vielemeyer, M. Stutzmann, A. Laufer, B. K. Meyer, and M. Eickhoff, "Optical properties of Si- and Mg-doped gallium nitride nanowires grown by plasma-assisted molecular beam epitaxy," *J. Appl. Phys.*, vol. 104, no. 7, p. 74309, 2008.

[83] P. Lefebvre, S. Fernández-Garrido, J. Grandal, J. Ristić, M.-a. Sanchez-Garcia, and E. Calleja, "Radiative defects in GaN nanocolumns: Correlation with growth conditions and sample morphology," *Appl. Phys. Lett.*, vol. 98, no. 8, p. 083104, 2011.

[84] C. Hauswald, "Dynamics of free and bound excitons in GaN nanowires: Origin of the nonradiative recombination channel," Ph.D. dissertation, Humboldt-Universität zu Berlin, 2015.

[85] P. Corfdir, C. Hauswald, J. K. Zettler, T. Flissikowski, J. Lähnemann, S. Fernández-Garrido, L. Geelhaar, H. T. Grahn, and O. Brandt, "Stacking faults as quantum wells in nanowires: Density of states, oscillator strength, and radiative efficiency," *Phys. Rev. B*, vol. 90, no. 19, p. 195309, 2014.

[86] P. Corfdir, J. K. Zettler, C. Hauswald, S. Fernández-Garrido, O. Brandt, and P. Lefebvre, "Sub-meV linewidth in GaN nanowire ensembles: Absence of surface excitons due to the field ionization of donors," *Phys. Rev. B*, vol. 90, no. 20, p. 205301, 2014.

[87] C. Hauswald, P. Corfdir, J. K. Zettler, V. M. Kaganer, K. K. Sabelfeld, S. Fernández-Garrido, T. Flissikowski, V. Consonni, T. Gotschke, H. T. Grahn, L. Geelhaar, and O. Brandt, "Origin of the nonradiative decay of bound excitons in GaN nanowires," *Phys. Rev. B*, vol. 90, no. 16, p. 165304, 2014.

[88] W. K. Burton, N. Cabrera, and F. C. Frank, "The Growth of Crystals and the Equilibrium Structure of their Surfaces," *Philos. Trans. R. Soc. A Math. Phys. Eng. Sci.*, vol. 243, no. 866, pp. 299–358, 1951.

[89] A. Ishizaka and Y. Murata, "Crystal growth model for molecular beam epitaxy: Role of kinks on crystal growth," *J. Phys. Condens. Matter*, vol. 6, no. 45, pp. L693–L698, 1994.

[90] K. Harafuji, T. Tsuchiya, and K. Kawamura, "Molecular dynamics simulation for evaluating melting point of wurtzite-type GaN crystal," *J. Appl. Phys.*, vol. 96, no. 5, p. 2501, 2004.

[91] K. Naniwae, S. Itoh, H. Amano, K. Itoh, K. Hiramatsu, and I. Akasaki, "Growth of single crystal GaN substrate using hydride vapor phase epitaxy," *J. Cryst. Growth*, vol. 99, no. 1-4, pp. 381–384, 1990.

[92] O. Ambacher, "Growth and applications of Group III-nitrides," *J. Phys. D. Appl. Phys.*, vol. 31, no. 20, pp. 2653–2710, 1998.

[93] E. Richter, C. Hennig, M. Weyers, F. Habel, J.-D. Tsay, W.-Y. Liu, P. Brückner, F. Scholz, Y. Makarov, A. Segal, and J. Kaeppeler, "Reactor and growth process optimization for growth of thick GaN layers on sapphire substrates by HVPE," *J. Cryst. Growth*, vol. 277, no. 1-4, pp. 6–12, 2005.

[94] S. Porowski and I. Grzegory, "Thermodynamical properties of III-V nitrides and crystal growth of GaN at high N_2 pressure," *J. Cryst. Growth*, vol. 178, no. 1–2, pp. 174 – 188, 1997.

[95] S. Fernández-Garrido, G. Koblmüller, E. Calleja, and J. S. Speck, "In situ GaN decomposition analysis by quadrupole mass spectrometry and reflection high-energy electron diffraction," *J. Appl. Phys.*, vol. 104, no. 3, p. 33541, 2008.

[96] T. Zywietz, J. Neugebauer, and M. Scheffler, "Adatom diffusion at GaN (0001) and (000$\bar{1}$) surfaces," *Appl. Phys. Lett.*, vol. 73, no. 4, p. 487, 1998.

[97] C. Adelmann, J. Brault, G. Mula, B. Daudin, L. Lymperakis, and J. Neugebauer, "Gallium adsorption on (0001) GaN surfaces," *Phys. Rev. B*, vol. 67, no. 16, pp. 1–9, 2003.

[98] G. Koblmüller, S. Fernández-Garrido, E. Calleja, and J. S. Speck, "In situ investigation of growth modes during plasma-assisted molecular beam epitaxy of (0001) GaN," *Appl. Phys. Lett.*, vol. 91, no. 16, p. 161904, 2007.

[99] C. Adelmann, J. Brault, D. Jalabert, P. Gentile, H. Mariette, G. Mula, and B. Daudin, "Dynamically stable gallium surface coverages during plasma-assisted molecular-beam epitaxy of (0001) GaN," *J. Appl. Phys.*, vol. 91, no. 12, pp. 9638–9645, 2002.

[100] C. Chèze, L. Geelhaar, A. Trampert, O. Brandt, and H. Riechert, "Collector phase transitions during vapor-solid-solid nucleation of GaN nanowires." *Nano Lett.*, vol. 10, no. 9, pp. 3426–31, 2010.

[101] L. Geelhaar, C. Chèze, W. M. Weber, R. Averbeck, H. Riechert, T. Kehagias, P. Komninou, G. P. Dimitrakopulos, and T. Karakostas, "Axial and radial growth of Ni-induced GaN nanowires," *Appl. Phys. Lett.*, vol. 91, no. 9, p. 093113, 2007.

[102] K. Kishino, T. Hoshino, S. Ishizawa, and A. Kikuchi, "Selective-area growth of GaN nanocolumns on titanium-mask-patterned silicon (111) substrates by RF-plasma-assisted molecular-beam epitaxy," *Electron. Lett.*, vol. 44, no. 13, pp. 819–821, 2008.

[103] K. Kishino, H. Sekiguchi, and A. Kikuchi, "Improved Ti-mask selective-area growth (SAG) by rf-plasma-assisted molecular beam epitaxy demonstrating extremely uniform GaN nanocolumn arrays," *J. Cryst. Growth*, vol. 311, no. 7, pp. 2063–2068, 2009.

[104] T. Schumann, T. Gotschke, F. Limbach, T. Stoica, and R. Calarco, "Selective-area catalyst-free MBE growth of GaN nanowires using a patterned oxide layer." *Nanotechnology*, vol. 22, no. 9, p. 095603, 2011.

[105] T. Gotschke, T. Schumann, F. Limbach, T. Stoica, and R. Calarco, "Influence of the adatom diffusion on selective growth of GaN nanowire regular arrays," *Appl. Phys. Lett.*, vol. 98, no. 10, p. 103102, 2011.

[106] F. Schuster, M. Hetzl, S. Weiszer, J. A. Garrido, M. de la Mata, C. Magen, J. Arbiol, and M. Stutzmann, "Position-Controlled Growth of GaN Nanowires and Nanotubes on Diamond by Molecular Beam Epitaxy," *Nano Lett.*, vol. ASAP, 2015.

[107] R. K. Debnath, R. J. Meijers, T. Richter, T. Stoica, R. Calarco, and H. Lüth, "Mechanism of molecular beam epitaxy growth of GaN nanowires on Si(111)," *Appl. Phys. Lett.*, vol. 90, no. 12, p. 123117, 2007.

[108] C. T. Foxon, S. Novikov, J. Hall, R. Campion, D. Cherns, I. Griffiths, and S. Khongphetsak, "A complementary geometric model for the growth of GaN nanocolumns prepared by plasma-assisted molecular beam epitaxy," *J. Cryst. Growth*, vol. 311, no. 13, pp. 3423–3427, 2009.

[109] L. Lymperakis and J. Neugebauer, "Large anisotropic adatom kinetics on nonpolar GaN surfaces: Consequences for surface morphologies and nanowire growth," *Phys. Rev. B*, vol. 79, no. 24, pp. 1–4, 2009.

[110] H. Li, L. Geelhaar, H. Riechert, and C. Draxl, "Computing Equilibrium Shapes of Wurtzite Crystals: The Example of GaN," *Phys. Rev. Lett.*, vol. 115, p. 085503, 2015.

[111] R. Calarco, R. J. Meijers, R. K. Debnath, T. Stoica, E. Sutter, and H. Lüth, "Nucleation and growth of GaN nanowires on Si(111) performed by molecular beam epitaxy." *Nano Lett.*, vol. 7, no. 8, pp. 2248–51, 2007.

[112] T. Stoica, E. Sutter, R. J. Meijers, R. K. Debnath, R. Calarco, H. Lüth, and D. Grützmacher, "Interface and wetting layer effect on the catalyst-free nucleation and growth of GaN nanowires." *Small*, vol. 4, no. 6, pp. 751–4, 2008.

[113] V. Consonni, V. G. Dubrovskii, A. Trampert, L. Geelhaar, and H. Riechert, "Quantitative description for the growth rate of self-induced GaN nanowires," *Phys. Rev. B*, vol. 85, no. 15, p. 155313, 2012.

[114] K. Hestroffer, C. Leclere, C. Bougerol, H. Renevier, and B. Daudin, "Polarity of GaN nanowires grown by plasma-assisted molecular beam epitaxy on Si(111)," *Phys. Rev. B*, vol. 84, no. 24, p. 245302, 2011.

[115] K. A. Bertness, N. A. Sanford, J. M. Barker, J. B. Schlager, A. Roshko, a. V. Davydov, and I. Levin, "Catalyst-free growth of GaN nanowires," *J. Electron. Mater.*, vol. 35, no. 4, pp. 576–580, 2006.

[116] L. Largeau, D. L. Dheeraj, M. Tchernycheva, G. E. Cirlin, and J.-C. Harmand, "Facet and in-plane crystallographic orientations of GaN nanowires grown on Si(111)," *Nanotechnology*, vol. 19, no. 15, p. 155704, 2008.

[117] A. Trampert, J. Ristić, U. Jahn, E. Calleja, and K. Ploog, "TEM study of (Ga, Al) N nanocolumns and embedded GaN nanodiscs," in *IOP Conf. Ser. No. 180*, vol. 167, no. 180, 2003, p. 167.

[118] X. Kong, J. Ristić, M. A. Sanchez-Garcia, E. Calleja, and A. Trampert, "Polarity determination by electron energy-loss spectroscopy: application to ultra-small III-nitride semiconductor nanocolumns." *Nanotechnology*, vol. 22, no. 41, p. 415701, 2011.

[119] S. D. Carnevale, T. F. Kent, P. J. Phillips, A. T. M. G. Sarwar, C. Selcu, R. F. Klie, and R. C. Myers, "Mixed Polarity in Polarization-Induced pn Junction Nanowire Light Emitting Diodes." *Nano Lett.*, vol. 13, no. 7, pp. 3029–3035, 2013.

[120] S. Fernández-Garrido, X. Kong, T. Gotschke, R. Calarco, L. Geelhaar, A. Trampert, and O. Brandt, "Spontaneous Nucleation and Growth of GaN Nanowires: The Fundamental Role of Crystal Polarity." *Nano Lett.*, vol. 12, no. 12, pp. 6119–6125, 2012.

[121] M. Stutzmann, O. Ambacher, M. Eickhoff, U. Karrer, a. Lima Pimenta, R. Neuberger, J. Schalwig, R. Dimitrov, P. Schuck, and R. Grober, "Playing with Polarity," *Phys. status solidi*, vol. 228, no. 2, pp. 505–512, 2001.

[122] X. Wang and A. Yoshikawa, "Molecular beam epitaxy growth of GaN, AlN and InN," *Prog. Cryst. Growth Charact. Mater.*, vol. 48-49, pp. 42–103, 2004.

[123] F. Fossard, J. Brault, N. Gogneau, E. Monroy, F. Enjalbert, L. S. Dang, E. Bellet-Amalric, S. Monnoye, H. Mank, and B. Daudin, "Direct Growth of High Quality GaN by Plasma Assisted Molecular Beam Epitaxy on 4H-SiC Substrates," *Mater. Sci. Forum*, vol. 457-460, pp. 1577–1580, 2004.

[124] O. Romanyuk, S. Fernández-Garrido, P. Jiríček, I. Bartoš, L. Geelhaar, O. Brandt, and T. Paskova, "Non-destructive assessment of the polarity of GaN nanowire ensembles using low-energy electron diffraction and x-ray photoelectron diffraction," *Appl. Phys. Lett.*, vol. 106, p. 021602, 2015.

[125] K. K. Sabelfeld, V. M. Kaganer, F. Limbach, P. Dogan, O. Brandt, L. Geelhaar, and H. Riechert, "Height self-equilibration during the growth of dense nanowire ensembles: Order emerging from disorder," *Appl. Phys. Lett.*, vol. 103, no. 13, p. 133105, 2013.

[126] S. D. Hersee, A. K. Rishinaramangalam, M. N. Fairchild, L. Zhang, and P. Varangis, "Threading defect elimination in GaN nanowires," *J. Mater. Res.*, vol. 26, no. 17, pp. 2293–2298, 2011.

[127] A. Das, J. Heo, M. Jankowski, W. Guo, L. Zhang, H. Deng, and P. Bhattacharya, "Room Temperature Ultralow Threshold GaN Nanowire Polariton Laser," *Phys. Rev. Lett.*, vol. 107, no. 6, p. 66405, 2011.

[128] B. Monemar, P. Paskov, J. P. Bergman, G. Pozina, a. a. Toropov, T. V. Shubina, T. Malinauskas, and A. Usui, "Transient photoluminescence of shallow donor bound excitons in GaN," *Phys. Rev. B*, vol. 82, no. 23, p. 235202, 2010.

[129] B. Monemar, P. Paskov, J. P. Bergman, a. a. Toropov, T. V. Shubina, T. Malinauskas, and a. Usui, "Recombination of free and bound excitons in GaN," *Phys. status solidi*, vol. 245, no. 9, pp. 1723–1740, 2008.

[130] V. G. Dubrovskii, V. Consonni, L. Geelhaar, A. Trampert, and H. Riechert, "Scaling growth kinetics of self-induced GaN nanowires," *Appl. Phys. Lett.*, vol. 100, no. 15, p. 153101, 2012.

[131] V. G. Dubrovskii, V. Consonni, A. Trampert, L. Geelhaar, and H. Riechert, "Scaling thermodynamic model for the self-induced nucleation of GaN nanowires," *Phys. Rev. B*, vol. 85, no. 16, p. 165317, 2012.

[132] J. W. Yoon, T. Sasaki, C. H. Roh, S. H. Shim, K. B. Shim, and N. Koshizaki, "Quantum confinement effect of nanocrystalline GaN films prepared by pulsed-laser ablation under various Ar pressures," *Thin Solid Films*, vol. 471, pp. 273–276, 2005.

[133] S. D. Carnevale, J. Yang, P. J. Phillips, M. J. Mills, and R. C. Myers, "Three-dimensional GaN/AlN nanowire heterostructures by separating nucleation and growth processes." *Nano Lett.*, vol. 11, no. 2, pp. 866–71, 2011.

[134] J. K. Zettler, C. Hauswald, P. Corfdir, M. Musolino, L. Geelhaar, H. Riechert, O. Brandt, and S. Fernández-Garrido, "High-Temperature Growth of GaN Nanowires by Molecular Beam Epitaxy: Toward the Material Quality of Bulk GaN," *Cryst. Growth Des.*, vol. 15, no. 8, pp. 4104–4109, 2015.

[135] J. K. Zettler, P. Corfdir, L. Geelhaar, H. Riechert, O. Brandt, and S. Fern?ndez-Garrido, "Improved control over spontaneously formed GaN nanowires in molecular beam epitaxy using a two-step growth process," *Nanotechnology*, vol. 26, no. 44, p. 445604, 2015.

[136] R. Songmuang, O. Landré, and B. Daudin, "From nucleation to growth of catalyst-free GaN nanowires on thin AlN buffer layer," *Appl. Phys. Lett.*, vol. 91, no. 25, p. 251902, 2007.

[137] M. Tchernycheva, C. Sartel, G. E. Cirlin, L. Travers, G. Patriarche, J.-C. Harmand, L. S. Dang, J. Renard, B. Gayral, L. Nevou, and F. Julien, "Growth of GaN free-standing nanowires by plasma-assisted molecular beam epitaxy: structural and optical characterization," *Nanotechnology*, vol. 18, no. 38, p. 385306, 2007.

[138] O. Landré, R. Songmuang, J. Renard, E. Bellet-Amalric, H. Renevier, and B. Daudin, "Plasma-assisted molecular beam epitaxy growth of GaN nanowires using indium-enhanced diffusion," *Appl. Phys. Lett.*, vol. 93, no. 18, p. 183109, 2008.

[139] R. Songmuang, T. Ben, B. Daudin, D. González, and E. Monroy, "Identification of III-N nanowire growth kinetics via a marker technique." *Nanotechnology*, vol. 21, no. 29, p. 295605, 2010.

[140] F. Schuster, S. Weiszer, M. Hetzl, A. Winnerl, J. A. Garrido, and M. Stutzmann, "Influence of substrate material, orientation, and surface termination on GaN nanowire growth," *J. Appl. Phys.*, vol. 116, no. 5, p. 054301, 2014.

[141] Z. Sun, D. Wang, and J. Xiang, "Self-bridging of vertical silicon nanowires and a universal capacitive force model for spontaneous attraction in nanostructures." *ACS Nano*, vol. 8, no. 11, pp. 11 261–7, 2014.

[142] J. J. Hill, K. Haller, B. Gelfand, and K. J. Ziegler, "Eliminating Capillary Coalescence of Nanowire Arrays with Applied Electric Fields," *ACS Appl. Mater. Interfaces*, vol. 2, no. 7, pp. 1992–1998, 2010.

[143] D. Zhu, D. J. Wallis, and C. J. Humphreys, "Prospects of III-nitride optoelectronics grown on Si." *Rep. Prog. Phys.*, vol. 76, no. 10, p. 106501, 2013.

[144] K. A. Bertness, A. W. Sanders, D. M. Rourke, T. E. Harvey, A. Roshko, J. B. Schlager, and N. A. Sanford, "Controlled Nucleation of GaN Nanowires Grown with Molecular Beam Epitaxy," *Adv. Funct. Mater.*, vol. 20, no. 17, pp. 2911–2915, 2010.

[145] M. Musolino, A. Tahraoui, S. Fernández-Garrido, O. Brandt, A. Trampert, L. Geelhaar, and H. Riechert, "Compatibility of the selective area growth of GaN nanowires on AlN-buffered Si substrates with the operation of light emitting diodes," *Nanotechnology*, vol. 26, p. 085605, 2015.

[146] K. Kornitzer, T. Ebner, K. Thonke, R. Sauer, C. Kirchner, V. Schwegler, M. Kamp, M. Leszczynski, I. Grzegory, and S. Porowski, "Photoluminescence and reflectance spectroscopy of excitonic transitions in high-quality homoepitaxial GaN films," *Phys. Rev. B*, vol. 60, no. 3, pp. 1471–1473, 1999.

[147] A. Wysmołek, K. Korona, R. Stępniewski, J. Baranowski, J. Bloniarz, M. Potemski, R. Jones, D. Look, J. Kuhl, S. Park, and S. Lee, "Recombination of excitons bound to oxygen and silicon donors in freestanding GaN," *Phys. Rev. B*, vol. 66, no. 24, p. 245317, 2002.

[148] T. Auzelle, B. Haas, M. Den Hertog, J.-L. Rouvière, B. Daudin, and B. Gayral, "Attribution of the 3.45 eV GaN nanowires luminescence to inversion domain boundaries," *Appl. Phys. Lett.*, vol. 107, no. 5, p. 051904, 2015.

[149] J. Lähnemann, O. Brandt, U. Jahn, C. Roder, P. Dogan, F. Grosse, A. Belabbes, F. Bechstedt, A. Trampert, L. Geelhaar, and C. Pfüller, "Direct experimental determination of the spontaneous polarization of GaN," *Phys. Rev. B*, vol. 86, no. 8, p. 081302, 2012.

[150] T. Gühne, Z. Bougrioua, S. Laügt, M. Nemoz, P. Vennéguès, B. Vinter, and M. Leroux, "Band-edge photoluminescence and reflectivity of nonpolar $(11\bar{2}0)$ and semipolar $(11\bar{2}2)$ GaN formed by epitaxial lateral overgrowth on sapphire," *Phys. Rev. B*, vol. 77, no. 7, p. 075308, 2008.

[151] L. H. Robins, K. A. Bertness, J. M. Barker, N. A. Sanford, and J. B. Schlager, "Optical and structural study of GaN nanowires grown by catalyst-free molecular beam epitaxy. I. Near-band-edge luminescence and strain effects," *J. Appl. Phys.*, vol. 101, no. 11, p. 113505, 2007.

[152] P. Dogan, O. Brandt, C. Pfüller, A.-K. Bluhm, L. Geelhaar, and H. Riechert, "GaN nanowire templates for the pendeoepitaxial coalescence overgrowth on Si(111) by molecular beam epitaxy," *J. Cryst. Growth*, vol. 323, no. 1, pp. 418–421, 2011.

[153] J. A. Chisholm and P. D. Bristowe, "Stacking fault energies in Si doped GaN: A first principles study," *Appl. Phys. Lett.*, vol. 77, no. 4, p. 534, 2000.

[154] C. Kirchner, V. Schwegler, F. Eberhard, M. Kamp, K. J. Ebeling, K. P. Korona, T. Ebner, K. Thonke, R. Sauer, P. Prystawko, M. Leszczynski, I. Grzegory, and S. Porowski, "Homoepitaxial growth of GaN by metalorganic vapor phase epitaxy: A benchmark for GaN technology," *Appl. Phys. Lett.*, vol. 75, no. 8, p. 1098, 1999.

[155] Y. S. Park, T. W. Kang, H. Im, S.-K. Lee, Y.-H. Cho, C. M. Park, M.-S. Han, and R. A. Taylor, "Effects of Surface Recombination on Exciton Dynamics in GaN Nanorods," *J. Nanoelectron. Optoelectron.*, vol. 4, pp. 307–311(5), 2009.

[156] Y. S. Park, H. Im, I. T. Yoon, S.-K. Lee, Y.-H. Cho, and R. A. Taylor, "Micro- and Time-resolved Photoluminescence in GaN Nanorods with Different Diameters," *J. Korean Phys. Soc.*, vol. 57, no. 4, p. 756, 2010.

[157] A. Gorgis, T. Flissikowski, O. Brandt, C. Chèze, L. Geelhaar, H. Riechert, and H. Grahn, "Time-resolved photoluminescence spectroscopy of individual GaN nanowires," *Phys. Rev. B*, vol. 86, no. 4, p. 041302(R), 2012.

[158] C. Hauswald, T. Flissikowski, T. Gotschke, R. Calarco, L. Geelhaar, H. T. Grahn, and O. Brandt, "Coupling of exciton states as the origin of their biexponential decay dynamics in GaN nanowires," *Phys. Rev. B*, vol. 88, no. 7, p. 075312, 2013.

[159] C. Hauswald, T. Flissikowski, H. T. Grahn, L. Geelhaar, H. Riechert, and O. Brandt, "Radiative and nonradiative decay of excitons in GaN nanowires," in *Proc. SPIE Gall. Nitride Mater. Devices IX*, J.-I. Chyi, Y. Nanishi, H. Morkoç, J. Piprek, E. Yoon, and H. Fujioka, Eds., vol. 8986, 2014, p. 89860V.

[160] D. Kage, "Time-resolved photoluminescence studies on inorganic-organic hybrid systems based on GaN nanowires," Master's thesis, Humboldt-Universität zu Berlin, 2015.

[161] S. Fan, S. Zhao, X. Liu, and Z. Mi, "Study on the coalescence of dislocation-free GaN nanowires on Si and SiOx," *J. Vac. Sci. Technol. B Microelectron. Nanom. Struct.*, vol. 32, no. 2, p. 02C114, 2014.

[162] S. Ghosh, P. Waltereit, O. Brandt, H. Grahn, and K. Ploog, "Electronic band structure of wurtzite GaN under biaxial strain in the M plane investigated with photoreflectance spectroscopy," *Phys. Rev. B*, vol. 65, no. 7, p. 075202, 2002.

[163] L. V. Keldysh, "Coulomb interaction in thin semiconductor and semimetal films," *J. Exp. Theor. Phys. Lett.*, vol. 29, p. 658, 1979.

[164] M. Kumagai and T. Takagahara, "Excitonic and nonlinear-optical properties of dielectric quantum-well structures," *Phys. Rev. B*, vol. 40, pp. 12 359–12 381, 1989.

[165] D. B. Tran Thoai, R. Zimmermann, M. Grundmann, and D. Bimberg, "Image charges in semiconductor quantum wells: Effect on exciton binding energy," *Phys. Rev. B*, vol. 42, pp. 5906–5909, 1990.

[166] E. A. Muljarov, E. A. Zhukov, V. S. Dneprovskii, and Y. Masumoto, "Dielectrically enhanced excitons in semiconductor-insulator quantum wires: Theory and experiment," *Phys. Rev. B*, vol. 62, no. 11, pp. 7420–7432, 2000.

[167] A. F. Slachmuylders, B. Partoens, W. Magnus, and F. M. Peeters, "Dielectric mismatch effect on the exciton states in cylindrical nanowires," *Phys. Rev. B*, vol. 74, pp. 1–8, 2006.

[168] S. Christopoulos, G. B. H. von Högersthal, A. J. D. Grundy, P. G. Lagoudakis, A. V. Kavokin, J. J. Baumberg, G. Christmann, R. Butté, E. Feltin, J.-F. Carlin, and N. Grandjean, "Room-Temperature Polariton Lasing in Semiconductor Microcavities," *Phys. Rev. Lett.*, vol. 98, p. 126405, 2007.

[169] G. Grosso, J. Graves, A. T. Hammack, A. A. High, L. V. Butov, M. Hanson, and A. C. Gossard, "Excitonic switches operating at around 100 K," *Nat. Photonics*, vol. 3, p. 577, 2009.

[170] T. K. Paraïso, M. Wouters, Y. Léger, F. Morier-Genoud, and B. Deveaud-Plédran, "Multistability of a coherent spin ensemble in a semiconductor microcavity," *Nat. Mater.*, vol. 9, p. 655, 2010.

[171] P. Cristofolini, G. Christmann, S. I. Tsintzos, G. Deligeorgis, G. Konstantinidis, Z. Hatzopoulos, P. G. Savvidis, and J. J. Baumberg, "Coupling Quantum Tunneling with Cavity Photons," *Science*, vol. 336, no. 6082, pp. 704–707, 2012.

[172] H. S. Nguyen, D. Vishnevsky, C. Sturm, D. Tanese, D. Solnyshkov, E. Galopin, A. Lemaître, I. Sagnes, A. Amo, G. Malpuech, and J. Bloch, "Realization of a Double-Barrier Resonant Tunneling Diode for Cavity Polaritons," *Phys. Rev. Lett.*, vol. 110, p. 236601, 2013.

[173] N. A. Gippius, A. L. Yablonskii, A. B. Dzyubenko, S. G. Tikhodeev, L. V. Kulik, V. D. Kulakovskii, and A. Forchel, "Excitons in near-surface quantum wells in magnetic fields: Experiment and theory," *J. Appl. Phys.*, vol. 83, no. 10, pp. 5410–5417, 1998.

[174] H. J. Joyce, C. J. Docherty, Q. Gao, H. H. Tan, C. Jagadish, J. Lloyd-Hughes, L. M. Herz, and M. B. Johnston, "Electronic properties of GaAs, InAs and InP nanowires studied by terahertz spectroscopy," *Nanotechnology*, vol. 24, no. 21, p. 214006, 2013.

[175] O. Demichel, M. Heiss, J. Bleuse, H. Mariette, and A. Fontcuberta i Morral, "Impact of surfaces on the optical properties of GaAs nanowires," *Appl. Phys. Lett.*, vol. 97, no. 20, p. 201907, 2010.

[176] S. Breuer, C. Pfüller, T. Flissikowski, O. Brandt, H. T. Grahn, L. Geelhaar, and H. Riechert, "Suitability of Au- and self-assisted GaAs nanowires for optoelectronic applications," *Nano Lett.*, vol. 11, no. 3, pp. 1276–1279, 2011.

[177] L. C. Andreani and A. Pasquarello, "Accurate theory of excitons in GaAs-$Ga_{1-x}Al_xAs$ quantum wells," *Phys. Rev. B*, vol. 42, pp. 8928–8938, 1990.

[178] S. Chu, G. Wang, W. Zhou, Y. Lin, L. Chernyak, J. Zhao, J. Kong, L. Li, J. Ren, and J. Liu, "Electrically pumped waveguide lasing from ZnO nanowires," *Nat. Nanotechnol.*, vol. 6, no. 8, pp. 506–510, 2011.

[179] G. Goldoni, F. Rossi, and E. Molinari, "Strong Exciton Binding in Quantum Structures through Remote Dielectric Confinement," *Phys. Rev. Lett.*, vol. 80, pp. 4995–4998, 1998.

[180] S. F. Chichibu, A. Uedono, T. Onuma, B. A. Haskell, A. Chakraborty, T. Koyama, P. T. Fini, S. Keller, S. P. DenBaars, J. S. Speck, U. K. Mishra, S. Nakamura, S. Yamaguchi, S. Kamiyama, H. Amano, I. Akasaki, J. Han, and T. Sota, "Origin of defect-insensitive emission probability in In-containing (Al,In,Ga)N alloy semiconductors." *Nat. Mater.*, vol. 5, no. 10, pp. 810–6, 2006.

[181] D. Segev and C. Van de Walle, "Electronic structure of nitride surfaces," *J. Cryst. Growth*, vol. 300, no. 1, pp. 199–203, 2007.

[182] D. J. Wolford, G. D. Gilliland, T. F. Kuech, J. F. Klem, H. P. Hjalmarson, J. A. Bradley, C. F. Tsang, and J. Martinsen, "Comparison of transport, recombination, and interfacial quality in molecular beam epitaxy and organometallic vaporn phase epitaxy $GaAs/Al_xGa_1a_{1-x}As$ structures," *Appl. Phys. Lett.*, vol. 64, no. 11, pp. 1416–1418, 1994.

[183] B. Loitsch, D. Rudolph, S. Morkötter, M. Döblinger, G. Grimaldi, L. Hanschke, S. Matich, E. Parzinger, U. Wurstbauer, G. Abstreiter, J. J. Finley, and G. Koblmüller, "Tunable Quantum Confinement in Ultrathin, Optically Active Semiconductor Nanowires Via Reverse-Reaction Growth," *Adv. Mater.*, pp. 2195–2202, 2015.

[184] L. Brockway, C. Pendyala, J. Jasinski, M. K. Sunkara, and S. Vaddiraju, "A postsynthesis decomposition strategy for group III-nitride quantum wires," *Cryst. Growth Des.*, vol. 11, pp. 4559–4564, 2011.

[185] J. K. Zettler, P. Corfdir, C. Hauswald, E. Luna, U. Jahn, T. Flissikowski, E. Schmidt, C. Ronning, A. Trampert, L. Geelhaar, H. T. Grahn, O. Brandt, and S. Fernández-Garrido, "Observation of Dielectrically Confined Excitons in Ultrathin GaN Nanowires up to Room Temperature," *Nano Letters*, vol. 16, no. 2, pp. 973–980, 2016.

[186] M. T. Björk, H. Schmid, J. Knoch, H. Riel, and W. Riess, "Donor deactivation in silicon nanostructures," *Nat. Nanotechnol.*, vol. 4, no. February, pp. 103–107, 2009.

[187] P. Corfdir and P. Lefebvre, "Role of the dielectric mismatch on the properties of donors in semiconductor nanostructures bounded by air," *J. Appl. Phys.*, vol. 112, no. 10, p. 106104, 2012.

[188] A. Trampert, J. Ristić, U. Jahn, E. Calleja, and K. Ploog, "TEM study of (Ga, Al) N nanocolumns and embedded GaN nanodiscs," *IOP Conf. Ser.*, vol. 180, p. 167, 2003.

[189] R. Held, D. E. Crawford, a. M. Johnston, a. M. Dabiran, and P. I. Cohen, "N-limited versus Ga-limited growth on GaN(000$\bar{1}$) by MBE using NH3," *Surf. Rev. Lett.*, vol. 5, no. 3-4, pp. 913–934, 1998.

[190] N. Grandjean, J. Massies, F. Semond, S. Y. Karpov, and R. a. Talalaev, "GaN evaporation in molecular-beam epitaxy environment," *Appl. Phys. Lett.*, vol. 74, no. 13, p. 1854, 1999.

[191] J. Wang, M. S. Gudiksen, X. Duan, Y. Cui, and C. M. Lieber, "Highly polarized photoluminescence and photodetection from single indium phosphide nanowires." *Science*, vol. 293, no. 5534, pp. 1455–7, 2001.

[192] D. S. Citrin, "Radiative lifetimes of excitons in quantum wells: Localization and phase-coherence effects," *Phys. Rev. B*, vol. 47, no. 23, pp. 3832–3841, 1993.

[193] D. S. Citrin, "Long intrinsic radiative lifetimes of excitons in quantum wires," *Phys. Rev. Lett.*, vol. 69, no. 23, p. 3393, 1992.

[194] P. Corfdir, J. Levrat, A. Dussaigne, P. Lefebvre, H. Teisseyre, I. Grzegory, T. Suski, J.-D. Ganière, N. Grandjean, and B. Deveaud-Plédran, "Intrinsic dynamics of weakly and strongly confined excitons in nonpolar nitride-based heterostructures," *Phys. Rev. B*, vol. 83, no. 24, p. 245326, 2011.

[195] A. Das, J. Heo, M. Jankowski, W. Guo, L. Zhang, H. Deng, and P. Bhattacharya, "Room Temperature Ultralow Threshold GaN Nanowire Polariton Laser," *Phys. Rev. Lett.*, vol. 107, no. 6, p. 66405, 2011.

[196] J. Heo, S. Jahangir, B. Xiao, and P. Bhattacharya, "Room-Temperature Polariton Lasing from GaN Nanowire Array Clad by Dielectric Microcavity." *Nano Lett.*, vol. 13, no. 6, pp. 2376–80, 2013.

[197] N. Akopian, G. Patriarche, L. Liu, J.-C. Harmand, and V. Zwiller, "Crystal phase quantum dots." *Nano Lett.*, vol. 10, no. 4, pp. 1198–201, 2010.

[198] E. Rauhala, N. Barradas, S. Fazinic, M. Mayer, E. Szilágyi, and M. Thompson, "Status of ion beam data analysis and simulation software," *Nuclear Instruments and Methods in Physics Research Section B: Beam Interactions with Materials and Atoms*, vol. 244, no. 2, pp. 436 – 456, 2006.

[199] M. Mayer, "Ion beam analysis of rough thin films," *Nuclear Instruments and Methods in Physics Research Section B: Beam Interactions with Materials and Atoms*, vol. 194, no. 2, pp. 177–186, 2002.

List of Figures

List of Tables

Acknowledgements

Writing the last pages of this thesis provides a satisfying feeling of relief. The past few years of experimental research with the aim to obtain a Doctorate in Physics have been, as it is usually the case, perturbed by many obstacles, re-orientations and other unexpected events. The outcome, as it is about to be concluded, would not have been possible without the help of countless people supporting me academically and personally. The most important of whom, I want to express my deepest gratitude to at this point.

First and most important of all, I want to thank my direct supervisor Sergio Fernández-Garrido. I had the privilege to work with you in a wonderful atmosphere, where we could discuss experiments, results and new ideas on a daily basis. When I started, I knew almost nothing about MBE, but you taught me well and pretty soon I felt home and comfortable in this very special world. I thank you for your guidance, your motivation, your time and interest. I thank you for you substantial assistance with all my papers and proof reading of my thesis. I thank you for the scientific development that you have led me through and the friendship that I have found.

I want to thank my doctoral supervisor and the director of the Paul-Drude-Institut, Prof. Henning Riechert, for giving me the opportunity to work at the institute and prepare my doctoral thesis. I appreciated the regular interest and support and the adaptability when the original experiments did not succeed as planned.

I want to thank my department head, Lutz Geelhaar, for many interesting discussions and regular motivation recharges. I thank you for various improvements and ideas for my manuscripts, presentations, and my thesis. I very much appreciated the opportunity of being able to present my research results at national and international conferences. Also, I very much enjoyed the weekly scientific group updates in the NW meeting.

I want to thank Oliver Brandt for many critical and fruitful discussions, for numerous improvements for my manuscripts, presentations, and my thesis. I have very much profited from your expertise both in the fields of MBE growth and spectroscopy.

I am very grateful to Hans-Peter Schönherr, Carsten Stemmler, Claudia Herrmann and Michael Höricke for keeping the Mostly Broken Equipment up and running for as long as somehow possible and thereby enabling the results presented in this thesis.

I am thankful to Anne-Kathrin Blum for countless hours of obtaining scanning electron micrographs.

I thank Bernd Jenichen for lots of effort teaching and assisting with XRD measurements as well as a wonderful time together at the MBE conference in Flagstaff in September 2014.

I thank Pierre Corfdir and Christian Hauswald for examining my samples so thoroughly and thereby enabling many of the results presented here.

I thank Esperanza Luna, Javier Grandal, Doreen Steffen, and Achim Trampert for preparing, performing, and interpreting TEM measurements on my samples.

I thank Emanuel Schmidt and Carsten Ronning from the Friedrich-Schiller-Universität Jena for carrying out RBS measurements on the decomposed NWs.

I want to thank Abbes Tahraoui, Claudia Herrmann, Sander Rauwerdink, Walid Anders for assisting me with the hybrid organic-inorganic experiments that where not successful

enough to become part of this thesis. I want to thank my RISE student Margaret Stevens and the master student Daniel Kage for their efforts on this difficult topic.

I also thank all my other fellow students, Ph.D. students and postdocs for a great time and many scientific and non-scientific events: Caroline Chéze, Pierre Corfdir, Tobias Gotschke, Javier Grandal, Christian Hauswald, Thomas Hentschel, Jumpei Kamimura, Hanno Küpers, Jonas Lähnemann, Ryan Lewis, Friederich Limbach, Yori Manzke, Mattia Musolino, Natalie Preissler, Timo Schuhmann, Claudio Somaschini, Maggie Stevens, David van Treeck, Kai Ubben, Joseph Wofford, Martin Wölz and whoever I may have forgotten.

I thank Prof. Holger T. Grahn and Vladimir Kaganer, Manfred Ramsteiner and Uwe Jahn for interesting discussions and Andreas Hartung, Nadine Möller, Anja Holdack and Bernd Pakulat for their administrative assistance.

I thank the entire staff of the Paul-Drude-Institut for a truly pleasant working atmosphere.

I thank the DFG for funding my Ph.D. position.

Last, but far from least, I thank my family and friends for filling my life with other things than physics.

Lana and Jonna, you are who matter!